ANALYSIS AND VALIDATION OF INTEGRAL POOL SPREADING MODELS OF LNG SPILLS ON CONCRETE

A Thesis

by

NISA ZAKIA ZAHRA ULUMUDDIN

Submitted to the Office of Graduate and Professional Studies of
Texas A&M University
in partial fulfillment of the requirements for the degree of

MASTER OF SCIENCE

Chair of Committee,	Luc Vechot
Committee Members,	Marcelo Castier
	Mahmood Amani
Head of Department,	M. Nazmul Karim

December 2017

Major Subject: Chemical Engineering

ABSTRACT

When a loss of primary containment of liquefied natural gas (LNG) occurs on the ground, a pool, that simultaneously spreads and vaporizes, is formed posing cryogenic, asphyxiating, and flammable hazards to its surrounding. Determining the pool size and vapor generation upon release play key roles in the accuracy of dispersion and consequence models. This work focuses on expanding the available data to be used for LNG source term model validation through the evaluation of an existing model.

A field-scale experimental setup was designed to study the pool temperature, pool spreading and heat flux under the concrete, after a release. In this work, liquid nitrogen (LN_2) was used as a safer analogue to LNG as it is a non-toxic non-flammable cryogen. The experiments were carried out inside a 6×5×1.2 m pit. A vaporizing pool spreading model based on Gas Accumulation over a Spreading Pool (GASP) was then implemented and used to predict the vaporization and pool spreading rates of the spill. Finally, the model predictions were compared to the experimental data.

The results of this work gave insight to the validity of two existing source term models, the coupling of a pool spreading model with Fourier's one-dimensional conduction heat transfer model. While the first model assumes that heat flux is uniform across the pool, the second model takes into account higher heat transfer due to exposure time difference between the outer rings of the pool to the center of the pool during pool spreading. Both models assume that the pool boils until it completely vaporizes. Experimental results indicate that the pool does boil until it completely vaporizes, and that the temperature at the center of the substrate was cooler than its outer parts. It was found that the model which accounts for higher heat transfer in the pool outer rings tends to underestimate pool size. Both models, however, overestimate the pool size at the early stages of the spill. As both models incorporate a solution of Fourier's one-dimensional conduction

equation, a comparison was also done between the predicted and experimental temperature.

ACKNOWLEDGEMENTS

This work was supervised by a thesis committee consisting of the committee chair Dr. Luc Vechot, and committee members Dr. Marcelo Castier, and Dr. Mahmood Amani. All work for the thesis was completed with the guidance of Dr. Tomasz Olewski. The experimental section was made possible by the collaboration of Ras Laffan Emergency and Safety College (RLESC) by facilitating us with the location, staff, and equipment as needed. I would also like to thank all the members and staff of the Mary Kay O'Connor Process Safety Center Qatar branch during the experiment preparation for the project. I also thank Marcin Kozusznik for his technical assistance during the preparation of sensors and the data acquisition system.

CONTRIBUTORS AND FUNDING SOURCES

Contributors

This work was supervised by a thesis committee consisting of Dr. Luc Vechot (advisor) and Dr. Marcelo Castier of the Chemical Engineering department and Dr. Mahmood Amani of the Petroleum Department.

The graph shown in Figure 4 was provided by Syed Qurayshi respectively and it has been published in 2015.

All other work conducted for the thesis was completed by the student independently.

Funding Sources

This work was made possible in part by the financial support provided by Qatar National Research Fund (QNRF) under Grant Number NPRP_6-425-2-172.

NOMENCLATURE

e	Constant related to thermal properties of the ground in Equation 14
C	An empirical constant in Equation 20
$Evap$	Evaporated mass flux, kg m^{-2} s^{-1}
F	Friction force over the bottom area of the pool, m s^{-3}
g	Acceleration due to gravity (9.81 m^2 s^{-1})
h, h_{min}	Depth, Minimum depth, m
Hv	Latent heat of vaporization, J kg^{-1}
k	Thermal conductivity, W m-1K-1
m	Mass, kg
Q	Heat flux, W m^{-2}
r	Radius, m
R_{aavg}	Average roughness of the substrate, μm
R_{amed}	Meadian roughness of the substrate, μm
σ_{Ra}	Standard deviation of the substrate, μm
s	Shape factor
S	Spill rate, kg s^{-1}
T	Temperature, K
Vap	Vaporization rate, kg s^{-1}
U	Velocity m s^{-1}

α	Thermal diffusivity, m^2 s^{-1}
ε	Froude number for spreading pool
ρ_w, ρ	Density of water, density of pool, kg m^{-3}
γ, C	Empirical constants for Equation 2 and Equation 3

Subscripts

L	Liquid
V	Vapor
s	Ground
j	Horizontal coordinate
w	Wetted point

ABBREVIATIONS

DAQ: Data Acquisition System

GASP: Gas Accumulation for Spreading Pools

MKOPSC: Mary Kay O'Connor Process Safety Center

LNG: Liquefied Natural Gas

LN_2: Liquid Nitrogen

RLESC: Ras Laffan Emergency and Safety College

RLIC: Ras Laffan Industrial City

TP-5: Traning Prop-5

TABLE OF CONTENTS

Page

ABSTRACT ii

ACKNOWLEDGEMENTS iv

CONTRIBUTORS AND FUNDING SOURCES v

NOMENCLATURE vi

ABBREVIATIONS viii

TABLE OF CONTENTS ix

LIST OF FIGURES xii

LIST OF TABLES xvi

1 INTRODUCTION 1

2 LITERATURE REVIEW 3

2.1 Background 3
2.1.1 Release types 4
2.1.2 Pool vaporization due to conductive heat transfer 4
2.1.3 Pool spreading 6
2.2 Previous experiments on cryogenic pool spreading on concrete 8
2.2.1 R C Reid and Wang (1978) 10
2.2.2 Lang *et al*. (1980) 10
2.2.3 Moorhouse and Carpenter (1986) 11
2.2.4 Olewski *et al.* (2013) 12
2.2.5 Vaporization experiments of liquid nitrogen 13
2.2.6 Nguyen *et al*. (2015) 16
2.2.7 Summary of existing experimental data 17
2.3 Review of existing models 18
2.3.1 Early pool spreading models 18
2.3.2 Heat conduction from the ground 20

2.3.3 Gas Accumulation over a Spreading Pool (GASP) 22
2.3.4 LPOOL by Technical Inc. 26
2.3.5 SOURCE5 by Trinity 27
2.3.6 Liquid Spill Modeling System (LSMS) 29
2.3.7 Process Hazard Analysis Software Tool (PVAP) 30
2.3.8 SuperChemsTM by ioMosaic 32
2.3.9 Summary of the research gaps 33

3 RESEARCH OBJECTIVES 36

4 METHODOLOGY 37

4.1 Modeling: Implementation of a pool spreading and conduction model 37
4.2 Experiment: Field-scale liquid nitrogen spill experiment on concrete 39
4.2.1 TP-5 state-of-the-art facility 40
4.2.2 General setup 43
4.2.3 Experimental procedure 48
4.2.4 Instrument locations 50
4.2.5 Uncertainty Analysis 65
4.2.6 Discharge flowrate from the tanker 66
4.3 Validation of the pool spreading model 68
4.4 Experiment: Field-scale liquefied natural gas spill on concrete 69
4.4.1 Pool temperature 71
4.4.2 Methane gas dispersion 71
4.4.3 Fire radiation 73

5 SPREADING AND VAPORIZING MODEL 78

5.1 Governing equations 78
5.2 Numerical solution and algorithm of solution 79
5.3 Verification and validation of pool spreading and vaporization model 84
5.3.1 Verification of the conduction model 84
5.3.2 Verification of non-vaporizing pool spreading model 85
5.3.3 Validation of the vaporization model 87
5.3.4 Validation with liquefied natural gas spill on concrete 89
5.3.5 Validation of non-vaporizing pool spreading model 91
5.3.6 Validation of pool spreading model for vaporizing pool 93
5.3.7 Summary of verification and validation activities 98

6 EXPERIMENTAL RESULTS 99

6.1 Challenges faced prior to experiment 99
6.1.1 Commissioning of data acquisition panel 99
6.1.2 Physical protection of data acquisition from dust and rain 100
6.1.3 Setup of software 100
6.2 Transition from boiling to evaporation regime 101
6.3 Temperature inside the concrete 102

7 VALIDATION OF EXISTING MODELS 105

8 PROGRESS IN LNG SPILL EXPERIMENT 109

8.1 Sequence of events 109
8.2 Preliminary results 111
8.2.1 Day 1 111
8.2.2 Day 2 113
8.3 Physical integrity of the facility 117
8.4 Summary and lessons learned 118

9 SUMMARY 120

REFERENCES 124

APPENDIX A 128

LIST OF FIGURES

Page

Figure 1: Schematic of LNG following a spill 4

Figure 2: General representation of a boiling curve (Olewski et al., 2013b)..... 6

Figure 3: Heat flux to LN_2 on rough and smooth concrete (Unpublished: Sadia et al. 2015)... 15

Figure 4: LN_2 spill heat flux at lab and medium scale (Reprinted: Quraishy et al., 2015)..... 16

Figure 5: Satellite view of RLESC with location of TP-5 facility 42

Figure 6: TP-5 experimental burning pit 43

Figure 7. Schematic of LN_2 delivery path 44

Figure 8: Spill point and radial coordinate system 45

Figure 9: Photos of the main structures within the experiment 45

Figure 10: Wood structure inside the pit aligning thermocouples and cryogenic hose 46

Figure 11: Bird-eye view of TP-5..... 46

Figure 12: Radius thermocouple arrangement for Trial 1 51

Figure 13: Radius thermocouple arrangement for Trial 2 51

Figure 14: Wooden thermocouple grid..... 52

Figure 15: Schematic diagram of sensors embedded within the base of the concrete 57

Figure 16: Schematic diagram of sensors embedded within the walls of the concrete pit 58

Figure 17: Schematic diagram embedded sensors in the upper base 59

Figure 18: Schematic diagram of embedded sensors in the lower base 60

Figure 19: Schematic diagram of embedded sensors in the lower walls 61

Figure 20: Schematic diagram of embedded sensors in the upper walls 62

Figure 21: Location of oxygen gas sensors in Trial 1 63

Figure 22: Location of oxygen gas sensors in Trial 2 63

Figure 23: Weather station at TP-5 65

Figure 24: Flowrate of spill throughout Trial 1 67

Figure 25: Flowrate of spill throughout Trial 2 67

Figure 26: Radius thermocouple arrangement for LNG spill 70

Figure 27: Wooden thermocouple grid and hose position 70

Figure 28: Bird-eye view of methane gas detector locations during LNG spill (Day 1) 72

Figure 29: Bird-eye view of methane gas detector locations during LNG spill (Day 2) 73

Figure 30: Bird-eye view of radiometer locations during LNG spill (Day 1 and 2) 76

Figure 31: Schematic diagram of water line network 77

Figure 32: Cooling water supply to radiometer 77

Figure 33: Flow diagram of the model 82

Figure 34: Verification of the Simple 1D conduction model 84

Figure 35: Similarity to $r \sim t^2$ behaviour for a non-vaporizing instantaneous release 86

Figure 36: Similarity to $r \sim t^{1/7}$ behaviour for a non-vaporizing and instantaneous release 86

Figure 37: Similarity to $r \sim t^{3/4}$ behaviour for a non-vaporizing and continuous release 87

Figure 38: Models prediction of the boil-off rate of LN_2 (Sadia et al., 2015) 89

Figure 39: Simple 1D and Webber1D against LN_2 boiling on concrete(Lang et al., 1980) 91

Figure 40: Comparison of Model 1 simulation with spreading of water on plywood 93

Figure 41: Validation with Moorhouse and Carpenter (Model 1 to 3) 94

Figure 42: Validation of Model 1, 2, and 3 against pool spreading data (Case 1 and 2) 97

Figure 43: Validation of Model 2 and 3 against pool spreading data (Case 3 and 4) 97

Figure 44: Validation of Model 2 and 3 against pool spreading data (Case 5 and 6) 98

Figure 45: Evidence of boiling during the experiment 101

Figure 46: Grid number allocation on pit base 102

Figure 47: Temperature across the nodes at 0.05 m concrete depth (Trial 1) 104

Figure 48: Temperature across the nodes at 0.15 m concrete depth (Trial 1) 104

Figure 49: Radius of pool as in all 8 measured directions (Trial 2) 105

Figure 50: 1D model simulation (dotted) against temperature 5 cm through the concrete 107

Figure 51: 1D model simulation (dotted) against temperature 15 cm through the concrete ... 107

Figure 52: LNG dispersion limited by water curtains 110

Figure 53: Pool fire generated at the large pit 111

Figure 54: Temperature of the pool on the pit ground at various locations (Day 1) 112

Figure 55: Ice formation after Day 1 post water drainage..... 112

Figure 56: Concentration of methane at various locations (Day 1)..... 113

Figure 57: Pool temperature at various depths above the surface (Day 2)..... 114

Figure 58: Concentration of methane at various locations (Day 2)..... 115

Figure 59: Radiative flux measured in various radiometers (Day 2)..... 116

Figure 60: After-experiment investigation evidence of insulation..... 116

Figure 61: After-experiment investigation evidence of concrete 117

Figure 62: Thermal conductivity of the concrete samples as a function of temperature..... 131

Figure 63: Heat capacity of the concrete samples as a function of temperature 132

LIST OF TABLES

Page

Table 1: Stages of pool spreading 8

Table 2: Summary of available cryogenic experimental data in literature 9

Table 3: Comparison of properties of different gases (various sources) 40

Table 4: Release condition of LN_2 48

Table 5: Weather conditions 49

Table 6: Spill detail 49

Table 7: Location of all radius thermocouples 53

Table 8: Level meter thermocouple positions at Trial 1 55

Table 9: Level meter thermocouple positions at Trial 2 56

Table 10: Weather station sensors 64

Table 11: Summary of discharge flowrate of LN_2 in both trials 68

Table 12: Thermocouple inside the pit during Day 2 71

Table 13: Outline specification 72

Table 14: Distance of methane gas detectors from the pit 73

Table 15: Specification of radiometers 74

Table 16: Radiometer working ranges 75

Table 17: Summary of model 79

Table 18: Input parameters to the model 81

Table 19: Temperature dependent parameters 83

Table 20: Flow diagram parameters 83

Table 21: Input data for lab-scale experiment by Sadia *et al*. 88

Table 22: Input data for LNG vaporization on concrete from Lang *et al*. (1980) 90

Table 23: Simulation input data for Belore and McBean (1980) 92

Table 24: Input data to the calculation for continuous release of LNG 94

Table 25: Input data of simulation to Nguyen *et al*. (2015) data 96

Table 26. Density measurements of concrete samples 129

Table 27: Composition of concrete 129

Table 28: Surface roughness measurement for TP-5 concrete 130

1 INTRODUCTION

Global demands for cleaner abundant energy are one of the drivers of the natural gas industry. The total Liquefied Natural Gas (LNG) trade is still a growing number, reaching 258 MT in 2016, which was a 13.1 MT increase from the previous year. Qatar remains as the largest LNG exporter, with an export of 77.2 MT, approximately a third of the global LNG supply (International Gas Union, 2017). Natural gas is liquefied by cooling, which leads to a 600 fold volume reduction and makes possible its transportation in liquid form using LNG ships. The number of importing countries has increased due to its economic feasibility. LNG is becoming increasingly obtainable even for countries with short-term demand for natural gas. Accounted in an International Gas Union, (2017) (IGU) report, "*Emerging markets will play an increasing role in development of new regasification capacity*".

LNG has specific characteristics that create challenges for the safety of LNG production, transport, and storage. It poses flammable, cryogenic, and asphyxiation hazards to its surrounding. In the particular scenario of a spill of LNG on ground, a liquid pool forms, simultaneously spreading and vaporizing at a rate proportional to the heat received from the surroundings. The generated vapor forms a dense cloud that moves downwind and may ignite if the cloud is within its flammability limit of 4.4 to 17 vol./vol % given that enough ignition energy is provided.

There are several stages to a risk analysis. First, the system has to go through a hazard identification stage, in which all hazards and potential harmful scenarios are recognized. Scenarios then go through a consequence analysis stage. For a release or loss of containment of LNG, consequence analyses are mostly interested in fire and explosion. Combined with a predicted frequency rate, risk can be calculated and then analyzed. Modeling the concentration of LNG vapor in the atmosphere requires the interaction of two models, a *dispersion* model, which predicts the concentration of the LNG vapor in the

atmosphere (governed by the atmospheric conditions), and a *source-term* model, which predicts the rate at which LNG vapor is formed (cloud formation - determined by the release conditions). While vapor cloud dispersion models have been successfully validated against numerous experimental data, vapor cloud formation in source-term models have received much less attention despite its importance(D. M. Webber *et al*., 2010). A misprediction of the LNG vapor formation and pool size may cause the wrong zones to be isolated and make the risk analysis ineffective. Thus, more research is required to ensure the reliability of existing source-term models.

This project aims to bring insight to the validity of common conduction and pool spreading models when LNG is spilled on the ground with new data. In the first part of this work, LN_2 was used as a safer analogue to LNG as it is a non-flammable cryogen. The scope of this work includes the validation work of a well-recognized vaporizing pool spreading model with experimental data generated in this work. At the end of this thesis, the project had the opportunity to conduct the experiment with LNG. This thesis will show partial results of the LNG experiment.

2 LITERATURE REVIEW

This section discusses the assumptions and validation of existing pool spreading models for cryogenic releases.

2.1 Background

Following an unpressurized release of LNG from the source, vaporization may occur at the source in the form of flashing. LNG has a boiling point of -162 °C. Upon contact with the ground, it immediately boils. Its vaporization rate is driven by the amount of heat the pool receives from the surroundings. In the case of pressurized leak, the discharge may be gaseous, liquid, or two-phase, and the scenario is complicated by flashing and rainout occurring at the release source. The pool then generates a flammable vapor plume. The plume initially sinks to the ground, and becomes increasingly buoyant as it mixes with air. In this work, the validation work is narrowed to an unpressurized release. We will only focus on the heat received through conduction from the ground.

Listed by Woodward and Pitblado (2010), the possible scenarios involving LNG spills on land may occur due to pump and pipe leaks (leaks under pressure), a leak from storage tanks (atmospheric pressure), an LNG storage tank rollover, and the vaporization of liquid pools generating a flammable vapor plume.

Figure 1 displays the schematic of a spill of an unpressurized LNG upon the ground. The release type (continuous or instantaneous), pool spreading, and simultaneous pool vaporization are the determining parameters for the source term and are explained in more detail in this section.

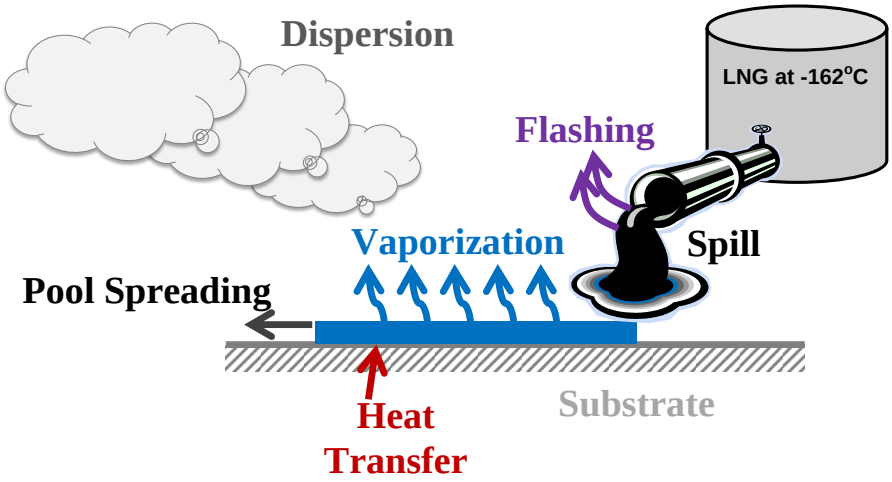

Figure 1: Schematic of LNG following a spill

2.1.1 Release types

Typically, the discharge can be categorized as either instantaneous or continuous. A spill is instantaneous when a large volume is spilled within a relatively short amount of time and it is considered continuous when the spill duration is long.

2.1.2 Pool vaporization due to conductive heat transfer

Experimental analysis by Burgess and Zabetakis, (1962) indicated that the conductive heat transfer from the ground is dominant at the initial period due to the high temperature difference. Hence, the more thermally conductive the substrate, the higher the vaporization rate. According to Olewski *et al*., (2013a), forced convection can also bring a significant effect on the vaporization. However, both convection and radiation effects will play a role in the rate of heat transfer in later stages, so conduction from the ground could be treated as the dominant source of heat transfer at the early pool life. It was experimentally determined that heat gain from convection and radiation will approximately account for approximately 30% of the overall heat transfer after first 10

minutes spill duration during a constant wind speed of 2-3 m s^{-1} for a non-spreading pool of 0.48 × 0.48 m^2 area (Olewski *et al.*, 2013a).

Thermal contact between the pool and the substrate determines the thermal power received by the pool from the ground. Thermal contact between the two is decreased when bubble formations block the heat path between the two media. Pool boiling can be achieved through different boiling regimes, which are driven by the temperature difference between cryogenic liquid and the ground (Figure 2). It occurs only after the onset boiling point *(ONB* in Figure 2). At very early stages of the spill, the temperature difference between the pool and the ground may lead to film boiling in which a film of vapor forms between the liquid and the ground limiting the heat transfer. For LNG spills on the ground, film boiling has only been observed on spills on smooth surfaces such as metals (R.C. Reid and Wang, 1978). As the ground cools down, the film breaks and more contact between the liquid and the ground is achieved, thus improving the heat transfer. This stage is known as transition boiling. The minimum heat flux between the film and transition boiling regime is referred to as the Leidenfrost point (*Min* in Figure 2). As the temperature of the ground keeps decreasing, the vapor film disappears, and boiling occurs through the formation of isolated bubbles forming at the ground surface nucleation sites. The maximum rate of heat transfer between nucleate and transition boiling regimes is called the critical heat flux (*CHF* in Figure 2).

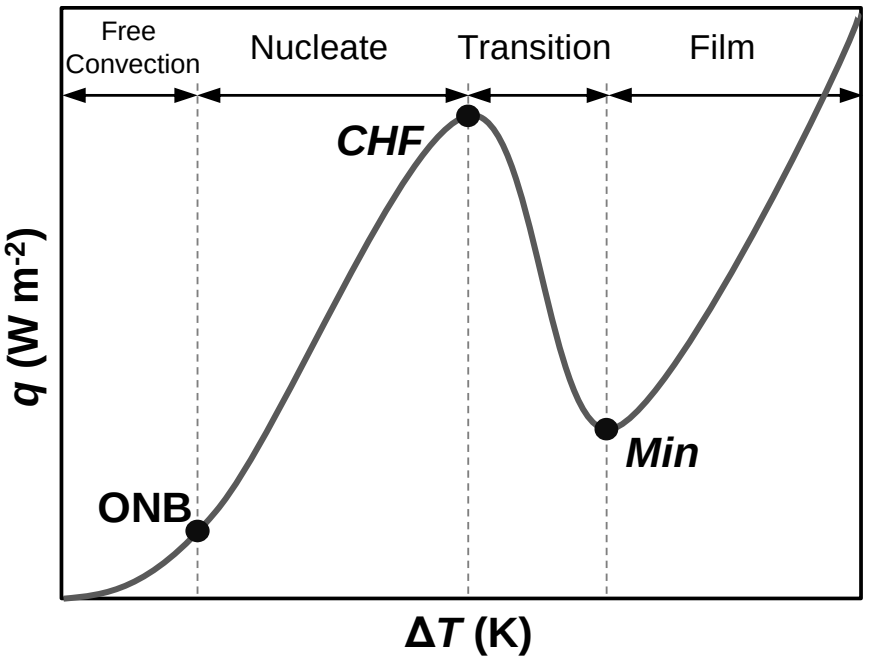

Figure 2: General representation of a boiling curve (Olewski *et al*., 2013b)

2.1.3 Pool spreading

When spilled on ground, LNG will form a liquid pool spreading on the surface. As the surface area of the pool is growing, the overall vaporization rate increases. The way the pool spreads depends on the forces acting on the liquid pool as described by the three following pool spreading regimes:

- Gravity-Inertia Regime

"Gravity-Inertia Regime" occurs when the main driving force of the pool spread is gravity and the resisting force to the spread is the liquid inertia. This regime is expected at early stage of the pool development, just after the release. The downward gravitational force acting on the pool causes an uneven pressure distribution within the pool, causing the pool to spread sideways. With time, the pool becomes thinner and thus the gravity force

decreases, and the pool spreading decelerates. The inertia of the moving liquid restrict the pool spreading. As the liquid covers a larger surface area, the effect of inertia minimizes and the next phase quickly occurs. The period of time in which the gravity-inertia regime occurs is momentary.

- Gravity-Viscous Regime

Gravity continues to drive the pool to spread. As the pool develops and immediately covers larger surface area, the effect of the liquid inertia diminishes and viscous friction generated between the pool and the ground becomes the dominant resistance to the pool spread. It is the longest regime that the LNG pool experiences.

- Surface Tension-Viscous Regime

For vary shallow pools, the effect of gravity becomes infinitesimal. The surface tension between the liquid-surface interfaces remains as the prevailing pool driving force. For a cryogenic spill on land, the surface tension-viscous regime may perhaps only be reached on smooth surfaces and have not been experimentally achieved. For a spill on normal rough surfaces, it is more likely for the pool to completely vaporize before the surface-tension force becomes dominant (D. M. Webber *et al.*, 2010).

In summary, pool spreading is governed by the acting dominant driving and resisting forces. The chronological order of the regimes is shown in Table 1. Lab-scale experiments indicate that the spreading of cryogenic liquids on surfaces such as concrete spend very little time in the gravity-inertial phase and are unlikely to reach the surface tension-viscous phase.

Table 1: Stages of pool spreading

	Early stage	**Middle stage**	**Last stage**
Driving force	Force of gravity	Force of gravity	Surface tension
Resisting force	Liquid inertia	Viscous forces	Viscous forces

2.2 Previous experiments on cryogenic pool spreading on concrete

Prince, (1985), Thyer, (2003) and Luketa-Hanlin, (2006) revealed that most experimental data provide LNG spills on water rather than on land. Additionally, most LNG spills on land were tested upon soil and sand substrates, and only three papers, by R C Reid and Wang, (1978), Lang *et al*., (1980), and Moorhouse and Carpenter, (1986a), experimented LNG spills on concrete, and only one is on pool spreading. The more recent source term experiments have been conducted using LN_2. The summary of existing experimental data for LNG and LN_2 spills on concrete is given in Table 2. So far, existing models have only been validated against the LNG data (Daish *et al*., 1998; Webber, 1991; Webber and Witlox, 2005). While they provide validation to a certain extent, each of them require the assumptions of one or two release conditions, which reduces the reliability of the simulation. Thus, there is a need to generate new data with the all release conditions specified to corroborate the validation of existing cryogenic liquid models.

Table 2: Summary of available cryogenic experimental data in literature

Reference	Chemical	Study	Spilled amount	Spill area	Substrate
Reid and Wang (1978)	LNG	Vaporization caused by conduction	N/A	103 cm^2 surface area	Concrete of 5 – 10 cm thickness
Lang *et al.* (1980)	LNG	Vaporization caused by conduction	N/A	22.9 cm diameter	Concrete of 2.5- 5 cm thickness
Moorhouse and Carpenter (1986)	LNG	Pool spreading	17 tonnes hr^{-1} for 300 s	Maximum of 16 m radius	Real case concrete with semi-infinitive depth
Olewski *et al.* (2013)	LN_2	Contribution of different heat transfer mechanisms on vaporization	N/A	0.5 × 0.5 m^2	Concrete
Sadia *et al.* (2015)	LN_2	Vaporization caused by conduction	1 kg	0.3 × 0.3 m^2	Concrete of 0.05 m thickness
Syed *et al.* (2015)	LN_2	Vaporization caused by conduction	80 L	0.5 × 0.5 m^2	Concrete
Kim *et al*. (2016)	LN_2	Pool spreading	3.4×10^{-2} 5.6×10^{-2} 9.0×10^{-2} kg s^{-1} for 100 s	0.8 m radius	Concrete of 0.025 m thickness

2.2.1 R C Reid and Wang (1978)

R C Reid and Wang (1978) examined LNG boiling rates on various substrates to make recommendations towards the selection of dike floor materials. The substrates were cut into rectangular slabs and put into Styrofoam boxes for insulation. The edges of each box were sealed with foamed polyurethane and its walls with Mylar film.

Weight was monitored to measure vaporization rate. Other than concrete, substrate materials such as soil, sand, and dry polyurethane were tested. The insulating concrete was varied by the aggregate types and density. However, no significant difference in boiling rates was observed between the concrete types and vaporization rate was found to be directly proportional to $t^{-1/2}$ until the test was terminated. Experimental data on concrete differ from sand and other substrates because it is impermeable and does not allow percolation of the liquid.

Reid and Wang's paper focuses on comparing LNG boiling rates on different substrates. However, there is no information about how much LNG was spilled, the composition of the spilled liquid, and whether the spill was instantaneous or continuous.

2.2.2 Lang *et al*. (1980)

Lang *et al*. (1980) performed rapid liquid spillages of LNG from a Dewar onto a horizontal slab of a substrate resting on a sensitive balance. The spillage was done in small quantities as the substrate size consists of thin discs of 22.9 cm diameter and 2.5 to 5 cm thick. The average composition of the LNG spilled was 90% methane, 8% ethane, and 1% propane by volume. The disc was put inside polystyrene tubes for an insulated containment. The substrates tested in this publication ranged from ordinary concrete, lightweight concrete, soil, steel, and particulate material. Some concrete and soil substrates were wetted, and the activity involved the combination of soaking the test samples in water for weeks and controlled drying. A glass dewar was supported by a wooden cradle mounted on the

polystyrene walls to discharge LNG. The glass dewar was left open at the bottom and a thin plastic membrane was used to replace the lid. The spills were triggered by the tear of the membrane.

The spill was instantaneous, lasting for approximately 1 second. Each substrate was tested at various water content. Boil-off rates were measured by a balance. They were found higher at high density materials and higher water contents as they are more conductive of heat.

In their experiments, the boil-off rates of LNG on concrete during nucleate boiling goes to a maximum of 0.4 to 0.5 kg m^{-2} s^{-1}. For LNG spills on various soils, the maximum rate could be higher to above 1 kg m^{-2} s^{-1} because of higher contact area. Additionally, film boiling was not observed with spills on concrete. In the highly moist samples, transition boiling regime can be observed at the beginning. However, only nucleate boiling was observed in the drier samples.

The paper was successful in studying the comparison of LNG vaporization rates on various concrete. However, it did not provide enough information about the release conditions. Although the paper provided the vaporization rate, the quantity spilled and the thermal properties of each substrate were not specified in this paper.

2.2.3 Moorhouse and Carpenter (1986)

Moorhouse and Carpenter (1986a) published the only relatively large scale of LNG spills on concrete, allowing for pool spreading observations. LNG was spilled at a rate of 17 tonnes min^{-1} into the apex of a 45^{o} sector. The setup of the release allowed the measurement of the liquid head using a simple float and a continuously purged manometer. The release rate into the substrate was made as consistent as possible by continuously feeding the tank with LNG, keeping the liquid head relatively constant. The

radius of the pool was monitored by an arrangement of thermocouples and infra-red camera. The mean pool radius was plotted with time. A total of four tests were conducted on soil and concrete. The applicability of Equation 1 was then tested against the LNG pool spreading data. The authors investigated the value of *hmin,* the minimum pool depth before the pool completely vaporizes. It was found that the value of 10 mm gives good agreement with the experiments. From this outcome, the experimental work by Moorhouse and Carpenter has shown that that reasonable prediction can be made using simple pool spreading models.

$$\frac{dr}{dt} = (2g(h - h_{min}))^{\frac{1}{2}}$$ *Equation 1*

Where *r* is radius, *h or* h_{min} is the pool depth and minimum pool depth respectively, *g* is acceleration due to gravity and *t* is time.

2.2.4 Olewski *et al.* (2013)

A measurement of the contribution of the different heat transfer mechanisms, conduction, convection, and radiation, to the vaporization rate of LN_2 was conducted experimentally by Olewski *et al.* (2013a), where LN_2 was an experimental substitute to LNG as a safer analogue.

The first set of experiments was conducted inside the lab, where the LN_2 was let to vaporize from a 7 L Dewar flask and its vaporization rate was measured by a balance. Convective and radiative heat contributions were individually controlled by generating convection from an electric fan and thermal radiation through a light bulb.

The second set of experiments was done inside a wind tunnel located at Fire Station 2 of the Ras Laffan Industrial City (RLIC), Qatar. This set of experiment was designed to

expand the range of the laboratory experiments and to allow for the same study on different substrates. LN_2 was spilled into self-made concrete or polystyrene square-based containers of dimensions 0.5 × 0.5 × 0.4 m and 0.48 × 0.48 × 0.1 m respectively. The concrete box was used to measure heat transfer by conduction without the effects of convection. Meanwhile, effects of convective and radiative heat transfer was studied following a spill into the polystyrene box, where the heat loss by conduction is limited by the polystyrene material.

Heat flux plates and thermocouples embedded inside the concrete at different depths of the base and walls and on the surface were used to measure heat transfer by conduction. To control effects of radiation and convection, the box was capped/uncapped and was located inside a wind tunnel. Conductive effects from the lid and walls were subtracted to the total heat flux to calculate conductive heat flux from the concrete sample.

The contribution of convective and radiative heat transfer was examined. It was found that the contribution of these heat transfer mechanisms for an LN_2 spill on concrete was as high as 30% after 10 minutes when the wind speed was 2-3 m s^{-1}. Thus, models which assume heat conduction from the substrate as the sole source of heat transfer may not be accurate at large times.

2.2.5 Vaporization experiments of liquid nitrogen

In recent years, researchers have spilled LN_2 onto a slab of concrete at lab and small-field scale. The experiments were conducted within the same context and under the same project as this thesis. In their work, vaporization was measured and then combined for the two sets of experiment.

2.2.5.1 Lab scale liquid nitrogen spill on smooth and rough concrete (Sadia *et al.*, 2015)

LN_2 was spilled into a box containing a concrete slab of dimensions 0.3 × 0.3 × 0.05 m. The walls of the box were made out of 1 mm thick stainless steel walls of height 0.15 m above the surface. The substrate comprises of two slabs of concrete, allowing the placement of thermocouples 5 cm under the surface. Twelve thermocouples and three heat flux sensors were installed to monitor the concrete temperature and heat transfer under the concrete. The container was placed on top of a balance. Vaporization rate was obtained through the changes in mass throughout the spill. Six runs were conducted in this project, spilling approximately 1 kg of LN_2 each instantaneously. The paper also makes the distinction between the boiling regimes of LN_2 spills on smooth and rough concrete surfaces.

The author first observed that LN_2 did not reach the evaporative regime throughout the experiment. Hence, the assumption that all heat received by the pool is used to vaporize the pool is valid. Secondly, the obtained heat flux profiles indicated that LN_2 goes through film and transition boiling regimes when spilled on smooth concrete. In contrast, the film boiling regime was not observed for spills on rough concrete. For an LN_2 spill on smooth concrete, an average of 52.99 kW m^{-2} was measured as the critical heat flux with the maximum vaporization rate of 23.96 g s^{-1}. For the spill on rough concrete, the critical heat flux value was higher at an average of 69.27 kW m^{-2} with a vaporization rate of 31.33 g s^{-1}. The profile of the vaporization rate of LN_2 on smooth concrete was provided as shown in Figure 3.

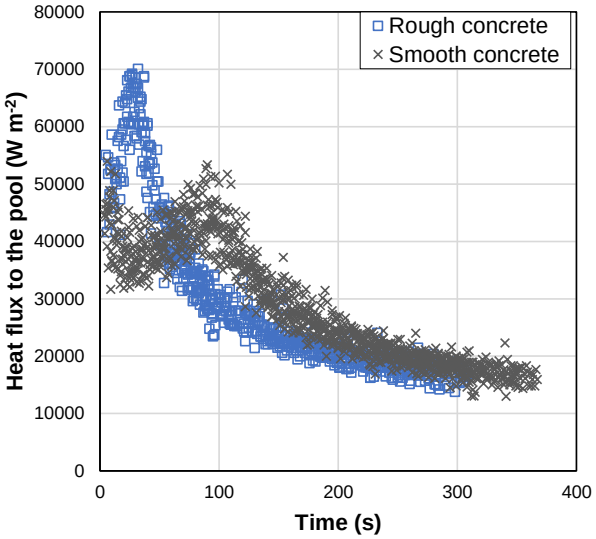

Figure 3: Heat flux to LN_2 on rough and smooth concrete (Unpublished: Sadia et al. *2015)*

2.2.5.2 Medium scale liquid nitrogen spill on concrete (Quraishy *et al.*, 2015)

To obtain vaporization data for later times, a medium-field scale 180 L LN_2 spill was conducted inside a wind tunnel on another sample of the same concrete slab located at Fire Station 2 of RLIC. A 32 L container was prepared with a concrete pad embedded with 11 thermocouples and 2 heat flux sensors to measure temperature and heat flux through the concrete at four layers. It rests on top of a balance of maximum weight of 300 kg. Vaporization was obtained through the 30 s average mass changes of the container. LN_2 was spilled slowly for 5 minutes. The container was covered with a polystyrene lid to minimize convective and radiative heat transfer to the pool. Conductive heat transfer from the lid was also later subtracted from the total heat flux to give conductive heat transfer from the concrete slab only. The vaporization rate and heat flux generated from this experiment was found to have continued the results from the lab-scale experiments as the duration for vaporization was longer as shown in Figure 4.

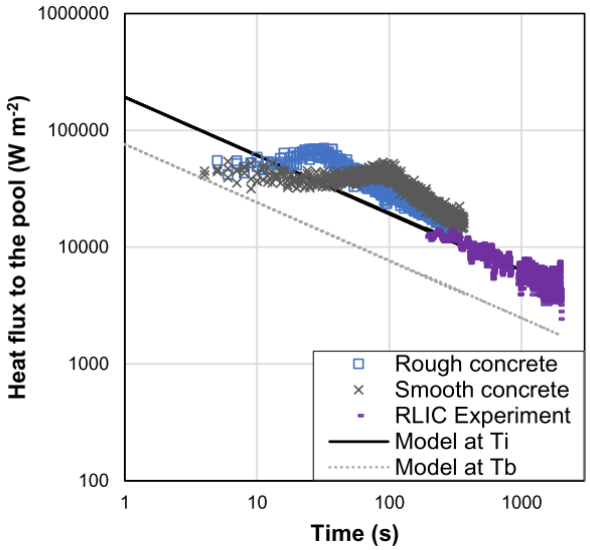

Lab scale : Rough and Smooth concrete
Medium scale : RLIC Experiment

Figure 4: LN_2 spill heat flux at lab and medium scale (Reprinted: Quraishy et al., *2015)*

The thermal properties of the concrete in these two sets of experiments are similar as they were extracted from the same location (referred to TP-5 in this thesis, refer to 4.2.1).

2.2.6 Nguyen *et al.* (2015)

Cryogenic pool spreading was investigated by Nguyen *et al.* (2015) by spilling LN_2 through a funnel onto a concrete plate. The substrate has a radius 0.8 m and thickness 0.025 m. Thermocouples have been aligned in four directions, of 0.05 m apart, starting from the center of the plate. The liquid is detected wherever the thermocouples indicate the boiling temperature at -190°C. The container of the plate was rested on a balance with a resolution of 0.1 g. A total of six trials were conducted. Nozzles of dimensions of 6 mm, 8 mm, and 10 mm were used to maintain the spill flowrates at 3.4×10^{-2} kg s^{-1}, 5.6×10^{-2} kg s^{-1} and 9.0×10^{-2} kg s^{-1} respectively. A total of 7.5 L of LN_2 was spilled in each trial.

*Reprinted with permission from "Modelling of Transition and Nucleate Boiling of Liquid Nitrogen Spill on Concrete" by S. Quraishy, A. Sadia, T. Olewski and L. Véchot, 2015. Hazards 25 Conference. Copyright 2015 by Syed Qurayshi

Data for the average pool radius was provided in this paper but no model has been validated against it. This paper provides validation data for pool radii for only up to 0.3 m, which is miniscule compared to larger spills. Some features in the experimental setup are questionable for the use of model validation. Firstly, the substrates thermal properties were missing in this data. Additionally, the work did not investigate if the substrate thickness of 0.025 cm is enough to correctly imitate a real case concrete (approximately semi-infinite depth). The authors also claimed that the input flowrate of the LN_2 was varied by changing the nozzle diameter. However, with liquid flows through a funnel, the liquid flowrate is more dependent on the head measurement rather than the hole size. The paper does not indicate if the liquid head was maintained, which in turn does not prove that the flowrate was constant in each trial.

2.2.7 Summary of existing experimental data

There is a lack of experimental data available for cryogenic spills on concrete. Data provided by Reid and Wang (1978), Lang *et al.* (1980), Sadia *et al.* (2015), and Syed *et al.* (2015) consist of vaporization data at lab-scale, where vaporization is measured for a non-spreading pool. Such data provides an incomplete result, as the pool is not in contact with new ground and the total heat flux into the pool starts to decrease as the ground cools down. In a real case or an accident, LNG is typically spilled over a large or unbounded area. The surface will be so big that the pool is in contact with new warmer ground most, if not all of the time. Data of a vaporizing spreading pool will thus give better insight to the accuracy of LNG source term model predictions.

Experiments which take into account pool spreading have been generated by Moorhouse and Carpenter (1986) and Nguyen *et al.* (2015). However, some aspects of the latter paper are still questionable and require to be addressed to the main author. To improve literature data and validation of existing source term models, additional experimental data observing cryogenic pool spreading and vaporization together are needed.

2.3 Review of existing models

A vaporizing pool spreading model on land or water mostly involve the same types of equations D. M. Webber *et al.* (2010). They all consist of a continuity, momentum, and heat balances. The TNO yellow book (Opschoor, 1979) has summarized the aspects in which models would actually differ. Most models are based on the same limited amount of literature tackling the issues of vaporization and pool spreading. This section reviews assumptions of existing models of use by various institutes and companies. Convective and radiative heat transfer models are not in the scope of this review.

2.3.1 Early pool spreading models

Early pool spreading models on solid substrates are derived from the shallow water equations. The shallow water equations are derivations of Euler's equations for inviscid flow when the pool is shallow and the vertical accelerations are negligible. They describe the pool behavior in terms of velocity and pool depth and can be written as Equation 2 and Equation 3.

$$\frac{\partial h}{\partial t} + \nabla(\vec{u}h) = 0 \qquad \textit{Equation 2}$$

$$\frac{\partial (hu_i)}{\partial t} + \vec{\nabla}(\vec{u}h_i) = -\frac{\mathrm{g}}{2}\nabla_i h^2 \qquad \textit{Equation 3}$$

Where $_i$ denotes the coordinate (*x*,*y*, *or z*) and *h* is depth in meters, $\vec{u}$ is velocity in m s^{-1}, *g* is the gravity constant in kg m^{-2} s^{-1} , and *t* is time in seconds.

A potential weakness of the classic shallow water equations is that it assumes that the spreading occurs on a level surface. Another weakness of the shallow water equation when applied on spills on solid substrates is the assumption that there are no resistance terms while the pool is extremely shallow. The inviscid assumption of the shallow water theory is not valid for shallow pools because friction increases as the pool covers an increasingly large area. This theory was only successfully applied for oil slicks spreading on water as the dominant resistance to the pool spread comes from the displacement of water being pushed out to the pool front. For spills on water, this condition was incorporated by specifying the boundary conditions at the pool front.

Webber listed the models of Raj and Kalelkar (1974), Opschoor (1978) and Briscoe and Shaw (1980) as the early models of cryogenic source term models. Equation 4 displays the cryogenic pool spreading equation on water derived from the classic shallow water equation.

$$\frac{d^2r}{dt^2} = -\gamma\frac{h}{R} \qquad \textit{Equation 4}$$

$$\gamma = \varepsilon g\left(\frac{\rho_w - \rho}{\rho_w}\right) \qquad \textit{Equation 5}$$

Where ε is the Froude's number for spreading pool, ρ_w, ρ are density of water and density of pool respectively, and γ, C are empirical constants.

In all of the three models, the old model for the pool spreading on land comprises of the same equation but with the relative density factor replaced with density *(D. M. Webber et al.*, 2010). Froude's number was derived from spill experiments on water, where it is assumed that hydrostatic pressure difference is balanced between the pool front and the

water pushing against the pool (Webber, 2012). These old models are no longer recommended for assessing the dispersion of a cryogenic spill. Most existing pool spreading models, which are discussed in Sections 2.3.3 to 2.3.8, are now improved integral models of the shallow water equation, taking into account friction.

2.3.2 Heat conduction from the ground

At the initial stages of the pool, the dominant mode of heat transfer for cryogenic spills is conduction from the solid surface (Burgess and Zabetakis, 1962). Many models assume one-dimensional heat conduction from the ground with perfect thermal contact.

The contribution of conduction towards the total vaporization rate depends on time and area of contact. For a pool contained in a bund, the heat received by the pool decreases with time as the ground cools down. For spreading pools, the outer rings of the pool is in contact with warmer ground, resulting to higher heat transfer into the pool, until it completely vaporizes or until it has reached the boundaries of a bund.

Most vaporizing pool spreading models accessible in literature, to be seen in Sections 2.3.2 to 2.3.8, have assumed that conduction to the pool can be modeled by the analytical solution of Fourier's one-dimensional (1D) heat conduction equation. The equation for Fourier's 1D heat conduction is shown in Equation 6.

$$\frac{\partial T}{\partial t} = \alpha \frac{\partial^2 T}{\partial z^2} \qquad \textit{Equation 6}$$

where α is the thermal diffusivity of the ground and T is temperature.

The simplest solution of Fourier's 1D equation is solved when the pool is assumed to be boiling throughout its life and that the ground is at ambient temperature outside of the pool. These assumptions are specified at the boundary conditions shown in Equation 7.

Equation 7

$$\begin{array}{lll} T(z,0) = T_i & at & z \in \langle 0, \infty \rangle \quad for \quad t = 0 \\ \left.\begin{array}{ll} T(0,t) = T_s & at \quad z = 0 \\ T(z \to \infty, t) = T_i & at \quad z \to \infty \end{array}\right\} & & for \quad t > 0 \end{array}$$

Where *Ts* is the ground temperature and *Ti* is the pool boiling point. The result is Equation 8. The resulting heat flux equation is indicated in Equation 9.

Equation 8

$$T = T_i - (T_i - T_s) \cdot erfc\left(\frac{z}{2\sqrt{\alpha \cdot t}}\right)$$

Equation 9

$$\bar{q} = -k\frac{\partial T}{\partial z} = \frac{k}{(\pi\alpha)^{0.5}}(T_i - T_s)t^{-0.5}\exp\left(-\frac{z^2}{4\alpha t}\right)$$

Where T is temperature, z is depth under the concrete, α is thermal diffusivity, and k is thermal conductivity.

The depth is 0 at the point of contact between the pool and the ground. This results to the "simple 1D" solution of conduction heat transfer towards the pool shown in Equation 10.

$$\bar{q} = -k \left. \frac{\partial T}{\partial z} \right|_{z=0} = \frac{k}{(\pi\alpha)^{0.5}} (T_i - T_s) \cdot t^{-0.5}$$ *Equation 10*

Where *k* is the ground thermal conductivity. At the surface, the equation indicates that heat flux is proportional to $t^{-0.5}$.

The "simple 1D" conduction equation have been solved with the basis of:

1. Perfect thermal contact between the pool and the ground
2. Uniform heat flux across the pool per unit time as if it was at the center of the pool
3. The heat flux tends to infinity when time is close to 0
4. Temperature of the concrete is assumed ambient at infinite depth of the substrate

In reality, the pool experiences a maximum heat flux value. Thermal contact between the pool and the ground is also imperfect and changes according to the boiling regime. It is to be noted that some models to be discussed in this section assume a different set of boundary conditions to account for contact with warmer ground as the pool spreads.

2.3.3 Gas Accumulation over a Spreading Pool (GASP)

Gas Accumulation over a Spreading Pool (GASP) was first developed in the 1980s for the Health Safety and Environment (HSE) by the Safety and Reliability Directorate (SRD) of the United Kingdom Atomic Energy Authority (UKAEA)(D. M. Webber *et al*., 2010). Its initial purpose was to correct theoretical misses incorporated in "SPILL," the previous model used by HSE. Its authors, D. M. Webber *et al*. (2010), has also analyzed the scientific basis of the shortcomings of early pool spreading models in the 1980s as discussed previously.

Equation 11 and Equation 12 display the set of pool spreading equations for instantaneous and continuous spills on land.

$$\frac{dr}{dt} = U$$ *Equation 11*

$$\frac{dU}{dt} = \frac{4g(1-s)h}{r} - F$$ *Equation 12*

Where *r* is radius, *F* is the effect of friction over the bottom area of the pool and *U* is velocity.

The acceleration of the pool spread is described in Equation 12, where it is the result of the resisting and driving forces. The friction term consists of the summation of the turbulent and laminar terms shown in Equation 13. They depend on the velocity which in turn is dependent on the radius of the pool. The dimensionless constants C_{Lam} and C_{Turb} are provided by Webber (1991).

$$F_{Lam} = C_{Lam}\frac{vU}{h^2} \qquad F_{Turb} = C_{Turb}\frac{U^2}{h}$$ *Equation 13*

Where *v* is kinetic viscosity and *C* is an empirical constant. The depth *h* is calculated as the volume of pool divided by its area. For continuous spills, a mass balance shown in Equation 14 is necessary.

$$\frac{dV}{dt} = S - Vap$$ *Equation 14*

Where *S* is the spill rate and *Vap* is the vaporization term. As explained by D. M. Webber *et al.* (2010) one shortcoming of using this form of equation is that it does not imply that the spill source is localized at one point. To model spills into a bund, the maximum radius of the pool is restricted by the bund dimensions and its spreading rate becomes 0.

GASP's conduction heat transfer model assumes the pool is in perfect thermal contact with a semi-infinite ground initially at ambient temperature. The liquid is set to boiling temperature as soon as they are in contact.

In a paper by Webber (1987), the vertical conduction estimation was found to be sufficient especially for large pools, as horizontal heat transfer was found to be only significant at the edge of the pool. As the pool thins out, the effects of such dimension becomes less and less important.

The Green's function of Fourier's conduction equation shown in Equation 15 was used to solve for the area-averaged vertical conduction heat transfer to the pool. Temperature difference is taken at each time step to take into account contact of the pool with fresh new ground.

$$Q_l(t) = -\frac{k\phi(t)}{\sqrt{\pi\alpha t}} - \frac{k}{A(t)\sqrt{4\pi a}}\int_0^t dt'(t-t')^{-\frac{3}{2}}[\phi(t)A(t) - \phi(t')A(t')]$$ *Equation 15*

$$\phi(t) = T(t) - T_a$$ *Equation 16*

$$A(t) = \pi r^2(t)$$ *Equation 17*

Equation 15 is Webber's solution to the one-dimensional heat conduction equation with the additional following surface boundary conditions: (D. M. Webber *et al.*, 2010)

- The temperature of the pool is time dependent
- Temperature difference is calculated at each time step

The second term in Equation 15 indicates that variation in heat transfer across the pool is taken into account, allowing for the fact that the outer rings of the pool are in contact with new warm ground. When the pool reaches its maximum radius, the second term in Equation 15 cancels out as the area becomes constant. However, there are no separate equations for heat transfer during different boiling regimes, and thermal contact is assumed perfect, which is not in the real case due to bubble formation during boiling.

The GASP model has been validated with Reid and Wang's LNG spills on insulating concrete and Webber and Jones' butane experiments on insulating floor to validate the vaporization model(D. M. Webber *et al.*, 2010). To validate for the simultaneous spreading and vaporization, GASP was plotted against the LNG radius profile generated by Moorhouse and Carpenter and found good agreement(D. M. Webber *et al.*, 2010).

2.3.4 LPOOL by Technical Inc.

LPOOL is a pool spread and vaporization model within the LECKON system, a system which merges selected source term and dispersion models for accidental chemical releases. Teuscher, Sabnis, and Drivas were noted as the initial authors for LPOOL's preliminary model, HAZARD (Woodward, 1990).

The model can tackle a broad range of release conditions such as spills from horizontal or vertical cylinders, confined or unconfined releases, two-phase discharges, and insulated and uninsulated vessels.

The pool spreading model in Equation 18 numerically solves for 2-dimensional shallow layer equations for radial flow over a flat ground (Woodward, 1990; Opschoor, 1979).The set of equations are solved using Crowley second-order finite difference solution.

$$\frac{\partial h}{\partial t} + \frac{1}{r}\frac{\partial RhU}{\partial r} = m_L^{\cdot} - \dot{m}_V \qquad \textit{Equation 18}$$

Where $\dot{m}_L$and $\dot{m}_V$ are the liquid and vapor mass rates respectively.

LPOOL solves heat conduction from the ground by Fourier's ideal one-dimensional heat conduction model where it assumes the same boundary conditions as the "simple 1D" model (Woodward, 1990).

$$Q = \frac{k(T_s - T_L)}{(\pi\alpha(t - t_w))^{1/2}} \qquad \textit{Equation 19}$$

$$where\ t - t_{wj} \geq 2\ s$$

Note: *twj* is the time when the grid ring j is first wetted by the spreading pool. T_s is the ground temperature and T_L is the liquid temperature.

The pool spreading model was verified against Belore and McBean's small-scale experimental data of water spilled on plywood and spills of crude oil on frozen arctic ground, snow, and ice (Woodward, 1990). LPOOL's vaporization rate model was verified by comparing against experimental data published by Kawamura and Mackay, (1987), where vaporization rates of volatile materials, Freon 11 and n-pentane, and less-volatile materials, cyclohexane and n-hexane, were measured when on sand.

When it comes to verifying the combined pool spread and evaporation model, the model performance was compared with simulations of the Briscoe and Shaw model (Woodward, 1990). In the pool radius profile generated, LPOOL predicted a longer lasting pool with a higher radius. Comparisons against the Briscoe and Shaw model has been discouraged by D. M. Webber *et al.* (2010) as it has been superseded by GASP.

2.3.5 SOURCE5 by Trinity

The source term model in SOURCE5 has been analyzed descriptively in one of HSE's review paper done by D. M. Webber *et al.* (2010). For instantaneous spills on land, pool spreading is modeled by Equation 20.

$$\frac{dr}{dt} = \sqrt{Cg(h - h_{min})} \qquad \textit{Equation 20}$$

Webber (2012) has criticized radius profiles in the form of Equation 20. Firstly, such equations are an adaptation of a pool spreading model of liquid on water. As reviewed by Webber (2012), this approach has no scientific justification for the resisting forces acting on the pool on solid ground would differ. Although the equation indicates that the velocity

decreases with time, there is no mention of viscous friction resisting the pool to spread (D. M. Webber *et al.*, 2010). Flaws were also found in the consistency of equations in its technical manual, making the applicability of the model unclear (D. M. Webber *et al.*, 2010).

The logic of SOURCE5's continuous spill model, not shown in this paper, was also unjustified. The model assumes that the pool vaporization rate is equal to the discharge rate until the pool reaches the bund walls, after which, only then is the vaporization rate controlled by the conduction heat transfer from the bund (D. M. Webber *et al*., 2010). It is then unclear how the pool can reach the end of the bund if the pool vaporizes instantaneously during its spread (D. M. Webber *et al*., 2010). The conduction heat transfer to pools on land was modeled as the "simple 1D" equation as previously derived.

Finally, the mass vaporization rate is modeled by Equation 21. It indicates that the mass rate is linear to the pool area, implying that the mass shrinks radially at constant depth, which is unclear how that would be the case in reality (D. M. Webber *et al*., 2010).

$$\frac{dm}{dt} = \frac{e^*}{\sqrt{t}} R^2$$ *Equation 21*

Where e is a constant related to thermal properties of the ground.

According to D. M. Webber *et al.* (2010) in an HSE report, no clear or documented validation activities has been done to the SOURCE5 models.

2.3.6 Liquid Spill Modeling System (LSMS)

Liquid Spill Modeling System (LSMS) is a model designed for cryogenic and volatile pool spreading and vaporization, also able to take into account multi-componence of the spilled material. It is capable of simulating instantaneous and time-varying continuous spills, and also model planar and axisymmetric source geometries. A multi-component mixture can be modeled by indicating the thermodynamic variables of each component and common mixtures such as LNG, LPG, liquid oxygen and butane have already been predefined. Variations in liquid temperature and composition during vaporization are taken into account in the model.

LSMS numerically solves the 2-dimensional shallow-water equation using the finite-volume method to give pool depth, area, velocity, temperature, composition and vaporization rate per unit time following a spill. The shallow water approximations were adopted because the spill horizontal dimensions largely outdistance the vertical dimensions. Consequently, the horizontal velocity is much more dominant than the vertical motions. Properties of the vertical profile of the pool also tend to homogenize with convection and boiling. By assuming axisymmetric or planar geometry, variations in the horizontal dimensions was also excluded. All of these observations validate the simplification of three-dimensional continuity and momentum equations to depth-averaged equations, resulting to the approximation of shallow water equations.

Following a spill, the cryogenic liquid spreads and gets heated up from its surrounding. Vaporization is calculated using the multicomponent generalization of the Brighton (1985)'s single-component model. When the pool temperature increases up to its boiling point, then bubbles begin to form and induce a local increase in depth within the flow. This aspect was highlighted by Daish *et al.* (1998) as an effect that is important when predicting dike overtopping.

The model was plotted against experimental data of Moorhouse and Carpenter (1986) where LNG was spilled on concrete. Two theoretical curves, one of a pure methane spill and one as an LNG mixture spill, were generated to compare the single-component model and multi-component model to a cryogenic spill on concrete. The pure methane spill model showed better agreement to the data but the possible reasons as to why that is, is not discussed in the paper (Linden *et al.*, 1998). Brighton (1985) claimed that the data were too limited to draw anymore conclusions.

LSMS has also been validated with small-scale liquid methane spill on sand, evaporation of butane from a containment dike, spreading and vaporization of liquid hydrogen on water, and spreading and dike overtopping of water from a planar channel (Linden *et al.*., 1998).

2.3.7 Process Hazard Analysis Software Tool (PVAP)

PVAP is the pool model in Process Hazard Analysis Software Tool (PHAST). It uses Briscoe and Shaw (1980)'s equation to model heat conduction from ground, assuming the ground to be a uniform semi-infinite medium (Oke and Witlox, 2006). Just like the previous models, Briscoe and Shaw (1980) solves Fourier's heat conduction equation assuming the liquid pool is thin, at uniform boiling temperature, in perfect thermal contact with the ground, and that heat conduction in the ground is vertically one-dimensional. The mass vaporizing rate can be found by dividing the heat flux by latent heat, which gives Equation 22.

$$\overline{\dot{m}_1} = \frac{\overline{\dot{Q}_1}}{L} = \frac{K(T_s - T_L)}{L(\pi\alpha t)^{1/2}} \qquad \textit{Equation 22}$$

Where L is the latent heat.

Equation 23 is the mass rate equation allowing for different contact times for a spreading pool, with t' being the arrival time for pool radius *r'* (Briscoe and Shaw, 1980). A correction factor χ was added to compensate for surface roughness.

$$\frac{dm}{dt} = \frac{Q}{L} = \frac{\chi K(T_s - T_L)}{L(\pi\alpha)^{1/2}} \int_0^{R(t)} \frac{2\pi r' dr'}{(t - t')^{1/2}} \qquad \textit{Equation 23}$$

The model for pool spreading on land is shown in Equation 24.

$$\frac{dr}{dt} = \sqrt{2g(h - h_{min})} \qquad \textit{Equation 24}$$

In Equation 24, *hmin* is the minimum depth at which spreading must be terminated. The authors of PVAP's technical manual (Webber and Witlox, 2005) argued that the form of the equation is wrong, but it does give an agreeable qualitative behavior. The form of this pool spreading equation was also seen in SOURCE5 (Section 2.3.5) and it has been previously criticized by Webber (2012) on "*A model for spreading pools*". The choice of *hmin* will be highly dependent on the ability of the substrate to maintain the pool and the liquid viscosity, which is not captured in the model (Oke and Witlox, 2006). Only experimental data can provide good estimation of this value.

Validation of PVAP was done in three main stages. First, its spreading logic was validated against non-volatile materials while its evaporation model was validated against spills in confined areas (Witlox and OKE, 2008). Belore *et al.* (1986) have published data of continuous spills of water on flat plywood. The model was used to simulate their experiments using the minimum depth of 0.005 m and 0.01 m. Both assumptions were found to fit the experimental data relatively well (Oke and Witlox, 2006).

The second stage consists of simulating the model against R C Reid and Wang (1978)'s boiling rates of LNG when instantaneously spilled in confined areas of typical dike floor materials (Oke and Witlox, 2006). The experiment was set up to minimize heat transfer from convection and sources other than the ground and ensured that the pool was always in the boiling regime. The model prediction agrees with the experimental data very well. According to the PVAP theory manual (Oke and Witlox, 2006), however, the model has not been validated against larger scales of simultaneously spreading and vaporizing liquid spills.

An area of improvement for the pool spreading equation is the formulation of the minimum depth (h_{min}) as it is function of the liquid physical properties such as surface tension, viscosity and density. The formulation of capillary depth (h_c) was published by Webber, however it was speculated that this value would be too low and result in the overestimation of radius and the underestimation of spill durations (Oke and Witlox, 2006). Currently, h_{min} is derived from small-scale experimental data, which has yet to be validated against larger data scales.

2.3.8 SuperChemsTM by ioMosaic

The pool spreading model incorporated in SuperChemsTM consists of mass and momentum conservation equations written by Webber solved numerically based on the shallow water equation. For a symmetrical spreading of the pool, simplified and integral solutions of the shallow water equations are used to calculate the bulk properties of the pool

The pool spreading and vaporization equations are solved numerically each time step, allowing for fresh warm ground to be covered by the concentrically growing pool (ioMosaic Corporation and Whitepaper, 2007). Like the vaporization models in GASP and PVAP, SuperChems^{TM} takes into account higher temperature difference at the outer rings.

IoMosaic Whitepaper (2007) has also claimed that film boiling and the transition regimes from film to nucleate boiling have been taken into account, however, access to its technical reference manual has been restricted to its users only.

For the validation for the cryogenic on-land spill models, SuperChems™ has been validated against small-scale data by Drake and Reid (1975)'s LNG Experiments and two data sets from MIT LNG Research Center (R C Reid and Wang, 1978).

The paper by Drake and Reid (1975) focuses on how boiling rates of LNG changes with soil type, soil moisture content, and LNG composition. Liquid nitrogen, liquid methane, and a mixture consisting of 93% methane and 7% ethane were their tested specimens. A cylindrical well of diameter 0.18 m and 0.22 m height was fit into a 0.31 m Styrofoam cube for insulation. Inside, soil is packed at the bottom to a depth between 0.05 to 0.06 m. Mass was monitored in order to observe boiling rates and its results were simulated on SuperChems™.

Similarly, data from an LNG and liquid methane spill on typical dike floors in a paper by MIT LNG Research Center (R C Reid and Wang, 1978) was used for validation. The model simulation was validated against the data sets for spills on low compact soil and sand. A mixture of 99% methane and 1% ethane was spilled at ranges 0.663 and 0.875 kg to a spill area of 0.1 m^2 on low compact soil and sand respectively. IoMosaic Whitepaper (2007) reported that there seemed to be inconsistency within the experimental data as the vaporized mass was reported to be greater than the reported spill mass. Nevertheless, no simulation against spill on concrete was displayed in this report.

2.3.9 Summary of the research gaps

Early pool spreading models based on the classic shallow water equations have now been disproved for spills on land because of the absence of friction and vaporization terms (D.

M. Webber *et al.*, 2010). They are only applicable to spills on liquid substrates as resistance from the water front can be set at the pool boundaries. Literature review has shown that many commercial pool spreading models are now improved equations based on the shallow-water equations, though they vary in the degree of complexity. So far, there has not been much criticism towards the use of such equations.

In all the models reviewed, none has taken into account resistance due to liquid inertia and pool spreading due to the liquid surface tension. Although the gravity-inertia regime has been described in theory books, it may be momentary in nature, as the effects of friction quickly overtakes inertia. Similarly, liquid surface tension is not taken into account in pool spreading models because it is within a regime that is rarely reached for cryogenic pools(D. M. Webber *et al.*, 2010).

Modeling LNG spills on the ground requires coupling the pool spreading model with heat transfer models. Most conductive heat transfer models have been based on Fourier's one-dimensional heat conduction equation, and they contain assumptions which may not reflect reality as LNG is boiling. The first most common simplification is the boundary conditions of the conduction heat transfer; the ground surface is set to the liquid boiling temperature when in contact with the liquid, and is set to ambient temperature outside of the pool. In reality, the temperature of the ground not in direct contact with the liquid may still be cooler than the ambient temperature. Most vaporization models also assume perfect thermal contact between the ground and the liquid, which is not realistically true because of the bubbles formed during boiling. Whether these models are sufficient for the modeling of LNG releases depend on the outcome of its validation checks to be done in this paper.

As accounted by various papers, there is a lack of published data towards the validation of the pool spreading and vaporization of LNG. Most source-term experimentations on LNG have been done in small scale, mainly focusing on its vaporization rate for non-

spreading pools. Hence, validation of the pool spreading and conductive heat transfer assumptions should be improved by validating existing models against data of larger scales.

The GASP model by Webber and Brighton (1987) was chosen as a suitable representative vaporizing pool spreading model for other existing models. Firstly, the shallow water equation and one-dimensional conductive heat transfer are both integrated within the model. It was also found to also be the most comprehensive model of high publicity in literature. Other commercial models such as PVAP have even been compared to GASP, making it a credible benchmark. Lastly, GASP has been validated against the most up-to-date experimental data. Therefore, the validation of GASP should correlate with the validation of other models.

3 RESEARCH OBJECTIVES

The aim of this thesis is to validate existing source term models of LNG spills on concrete ground with a new set of experimental data at medium scale. To achieve this objective, this work was divided into modeling work and experimental work. The first part was to implement an existing cryogenic pool spreading model, based on GASP, which entails a pool spreading component and a vaporization component. The models calculate mainly the pool radius and vaporization rate. Then, two medium field-scale spills of LN_2 were conducted inside a concrete pit, measuring pool radius and temperature change within the concrete. Results of the model simulation of the experiment were then compared with the experimental data. Extension of the experimental work to spilling the LNG itself was attempted when LNG was made available at the last stage of the project. Two LNG spill experiments were aimed to measure the pool radius and vaporization rates, as well as the dispersion of LNG vapor and fire radiation during a pool fire. The preliminary analysis of the setup and measurements are included in this thesis.

4 METHODOLOGY

This research was divided into two main parts:

- Modeling part: An existing integral vaporizing pool spreading model was implemented using Matlab. Prior to its use, the code was verified and validated with existing literature data.
- Experimental part: Two LN_2 spills inside a large concrete pit was conducted, recording pool radius and concrete temperature and other release conditions sufficient for model validation. When LNG became available, LNG was spilled twice using a preliminary experimental setup. The first spill was set to measure pool vaporization, spreading, and vapor dispersion, while the second spill was ignited to allow the recording of fire radiation. Recommendations regarding the experimental setup was made and the preliminary analysis of the results was obtained.

The following describes each part of the work in greater details.

4.1 Modeling: Implementation of a pool spreading and conduction model

Following the literature review, it was decided to choose a widely accepted source term model in literature in order to simulate pool spreading and conduction. The following criteria for the choice of the model were used:

- The model has a widespread publication record;
- The model has been reviewed by credible institutions;
- The model has been validated against the most up-to-date experimental data

Gas Accumulation and Spreading Pools (GASP) is the only model in which its algorithm and derivations have been published in-depth (D. M. Webber *et al.*, 2010; Webber, 1991). It has been used by a number of organizations including Health and Safety Environment (HSE), Health and Safety Laboratory (HSL), UK Atomic Energy Authority (UKAEA), AEA Technology, ESR Technology, BP, TNO and many others, proving its usability (D. M. Webber *et al.*, 2010). As discussed in Section 2.3.3, its vaporizing pool spreading model has been validated against the only LNG pool spreading data published by Moorhouse and Carpenter (1986a), making it a suitable pool spreading model for cryogenic spills. Even other models such as PVAP have been verified against GASP in order to ensure their soundness.

The model solves simultaneously ordinary differential equations of mass, radius, and velocity, and an integral equation of conductive heat transfer. There were two solutions to conduction available in literature which were both tested in this work. In total, three models were generated and analyzed; the first model simulates the pool spreading of a non-vaporizing pool and the second and third simulates a spreading vaporizing pool with different boundary conditions for the conduction heat transfer.

Other modes of heat transfer were neglected as conductive heat transfer is the dominant mode of heat transfer at the beginning of a cryogenic pool life when spilled onto a solid substrate. The model was implemented and solved utilizing Matlab version R2016b. The Matlab algorithm and solution were also verified by implementing the same equations into Polymath. It was then validated with existing experimental data available on literature. A limiting factor of GASP tolerated in this study is that it does not consider phase change before the liquid reaches the ground.

4.2 Experiment: Field-scale liquid nitrogen spill experiment on concrete

The objective of this part is to conduct a medium-field scale experiment to validate the generated model. As LNG was not readily available at the time this thesis started, liquid nitrogen (LN_2) was used as a safer analogue as it is a non-flammable cryogen. The similar characteristics of LN_2 when spilled onto the ground, being a vaporizing spreading pool, makes the generated experimental data valuable to validation of LNG source term models. Conducting large spills of LN_2 also allows for the learning curve of experimenting with LNG in the future.

Other characteristics of LN_2 also differ from that of LNG. Some properties of nitrogen, methane, and ethane have been listed in Table 3 to allow for comparison. LNG typically comprises of 85-95% methane and a few percent of ethane (Woodward and Pitblado, 2010). Hence, the properties of LNG will fall between the values of ethane and methane. The latent heat of nitrogen is comparatively lower, and is 2.5 times lower than that of methane. Thus, it is expected that vaporization occurs faster with LN_2 than with LNG. Secondly the nitrogen gas density at the boiling point is 4 times higher than LNG, and its vapor cloud would stay close to the ground for a longer time. Thermal conductivity is higher in methane, which indicates that the heat flux received by the pool should be relatively higher than nitrogen. These observations imply that the vaporization and pool spreading rates from LN_2 cannot be directly extrapolated to LNG.

Regardless, LN_2 is a suitable alternative to LNG because its pool spreading and vaporization rates depend on the same parameters, such as the thermal properties of the substrate. It is also much more obtainable than LNG as it is in the standard market. The non-flammable properties of LN_2 highly minimizes the operational risk during the experiment in case any source of ignition exists within its path. It also allows a bigger range of equipment and sensors because they do not need to be explosion proof, thus

reducing the cost and time for the experiment. There are plans to conduct experiments with LNG covered in Section 10 of this thesis.

Table 3: Comparison of properties of different gases (various sources)

	Methane	**Ethane**	**Nitrogen**
Molecular weight, g mol^{-1}	16	30	28
Boiling point (1.013 bar), ^{o} C	-161.60	-89.01	-195.90
Liquid density, kg m^{-3} (1.013 bar)	421	546	808
Gas density, kg m^{-3} (1.013 bar at boiling point)	1.82	1.26	4.61
Solubility in water, g gas/ kg of water (1.013 bar and 0°C)	0.04	0.13	0.03
Latent heat of vaporization, kJ kg^{-1} (1.013 bar at boiling point)	510	488	198
Heat cap. at const. pressure, Cp (1 bar and 25°C), J mol^{-1} K^{-1}	35	53	29
Thermal conductivity, mW m^{-1} K^{-1} (1.013 bar and 0 °C)	32.81	21.30	24.01
Dynamic viscosity , $\times 10^{-4}$ Pa s^{-1} (1.013 bar at boiling point)	1.18	1.66	1.27

4.2.1 TP-5 state-of-the-art facility

The experiment was conducted at a state-of-the-art facility available at LNG training prop-5 (TP-5) of Ras Laffan Emergency and Safety College (RLESC). The Mary Kay O'Connor Process Safety Center (MKOPSC) has worked closely with Qatar Petroleum (QP) on the design of the TP-5 in order to facilitate studies for LNG source term, dispersion, and pool fire experiments. RLESC is owned by Qatar Petroleum (QP),

designed for the main purpose of fire training. It contains 29 different training props (TPs) to train firefighters in various situations. It spans over an area of 1 km^2. Satellite view of RLESC and location of the TP-5 is shown in Figure 5.

TP-5 consists of three concrete burning pits. The pit used for the experiment is of size 5 x 6 m and depth 1.2 m (Figure 6).The bottom of the pit is 1% slopped towards a small sump in south-west corner. There are 100 thermocouples and 13 heat flux plates embedded in the concrete of this pit to measure temperatures and heat transfer within the concrete substrate (Figure 15).

The site prevalent wind direction is from the North-West. The experiments can be observed from a control room located 80 m east from the experimental pit (Figure 11). On the west side of the pit are fences and an unoccupied area.

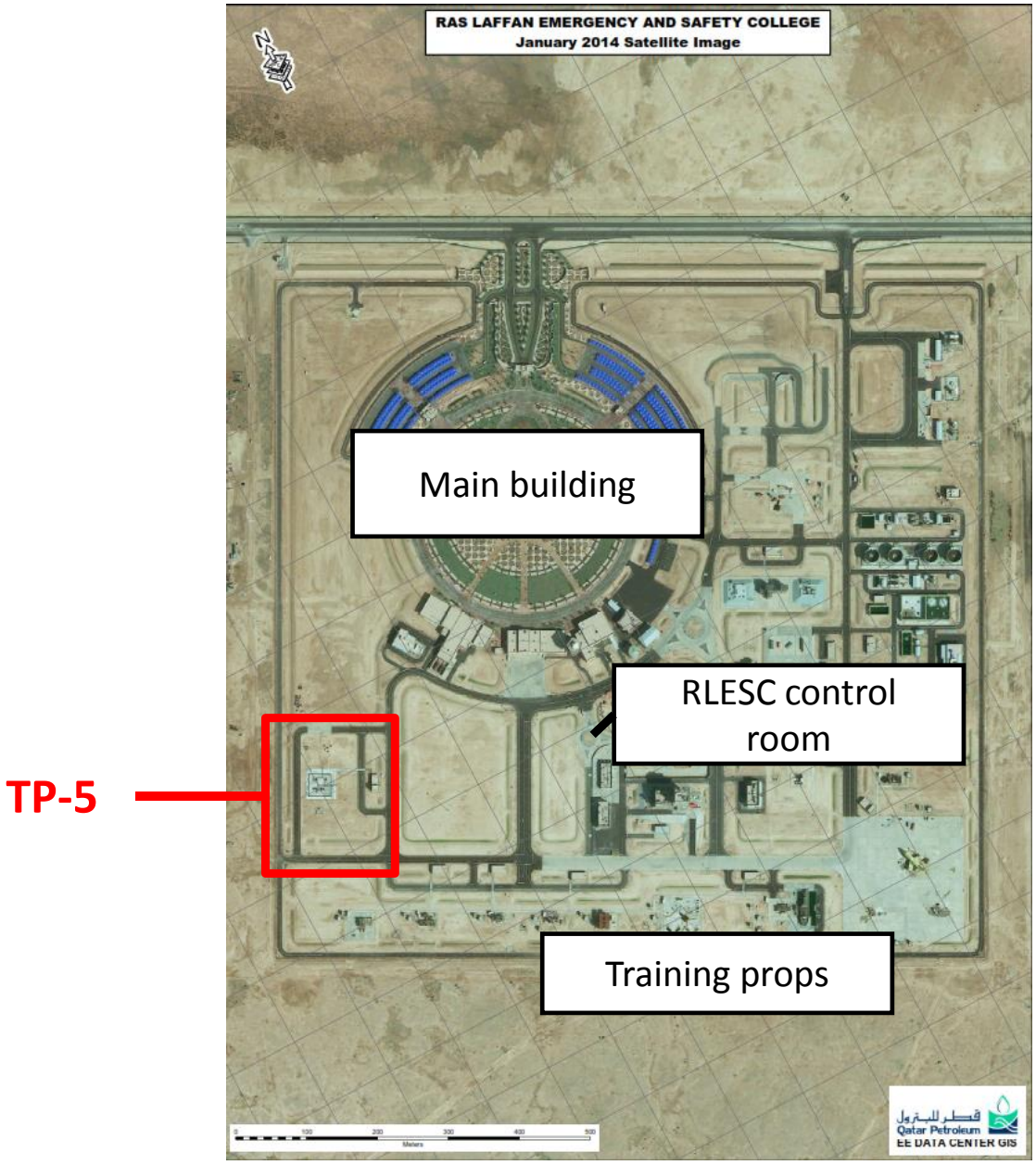

Figure 5: Satellite view of RLESC with location of TP-5 facility

Figure 6: TP-5 experimental burning pit

The TP-5 research facility includes two marshaling panels, which can accommodate more than 600 different sensors, which are terminated and connected to laptop in TP-5 control room. Marshalling panels are located at the east and north of the pit. Sensor readings are processed by programmable logic controllers and then communicated to a laptop at the classroom through Ethernet switches. In total, approximately 600 connections are available for use at the panels, comprising of N and K thermocouples, mV, Ethernet, RS-232, RS-485 and 4-20 mA connections. The sensors utilized during this project include fireproof thermocouples, heat flux plates, oxygen gas detectors, and a bubbler meter (Section 0). The site is also equipped with a stationary weather station, which is described in the next section.

4.2.2 General setup

A total of 10,000 L of LN_2 contained in a road tanker was delivered through a cryogenic hose into a concrete pit of size 5 × 6 × 1.2 m (Figure 7). There are six main components to the experimental setup: the concrete substrate, a pathway for the cryogenic hose, a thermocouple frame, thermocouples, heat flux plates, oxygen gas detectors. A set of wooden planks was set across the top of the pit to become the pathway for the delivery

hose. Using cable ties, the hose was tightened to the planks and then set to spill in approximately the middle of the pit (Figure 8 and Figure 9). The pit sides are labeled as north, west, east, and south, and an 8-direction radial coordinate system (N, S, E, W, NE, SE, SW, SE) was used to locate the thermocouples measuring radius (Figure 8). The north of the pit is 20 ^{o} east to the geographical true north. It is also noted that the pit has a 1% slope towards the sump. Thermal properties of the substrate has been analyzed and its results are given in Appendix A.

An insulating material such as wood was chosen as the frame material to minimize any temperature reading disturbances to the thermocouples. Additionally, the wooden frame is supported by several 13 cm bolts of 3 mm diameter in order to minimize physical obstruction to the pool spread caused by the framework.

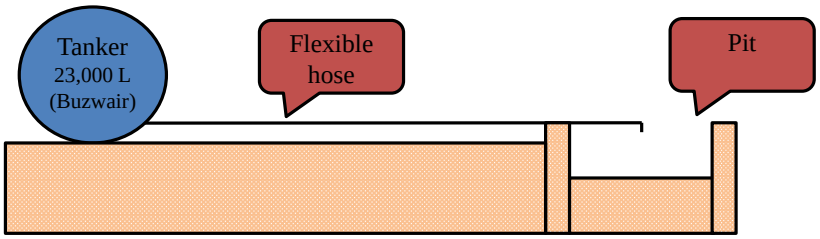

Figure 7. Schematic of LN_2 delivery path

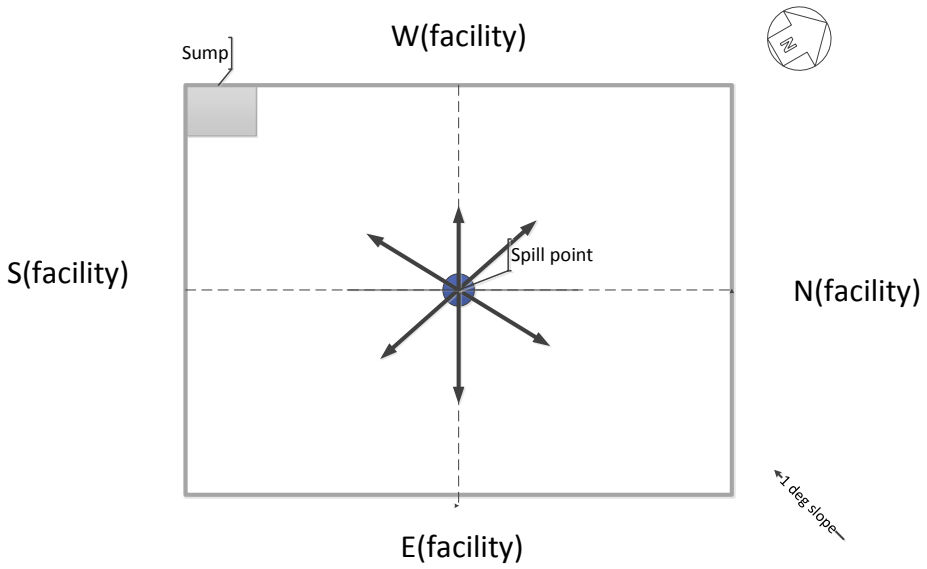

Figure 8: Spill point and radial coordinate system

Top and side view of experimental setup:

[1] LN_2 road tanker
[2] Wind fences
[3] Oxygen gas detector
[4] Thermocouple grid
[5] Delivery cryogenic hose
[6] Delivery pit

Figure 9: Photos of the main structures within the experiment

Figure 10: Wood structure inside the pit aligning thermocouples and cryogenic hose

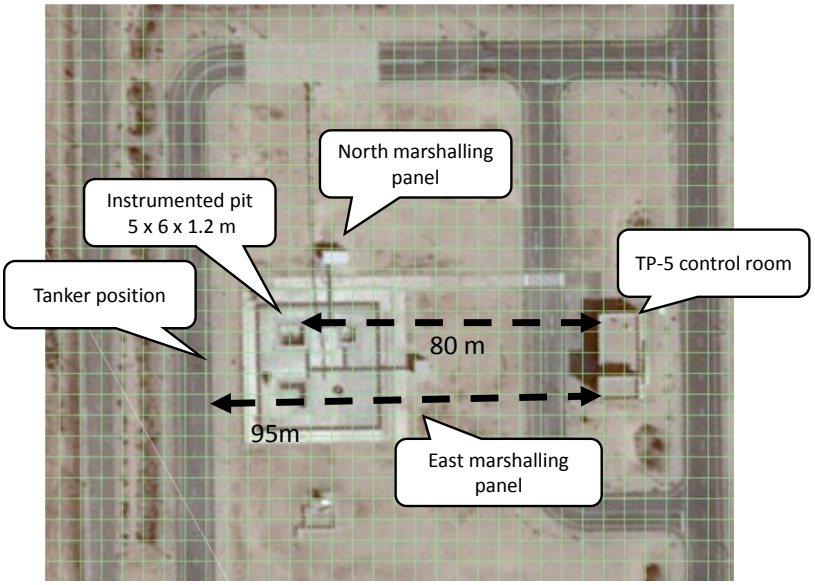

Figure 11: Bird-eye view of TP-5

The pool radius and pool level were detected using thermocouples. To detect the pool front during the experiment, 23 thermocouples (during Trial 1) and 27 thermocouples (during Trial 2) were mounted along radially arranged horizontal planks. The pool radius can be detected in 8 directions: north, south, east, west, north-east, north-west, south-east and south-west. Holes were drilled into the wood and the thermocouples were tight-fitted through the hole. Metallic cable holders held the wiring in place. Along each line, the thermocouples were approximately spaced 1 m apart, starting from the inner frame. Liquid is detected wherever the thermocouples display values close to the boiling point of LN_2 (-196°C). The schematic diagram and positions of each thermocouples are a part of Section 4.2.4.1. The pool level was detected using a similar way to the pool front method. A total of 13 thermocouples were vertically aligned on a vertical wooden plank. The measurable pool depths are detailed in Section 4.2.4.2.

A total of 100 thermocouples and 13 heat flux plates have been embedded under the concrete to measure the heat transfer and temperature inside the substrate. The base was divided into the upper base (0.05 m through the ground) and the lower base (0.15 m through the ground). Similarly, the walls are divided into the upper walls and lower walls. The lower walls are approximately at a 0.05 m height while the upper wall is the segment at a 0.5 m height.

At the base, the pit was divided into 9 nodes. Thermocouples and heat flux plates were planted 0.05 m and 0.15 m under the ground at each node. In total, there were 18 nodes within the base. From a bird-eye view, the 4 pit walls were divided into a total of 12 nodes, with each side bearing 3 nodes along the edge. Within each node there sub-nodes, which comprises of the lower-wall and the upper-wall section, and the inner-wall and the outer-wall section. In total, there are 48 nodes at the walls. Thermocouples were planted at each node to increase the reliability of the readings. The details of the location of each sensor are given in Section 0.

Surrounding the pit are 4 wooden fences with the purpose of minimizing the effects of wind towards the pool. Oxygen gas detectors were also positioned around the pit and near the tanker to ensure the safety of personnel during the experiment. The schematic of the oxygen sensors are given in Section 4.2.4.4. Two trials of the experiment have been conducted and the experimental procedure is discussed in Section 4.2.3.

4.2.3 Experimental procedure

The experiment was conducted in two runs, where each run was conducted on separate days. The first trial was conducted on 15th December 2016 while the second was conducted on 31st January 2017. Both trials were conducted when the atmospheric stability was A – C so to gain reproducibility of the results. In both trials, the hose spilled LN_2 at a height of 15 cm above the ground to minimize rain-out to other parts of the pit. Table 4 to

Table 6 contain a summary of the release and atmospheric conditions measured during the experiment.

Table 4: Release condition of LN_2

Release data	**Trial 1**	**Trial 2**
Volume, m^3	10	10
Pressure of tanker, bar	2	4
Density of LN_2, kg m^{-3}	800	800
Release height, cm	15	15

Table 5: Weather conditions

Atmospheric condition	Day 1	Day 2
Wind speed @ 2 m, m s^{-1}	6.17 ± 1.25	1.23 ± 0.77
Air temperature @ 2m, ^{o} C	24.6 ± 0.5	22.87 ± 1.23
Solar radiation kW m^{-2}	0.72 ± 0.07	0.52 ± 0.06
Humidity, %	49.1 ± 1.3	50 ± 5.7
Atmospheric stability	C	A

The experiment consisted of a series of spills into the pit until the tanker is empty. In both experiments, the pool was maintained at depths below the maximum range of the level meter while managing not to dry out the pit. These details are summarized in Table 6.

Table 6: Spill detail

Trial	Spill	Duration, min	Volume spilled, m^3
Trial 1	First	66	7.6
	Second	25	2.6
Trial 2	First	20	1.9
	Second	12	1.8
	Third	21	3.2
	Fourth	23	3.7

4.2.4 Instrument locations

The location of some thermocouple and oxygen gas detectors were modified between Trial 2 and Trial 1. For oxygen gas detectors, the locations had to be modified due to the wind speed and direction changes. Trial 1 has also provided a learning curve for the preparation of Trial 2, as it was found that there were not enough data points for the measurement of the pool radius. An additional level meter was also placed inside the pit for Trial 2 to obtain reproducibility of the measured pool level. This section discusses the exact locations of each sensor during each trial of the experiment.

4.2.4.1 Pool radius

The radius of the pool is detected by thermocouples arranged in 8 directions. The walls of the pit are labeled as north, east, west, and south. In each direction, 2 – 4 thermocouples were installed as shown in Figure 12 and Figure 13. The only addition to the setup during trial 2 are the 4 thermocouples positioned in the diagonal directions, as there were not enough in Trial 1. In total, 23 thermocouples were used in Trial 1 and 27 thermocouples were used in Trial 2. The contact point between the thermocouple tip and the surface was marked and measured from the north-west corner of the pit. On the day of the experiment, the spill point was also measured from the same reference point. The detectable pool radii of the spill was then calculated, at an accuracy of ± 2 mm and shown in Table 7.

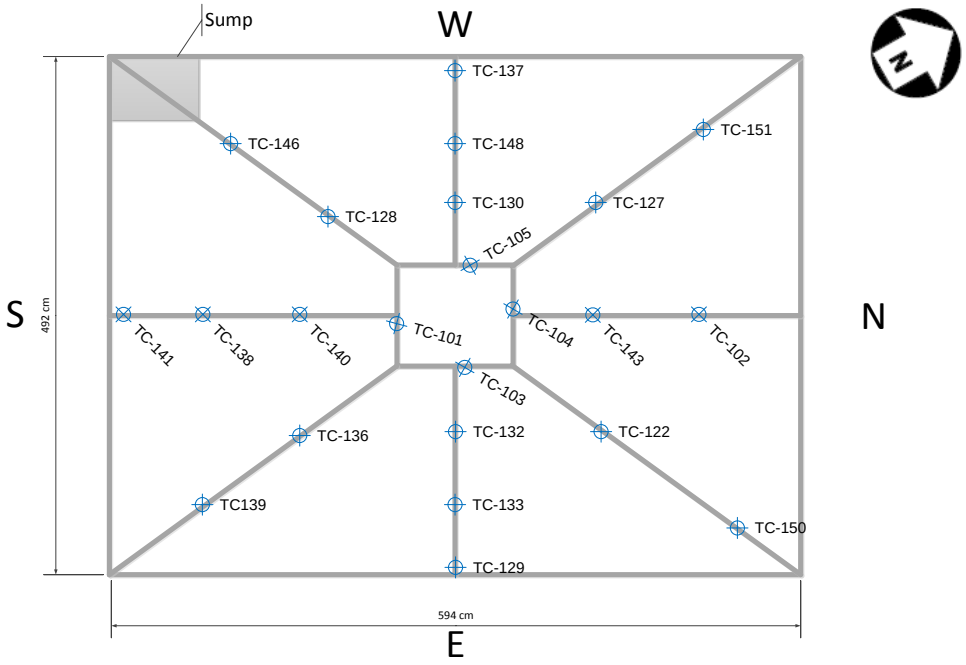

Figure 12: Radius thermocouple arrangement for Trial 1

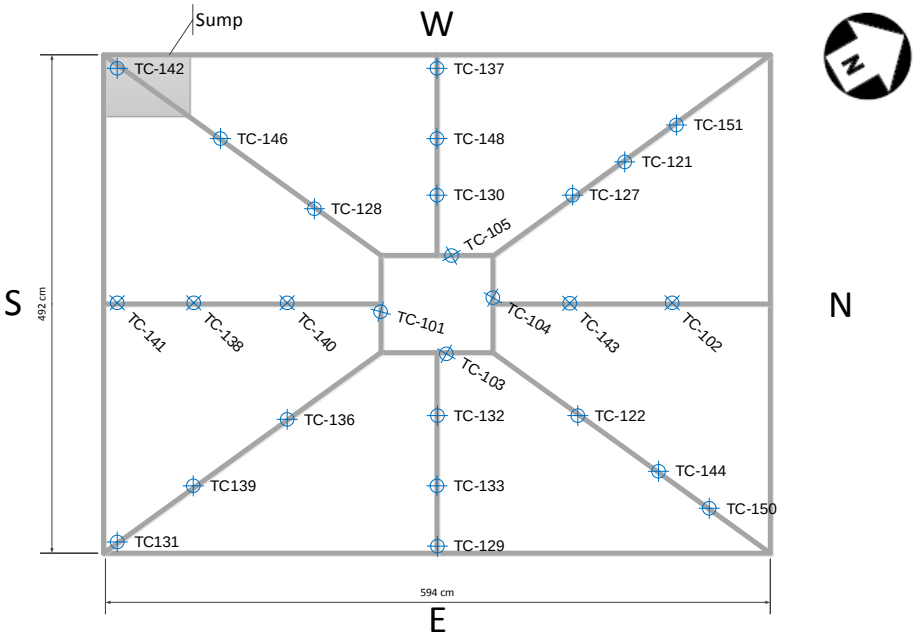

Figure 13: Radius thermocouple arrangement for Trial 2

Figure 14: Wooden thermocouple grid

Table 7: Location of all radius thermocouples

Tag name	Radius ± 2mm (cm)	Direction (ref: facility)
TC 103	86.39	East
TC 129	185.40	East
TC 132	40.87	East
TC 133	116.89	East
Spill point	0.00	None
TC 102	183.92	North
TC 104	61.92	North
TC 143	116.99	North
TC 122	126.63	North-East
TC 150	214.22	North-East
TC 144	176.45	North-East
TC 127	170.56	North-West
TC 151	268.84	North-West
TC 121	219.57	North-West
TC 101	172.34	South
TC 138	276.93	South
TC 140	222.85	South
TC 141	330.96	South
TC 136	201.33	South-East
TC 139	285.19	South-East
TC 131	350.00	South-East
TC 128	240.09	South-West
TC 146	332.48	South-West
TC 142	415.33	South-West
TC 105	52.89	West
TC 130	88.47	West
TC 137	285.00	West
TC 148	203.01	West

4.2.4.2 Pool level

Two types of sensors were initially set up to measure pool level during the LN_2 spill. The first level meter consists of a vertical array of thermocouples and the second consists of a bubbler meter. Although the bubbler meter worked when tested with water in lab, it did not indicate any level changes during the experiment. Hence, only readings from the former type of level meter was used.

In the first trial, a thermocouple level meter was located on the western wall of the pit. This location was chosen because the pit is sloped towards the sump located in the south-west corner of the pit, and we suspect that level detection will be earlier at the lower side. In the second trial, an additional thermocouple level meter was placed on the eastern wall of the pit to observe if the pool level varies from one wall to the other. The measurable heights by the level meters are of an accuracy of ± 0.5 mm and are shown in Table 8 for Trial 1 and Table 9 for Trial 2.

Table 8: Level meter thermocouple positions at Trial 1

Level meter	
Tag	Height ± 0.5 mm (cm)
TC 147	1.8
TC 149	3.8
TC 145	5.7
TC 126	8
TC 125	10
TC 118	12.9
TC 123	15.9
TC 120	18.7
TC 119	21.8
TC 124	24.9
TC 121	27.8
TC 144	31.1

Table 9: Level meter thermocouple positions at Trial 2

East Level Meter	
Tag	Height ± 0.5 mm (cm)
TC 147	1.8
TC 149	3.8
TC 145	5.7
TC 126	8
TC 125	10
TC 118	12.9
TC 123	15.9
West Level Meter	
TC 117	1.8
TC 134	4
TC 119	6
TC 152	10
TC 120	14
TC 125	18

4.2.4.3 Heat transfer under concrete

Embedded under the large concrete pit are a total of 100 thermocouples and 13 heat flux plates. Within the base, they are arranged in a 3 x 3 grid (see Figure 15) while they are arranged in a 2 x 3 grid within the walls (see Figure 16). The schematic diagram of each section (upper base, lower base, upper walls, lower walls) are displayed in Figure 17 to Figure 20. These locations and set of sensors were not changed during any of the trials.

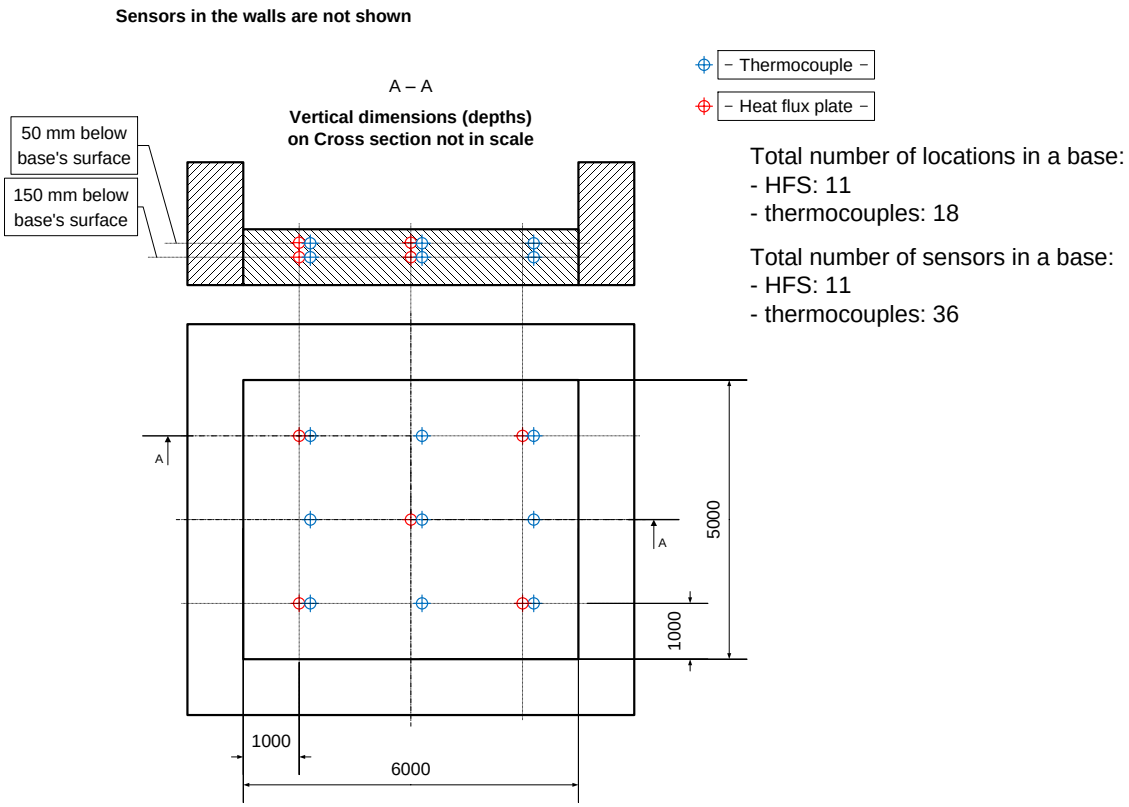

Figure 15: Schematic diagram of sensors embedded within the base of the concrete

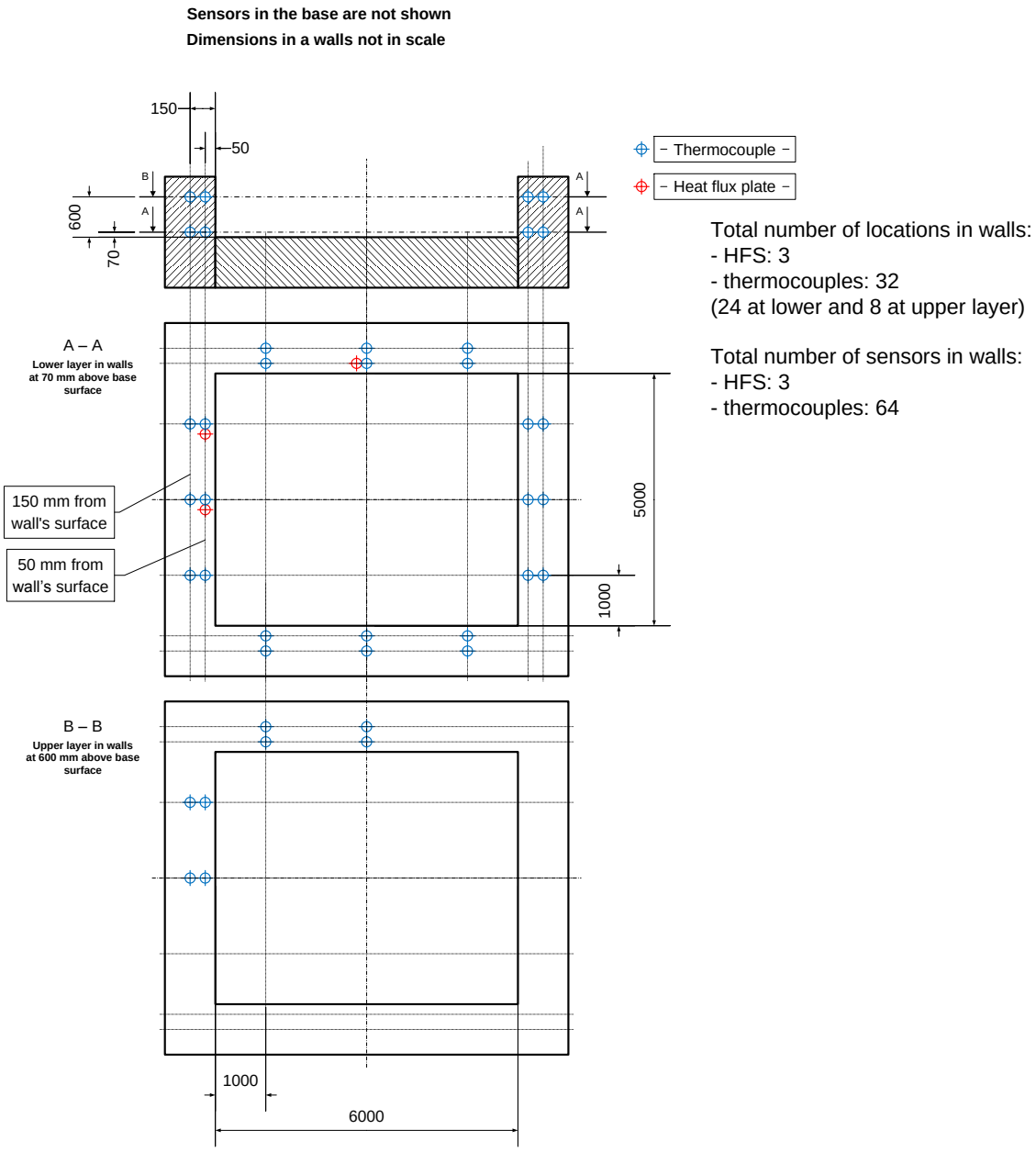

Figure 16: Schematic diagram of sensors embedded within the walls of the concrete pit

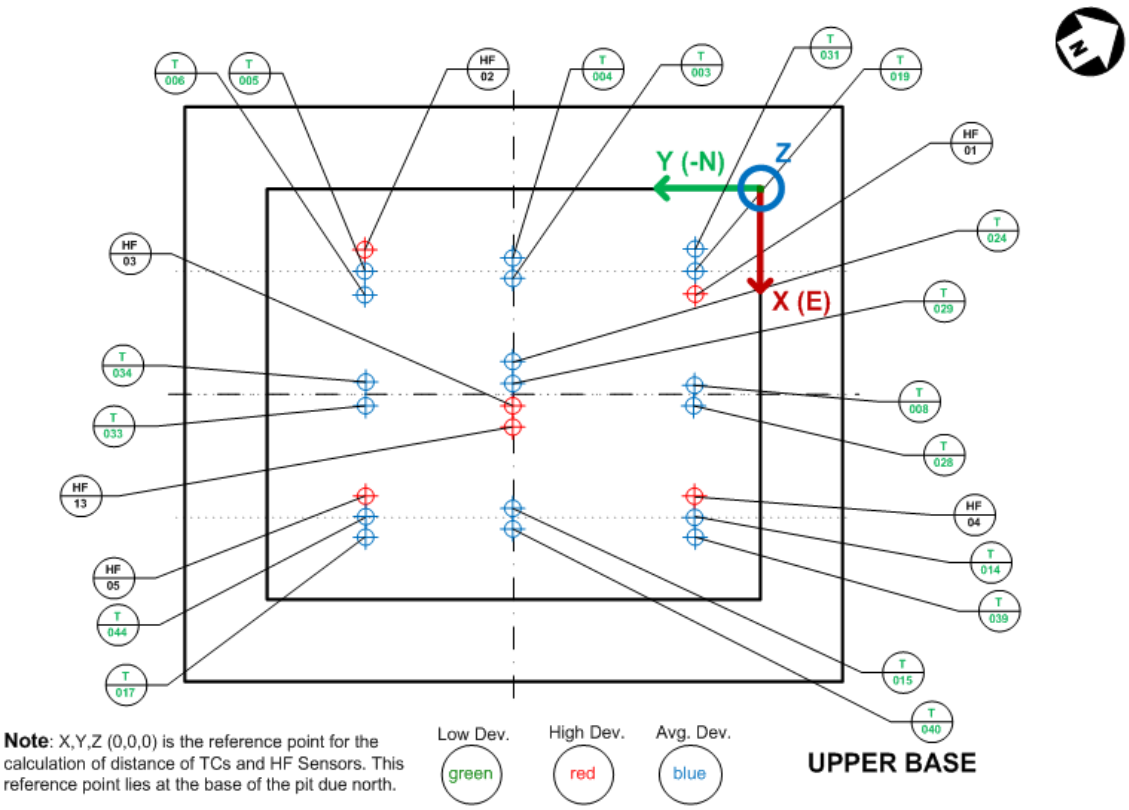

Figure 17: Schematic diagram embedded sensors in the upper base

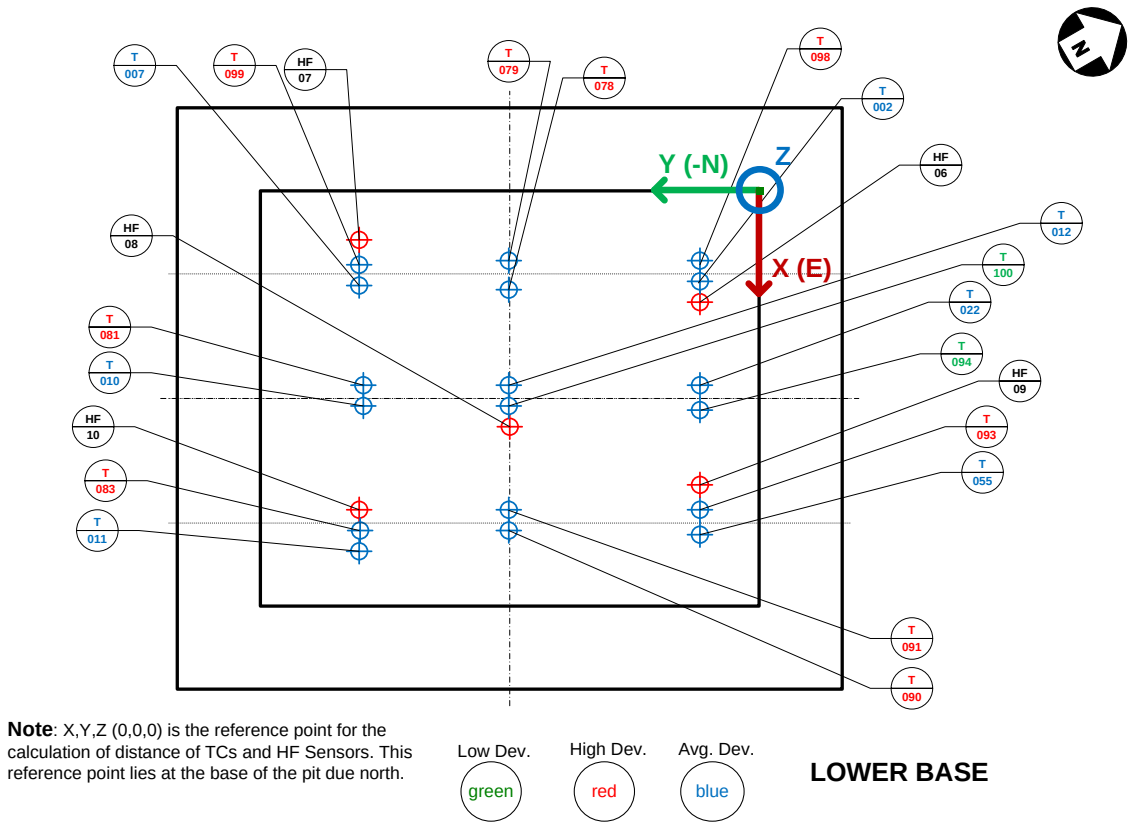

Note: X,Y,Z (0,0,0) is the reference point for the calculation of distance of TCs and HF Sensors. This reference point lies at the base of the pit due north.

Figure 18: Schematic diagram of embedded sensors in the lower base

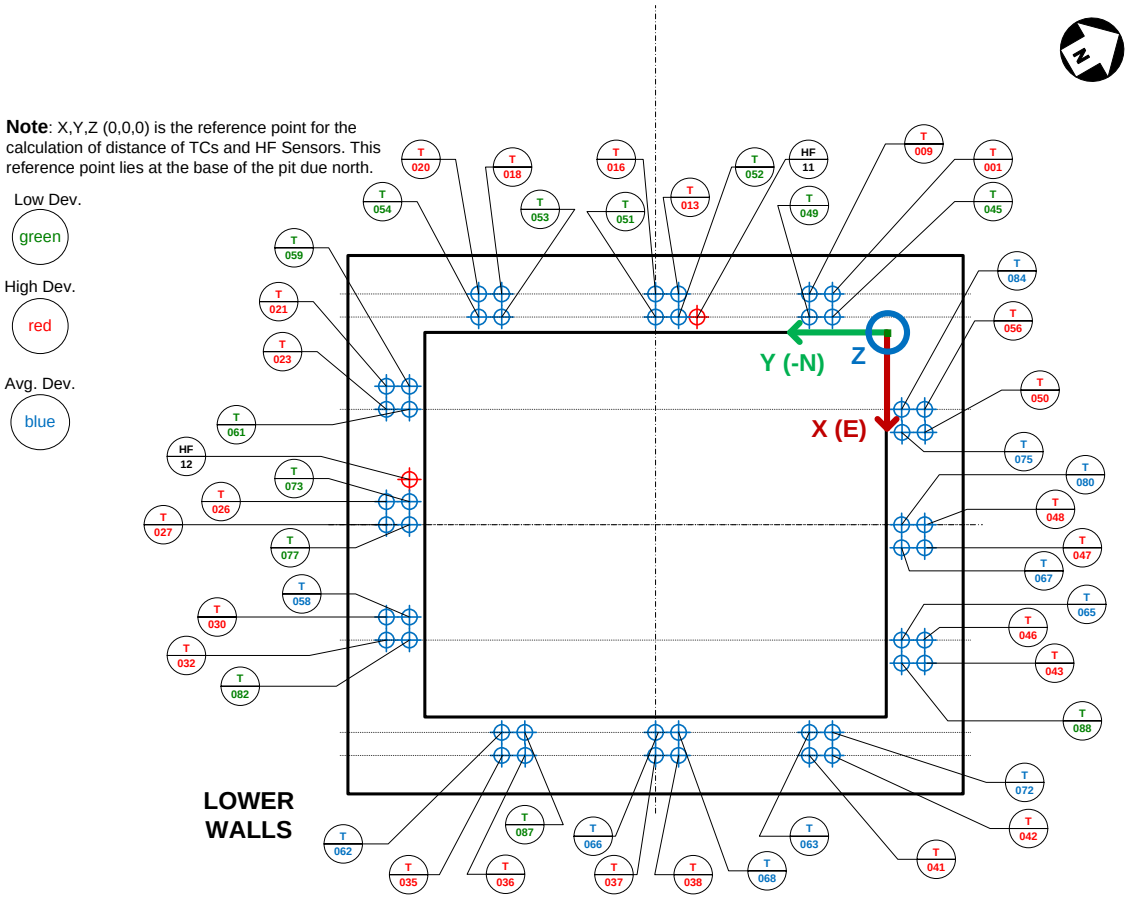

Figure 19: Schematic diagram of embedded sensors in the lower walls

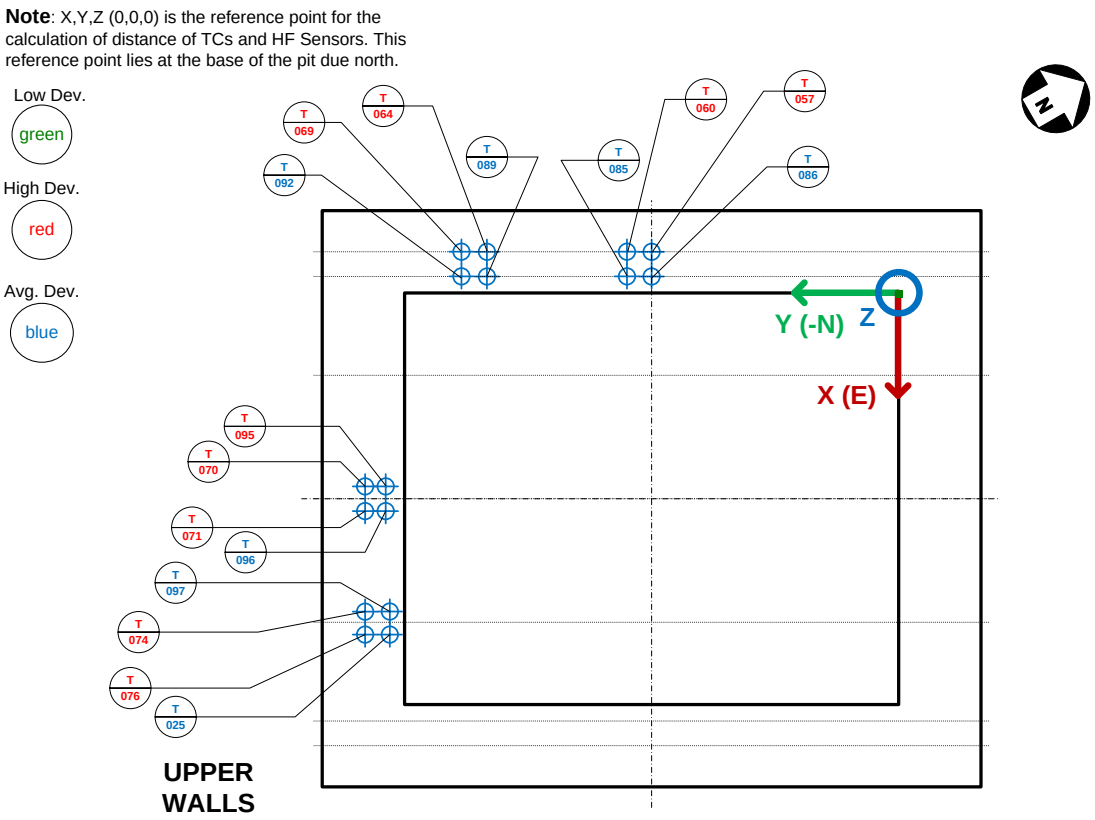

Figure 20: Schematic diagram of embedded sensors in the upper walls

4.2.4.4 Oxygen level

Seven oxygen detectors were located within the TP-5 vicinity to track the LN_2 vapor cloud for safety measures. These sensors were arranged according to the weather condition of the experiment. In the first trial, the wind speed was much faster and the oxygen gas detectors' locations were more dispersed.

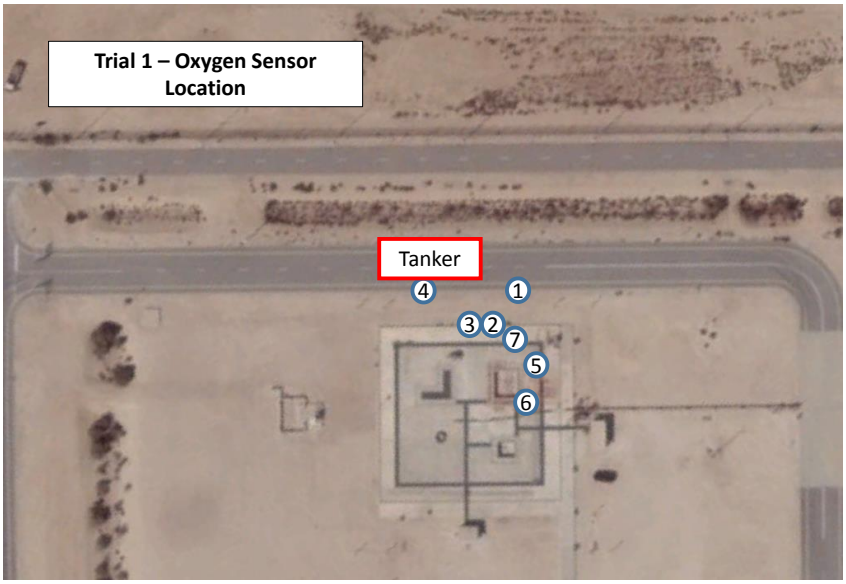

Figure 21: Location of oxygen gas sensors in Trial 1

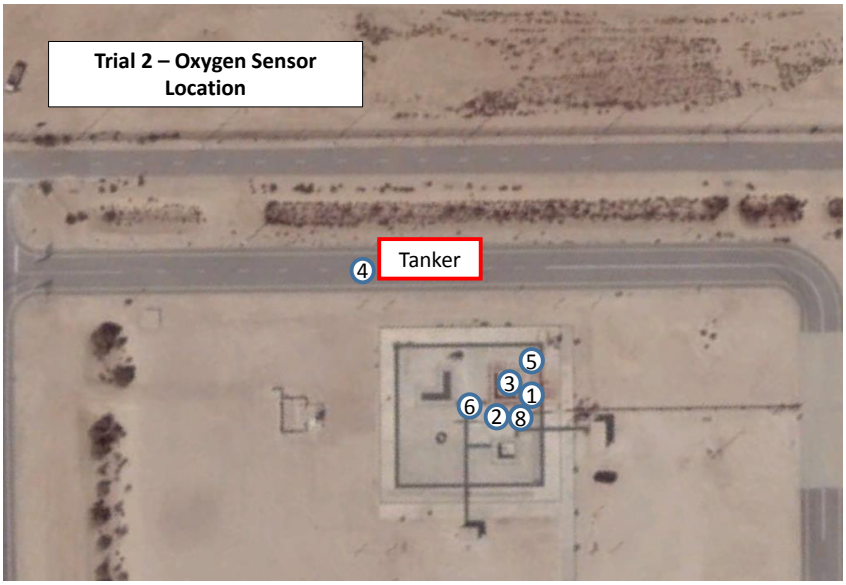

Figure 22: Location of oxygen gas sensors in Trial 2

4.2.4.5 Weather station

A stationary weather station was available to monitor the weather conditions throughout the experiment. It is capable of measuring precipitation, temperature, atmospheric pressure, humidity, solar radiation, electric field, and wind speed and direction. Table 10 displays the approximate height of each sensor.

Table 10: Weather station sensors

Sensor	Approximate height (m)
Rain gauge	0.5
Resistance Temperature Detector 1 & 2	2 and 10
Barometric pressure sensor	2
Pyranometer	2
Temperature and humidity sensor	2
3-D Sonic anemometer	2 and 10
Electric field meter	2

Figure 23: Weather station at TP-5

4.2.5 Uncertainty Analysis

Variables of interest were measured directly in this work. The variables consist of the pool temperature, concrete temperature, and the pool radius indicated by the thermocouples. There are two sources of error, a module error within the DAQ and the limit of the sensors' capabilities. Firstly, the thermocouples inside the concrete have an average standard deviation of 0.33 ^{o}C with a maximum of 1.85 ^{o}C. For thermocouples measuring pool temperature and radius, the averaged standard deviation of all thermocouples were 0.61 ^{o}C. Two radius thermocouples have a maximum standard deviation of 4.89 ^{o}C (TC-127 and TC-128). However, these thermocouples were not used to indicate pool temperature and rather used for pool radius. For the measurement of the pool radius, the uncertainty of selection of the point when the pool arrived at the thermocouple is ± 3 seconds. Additionally, the responsivity of the sensor to temperature change is indicated to be 50 ms

min floating point (temperature). Finally, the positioning of each thermocouple have an uncertainty of ± 2mm.

4.2.6 Discharge flowrate from the tanker

Pressure readings from the tanker were converted to indicate the amount of LN_2 left inside the road tanker. These readings were taken manually every few minutes until the tanker was empty. Figure 24 and Figure 25 display the spill rate from the tanker in Run 1 and Run 2 respectively.

During the first day, the tanker was at a pressure of 2 bar. Unexpectedly, despite keeping the pressure constant, the flowrate of the spill kept fluctuating. The theoretical flowrate of the spill was simulated through PHAST and was found to be 4.38 kg s^{-1}. The spill flowrate varied mainly between 0.4 to 2.5 kg s^{-1} throughout the experiment, exhibiting lower flowrates than the expected value.

In the second day, the tanker was maintained at 4 bar. As like the first day, the flowrate of the spill gradually increased from 1 to 3 kg s^{-1}. It was speculated that the flowrate starts off slow because heat from the cryogenic hose has vaporized the incoming LN_2. A vapor flow would be relatively slower than liquid as it is less dense. It is speculated that pure liquid was out only after 1 hour 12 minutes after spillage, though this is still half of the simulated value by PHAST at 6.1 kg s^{-1}. These details are summarized in Table 11.

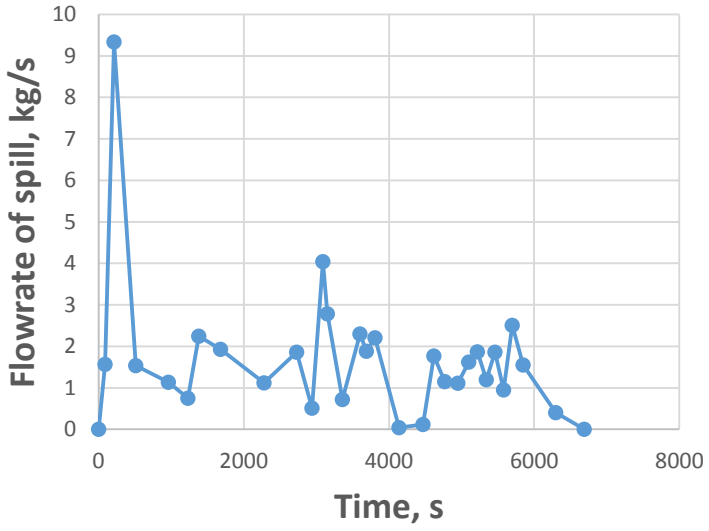

Figure 24: Flowrate of spill throughout Trial 1

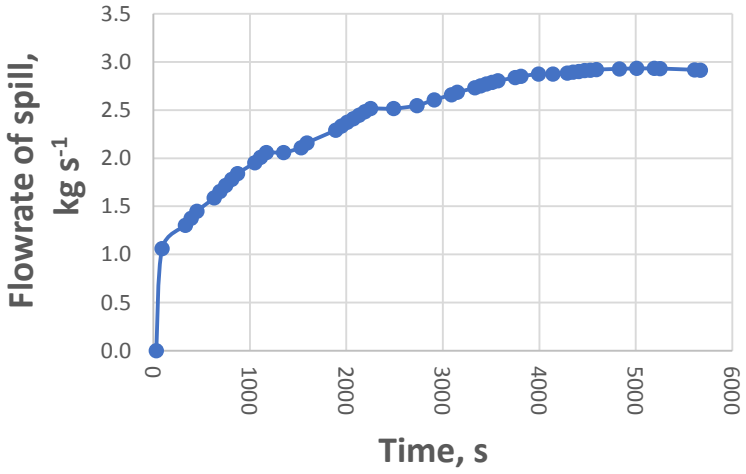

Figure 25: Flowrate of spill throughout Trial 2

Table 11: Summary of discharge flowrate of LN_2 in both trials

Trial number	Pressure	Theoretical flowrate, kg s^{-1}	Observed flowrate, kg s^{-1}
1	2 bar	4.38	0.4 – 2.5
2	4 bar	6.1	1 – 3

Vaporization within the cryogenic hose was suspected to be the explanation for the low observed flowrate. As nitrogen is denser in liquid form and lighter in vapor form, lack of insulation at the hose may have allowed heat to vaporize LN_2 before the spill reaches the pit.

Although fluctuations within the spill rate will cause inconvenience during modeling, existing models may need to be corrected to allow a tolerance of such situations.

4.3 Validation of the pool spreading model

To examine the validation of each model, each assumption to the model are tested. The first is the assumption that the pool is boiling throughout its life even for large spills. Using the input parameters recorded in the experiment, the pool radius estimated by the models are compared to the experimental data. This activity will justify whether the current assumptions incorporated in vaporizing pool spreading models are acceptable or not. Comparing the heat transfer through the concrete estimated by the one-dimensional conduction model against the temperature profile through across the concrete also gave insight on the applicability of the conduction models.

4.4 Experiment: Field-scale liquefied natural gas spill on concrete

LNG was spilled into the same pit as an extension of the experimental work. The setup to the experiment is identical, except that 23 m^3 LNG was delivered from a 1.5" diameter cryogenic hose connected to a 4" fixed pipe. Additionally, low concentration methane gas sensors and radiometers were positioned surrounding the pit to measure gas dispersion and fire radiation at various locations. As LNG was not readily available in Qatar, it was delivered just one month before the deadline of the project report. Extraction of data has been conducted but a detailed analysis remains as a near-future work.

In the first day of the LNG unloading, the same framework used for past LN_2 experiments remained inside the pit to measure pool radius and level. The same 100 thermocouples and 13 heat flux plates embedded under the concrete measured the temperature and heat flux profiles under the ground. The spill was located in the south-east corner of the pit as shown in Figure 26 and Figure 27.

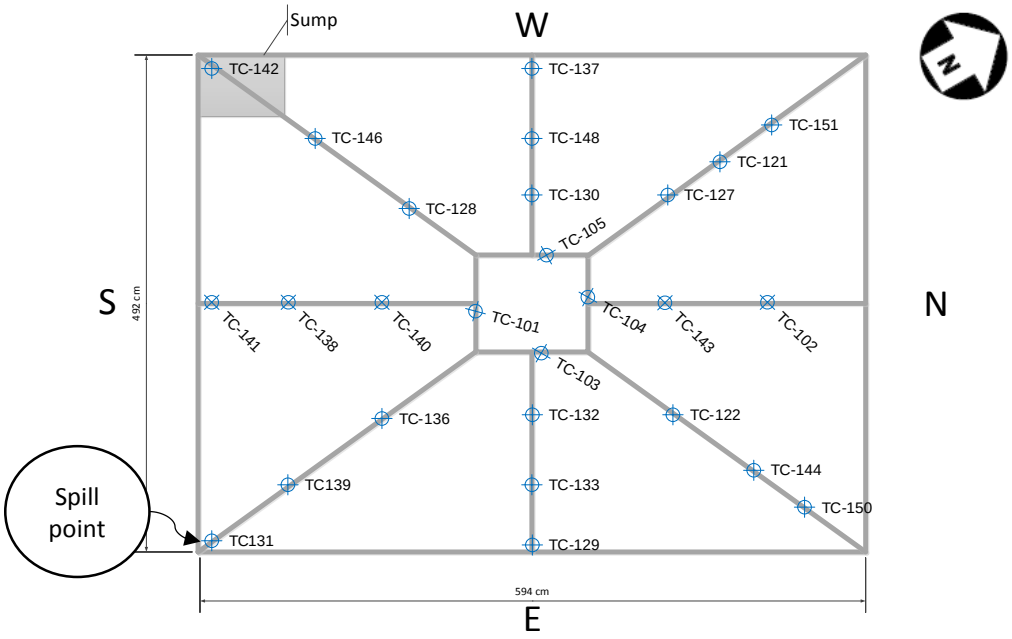

Figure 26: Radius thermocouple arrangement for LNG spill

Figure 27: Wooden thermocouple grid and hose position

4.4.1 Pool temperature

During the second day, all wooden framework was removed from the area as they would add fuel to the fire. Several thermocouples were positioned at different depths inside the pit to measure pool temperature as shown in Table 12.

Table 12: Thermocouple inside the pit during Day 2

Tag	Height (cm)
TC131	0
TC 149	1
TC 147	2
TC 145	2.5
TC 126	4.5
TC 123	10.5
TC 125	10.5
TC 118	13

4.4.2 Methane gas dispersion

Seven methane gas detectors, with specifications shown in Table 13, were positioned around the pit to measure the methane gas concentration and dispersion (Figure 28 and Figure 29). The sensor locations were determined according to the prevalent wind direction during the day. During the LNG fire experiment, only four methane gas sensors remained onsite so to avoid exceeding the sensors' temperature limit and disallowing them to become possible ignition sources for the LNG vapor cloud. The distances of each sensor are displayed in Table 14).

Table 13: Outline specification

Specification	
Measurement range	0 – 100 % LEL
Operational and Certified Temperature Range	-40ºC to 65ºC
Measuring range	4-20mA
Material	Stainless steel

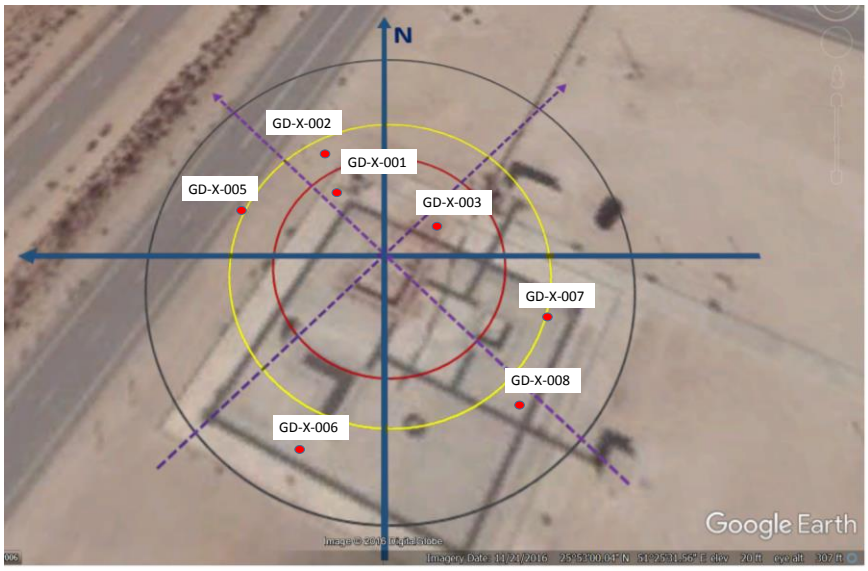

Figure 28: Bird-eye view of methane gas detector locations during LNG spill (Day 1)

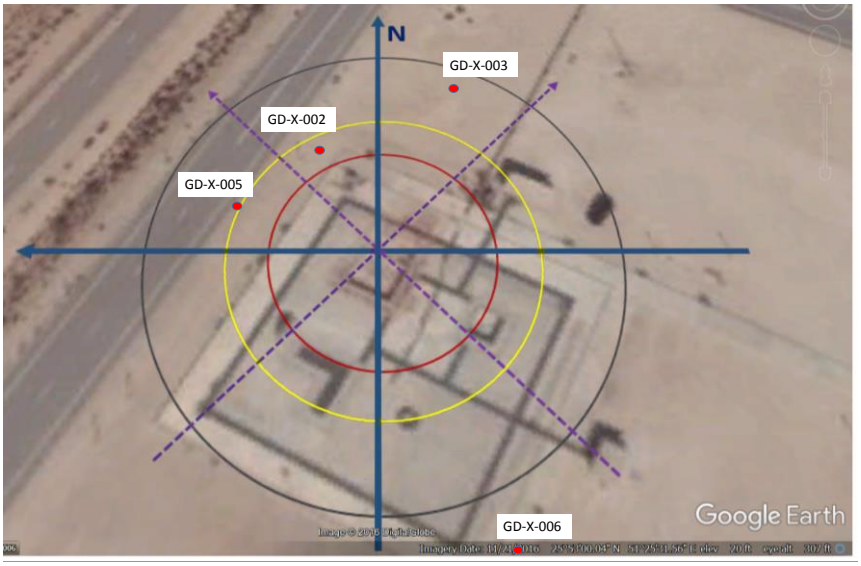

Figure 29: Bird-eye view of methane gas detector locations during LNG spill (Day 2)

Table 14: Distance of methane gas detectors from the pit

Sensor	Distance from the pit (m)		Height of sensor (m)
	Day 1	Day 2	
HGD-X-001	11.79	Removed	1.10
HGD-X-002	19.38	Removed	1.10
HGD-X-003	9.72	28.66	0.20
HGD-X-005	17.61	28.87	0.20
HGD-X-006	28.87	39.18	0.20
HGD-X-007	24.20	Removed	0.20
HGD-X-008	29.76	Removed	0.20

4.4.3 Fire radiation

A total of 12 radiometers of various working ranges shown in Figure 30 were located around the pit during both days of the LNG spill experiment. The radiometer range

varied from 5 to 200 kW m^{-2}. Those which were of higher range were positioned closer to the pit. The specification of the radiometers are shown in Table 15. The radial distances of each radiometers from the pit were determined by a computational simulation in PHAST. The radiometer positions are displayed in

Table 16 and Figure 30. All radiometers were installed at a 1.4 m height from the ground.

Table 15: Specification of radiometers

Specification	
Working ranges	5, 50, 200 kW m^{-2}
Temperature range cooling water	10 to 30°C
Cooling water flow	> 10 L/hr
Output signal	> 5 mV at working range
Field of view	180 degrees
Maximum range	150% of working range

Table 16: Radiometer working ranges

Name	Range (kW m^{-2})	Distance from northwest corner of pit (m)
RF-X-001	50	28.35
RF-X-002	200	16.50
RF-X-003	5	28.86
RF-X-004	5	38.10
RF-X-005	50	27.50
RF-X-006	200	5.36
RF-X-007	50	22.23
RF-X-008	200	10.30
RF-X-009	50	27.37
RF-X-010	50	10.43
RF-X-011	200	10.30
RF-X-012	200	12.29

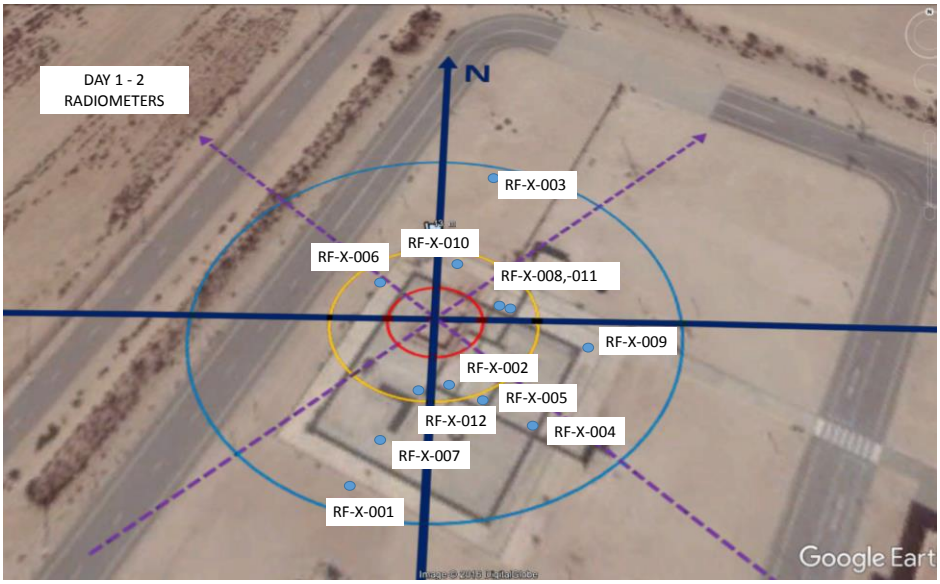

Figure 30: Bird-eye view of radiometer locations during LNG spill (Day 1 and 2)

Cooling water was supplied from a nearby fire hydrant. The design of the water network is shown in Figure 31 and Figure 32. The water network consisted of 12 water valves connected in series through 11 tee-connectors. Between the fire hydrant valve and the 12 water valves were a reducer and a pressure indicator. The pressure rating of each valve and connector were approximately 10-15 bar, which was the discharge pressure of the fire hydrant. Connected to each water valve were 1/8" of silicone tube connected to a radiometer. The tube was tightened using Swagelok fittings. Each cable and tube was insulated using fireproof sleeves.

The cooling water flow rate through the radiometer was the most crucial design aspect. A flow that was too fast would not provide a long enough cooling time. Likewise, a flow that was too slow would not be able to remove heat quickly enough. The minimum cooling water rate was indicated to be 10 L hr^{-1} (Table 15). The water flowrate was tested by

measuring the rate at which water filled a certain volume of a beaker at the end of the silicon tube. The current design was successful at delivering water at the required range.

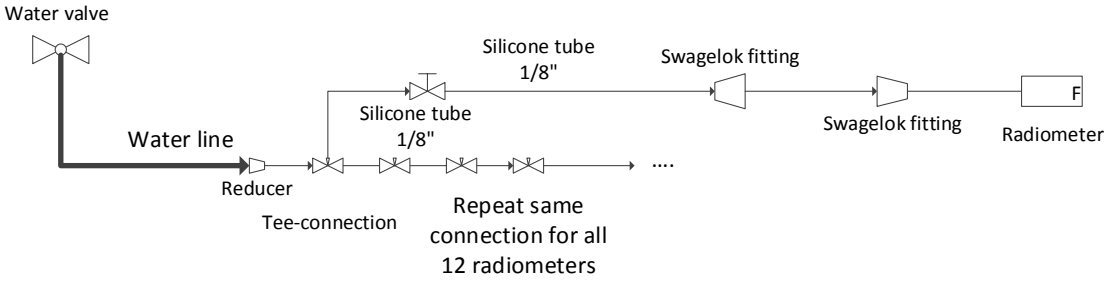

Figure 31: Schematic diagram of water line network

Figure 32: Cooling water supply to radiometer

5 SPREADING AND VAPORIZING MODEL

A spreading, vaporizing pool spreading model was implemented into Matlab in order to analyze its validity for cryogenic spills. The model is based on Webber and Brighton's integral solution for vaporizing spreading pools.

5.1 Governing equations

There are three cases that the model simulated. The first case is the prediction of pool spreading for non-volatile/non-vaporizing liquids. The second and third cases are the prediction of spreading for a vaporizing pool, assuming ideal one-dimensional conductive heat transfer from the surface. The boundary conditions of cases 2 and 3 are different. In the second case, heat transfer to the pool were the same everywhere as if it was at the center of the pool (Equation 10). In the third case, however, the temperature difference was calculated at each time step to take into account shorter exposure durations in the outer rings of the pool during pool spreading (Equation 15). The main assumptions to both conduction equations, which are to be validated in this thesis, are the perfect thermal contact between the ground and the pool and the ambient ground temperature outside of the pool.

The pool spreading model, applied in all three cases, consists of an improved integral solution of the shallow water equation taking into account friction forces and vaporization and is shown from Equation 11 to Equation 14. They are equations within the Gas Accumulation over a Spreading Pool (GASP) model. In this work, the study of the early pool spreading stage (gravity-inertial regime) has been neglected because the effect of liquid inertia is momentary. The last pool spreading stage (surface tension-viscous regime) has also been discounted as it is an unlikely regime for cryogenic spills on land.

Three final sets of models were generated through the coupling of the pool spreading and the vaporization terms. Model 1 is the pool spreading equations without a vaporization term. Model 2 is used to refer the coupling of the pool spreading equations with the "simple 1D conduction" equation. Lastly, Model 3 is the combination of the pool spreading equations with the "Webber 1D conduction" equation. It is expected that the non-vaporizing pool will spread farther than vaporizing pools. The model which utilizes "Webber 1D" conduction model should predict higher vaporization rate and smaller pool radius than that which assumes "simple 1D" conduction from the substrate. The summary of these models are shown in Table 17.

Table 17: Summary of model

Model	**Model 1**	**Model 2**	**Model 3**
Pool Spreading	GASP pool spreading equations Equation 11 to Equation 14	GASP pool spreading equations Equation 11 to Equation 14	GASP pool spreading equations Equation 11 to Equation 14
Vaporization	No vaporization	"Simple 1D conduction" Equation 10	"Webber 1D conduction" Equation 15

5.2 Numerical solution and algorithm of solution

The pool spreading model was solved using an *ode23* solver, a low order method to non-stiff differential equations. Within the solver, the one-dimensional equation was solved internally to give the pool vaporization rate. An optimization function was incorporated in the solver to stop calculations when the mass reaches zero. The second

optimization done to the model was the storage of previous successful solutions of the solver in order to take into account the progression of the pool radius into the heat conduction equation. All of these information are displayed in the flow diagram in Figure 33. The input data to the model and temperature dependent parameters are listed in Table 18 and Table 19 respectively. The key to reading the flow diagram is in

Table 20.

The algorithm is as follows:

1. The input data are inserted into the model
2. Temperature dependent properties are calculated
3. The model goes inside *funMMEBalance*, where the ordinary differential equations (ODE) are stored. The initial radius, height, and velocity values are sent to *funFriction* and *funGravity* functions, where the gravity and friction terms will be calculated
4. The gravity and friction terms of the pool spreading model is calculated given the liquid density, dynamic viscosity, velocity, pool depth, and radius through *funFriction* and *funGravity*
5. The function *funBoiling* receives the current value of time and radius
6. *funIntegral* stores all values of radius
7. If the "Webber 1D" conduction model was set as the *BoilType* data, then *funIntegral* is activated to calculate the integral term in Equation 15
8. If the "simple 1D" conduction model was set as the *BoilType* data, then Equation 10 is calculated directly in *funBoiling*
9. *funMMEBalance* receives the value of conductive heat transfer from *funBoiling*
10. The set of ordinary differential equations (solving radius, mass and velocity) are sent to the *ode23* solver, outputting the value of radius, mass, and velocity
11. Steps 3 – 10 are repeated until the end of the calculation
12. Graphs of variables of interest are generated

Table 18: Input parameters to the model

Input parameters	Input type
Substrate type	"Concrete"/ "water" (Select substrate)
Roughness of substrate	"Smooth"/ "rough"/ "liquid" (Select substrate texture)
Liquid	"Methane"/ "nitrogen" (Select liquid)
Initial temperature of substrate	(Ambient temperature of substrate in Kelvins)
Initial time (for model calculation)	(Starting calculation time in seconds)
Final time (for model calculation)	(Ending calculation time in seconds)
Initial *h/r* ratio	(Ratio of height to radius of the tank)
Spill type	Continuous/instantaneous
Spill time	(Duration of spill in seconds)
Discharge rate	(Spill rate in $m^3 s^{-1}$)
Initial volume	(For instantaneous spills, initial volume of spill in m^3)
Boiling type	"Webber 1D" / "simple 1D"/ "no vaporization" (Select conduction equation)
Maximum radius (if bund exists)	(Maximum pool radius in m)

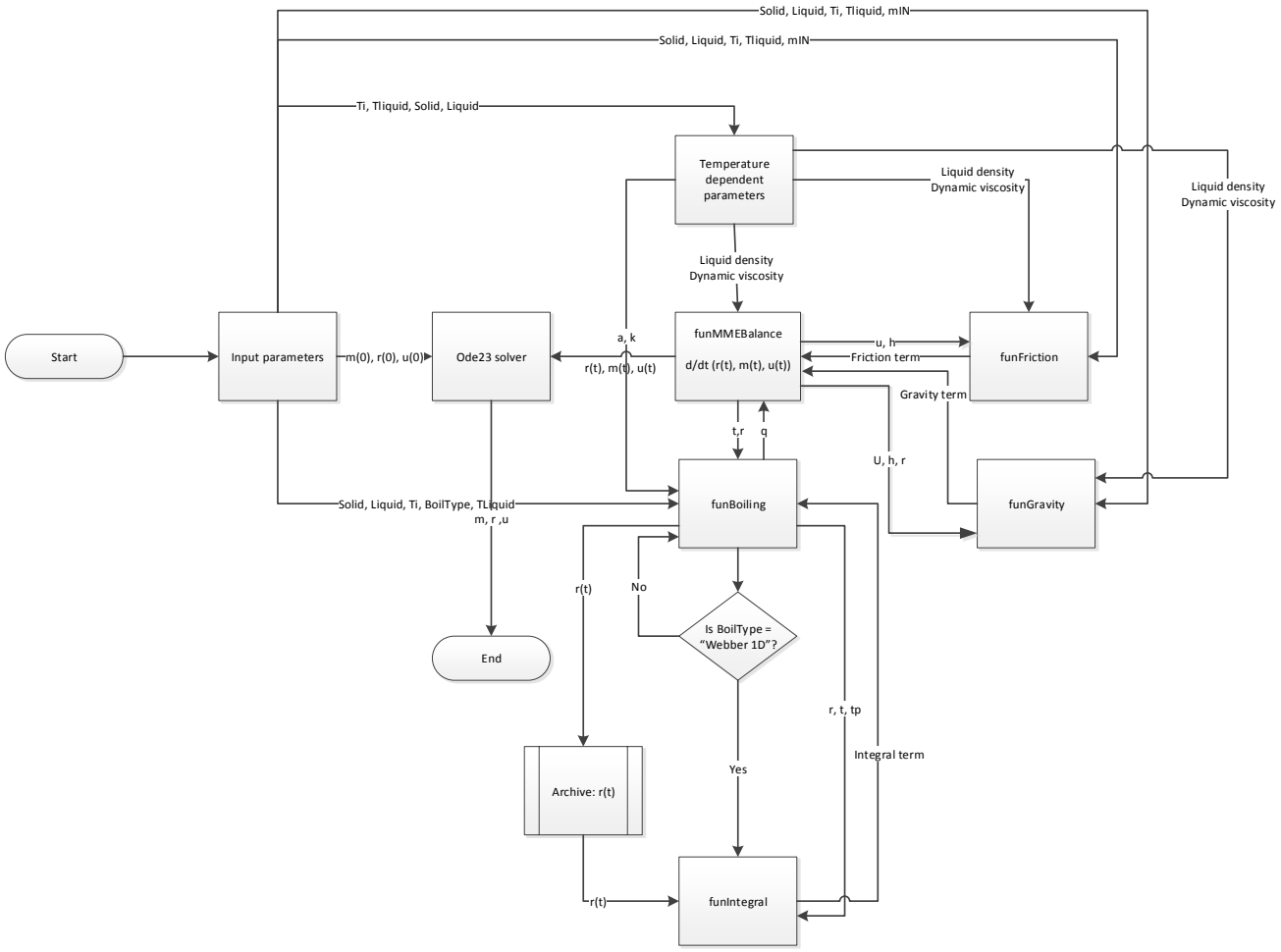

Figure 33: Flow diagram of the model

Table 19: Temperature dependent parameters

Temperature dependent parameters	Detail
Specific heat capacity of substrate	Calculated at 1.013 bar as a function of temperature Source: DIPPR
Critical properties of liquid	Calculates molecular weight (g mol^{-1}), critical temperature (K), critical pressure (mPa), critical density (kmol m^{-3}), acentric factor, normal boiling point at 1.013 bar(K) and dipole-dipole moment
Dynamic viscosity	Calculated as a function of temperature at 1.013 bar Source: BYU-DIPPR
Thermal properties of substrate	Calculates thermal diffusivity (m^2 s^{-1}) and thermal conductivity (W m^{-1} K^{-1}) according to published/available substrate data (to be specified by the user or assumed using available literature data)

Table 20: Flow diagram parameters

Parameter symbol	Meaning
h	Pool depth, m
Liquid	Liquid name
m	Mass, kg
mIN	Input flowrate, kg s^{-1}
t	Time, s
r	Radius, m
u	Velocity, m s^{-1}
Ti	Initial temperature of ground, K
Tliquid	Boiling temperature of liquid, K
Solid	Substrate name

5.3 Verification and validation of pool spreading and vaporization model

The verification and validation of model algorithm in this project was done in three stages. The first stage consists of verifying the pool spreading model and the heat conduction models separately. Then, the model is validated for a non-vaporizing spreading pool, vaporizing non-spreading pools, and simultaneously vaporizing spreading pools.

5.3.1 Verification of the conduction model

The simple 1D equation derived from Fourier's one-dimensional conduction equation is one that can be simplified to the form of $At^{-1/2}$. This is also the case for the "Spreading 1D" conduction equation when its area is set to a constant, which occurs when the pool is not spreading, as the second term within the equation cancels out. Experimentally, the proportionality with $t^{-1/2}$ is also observed with boil-off data of LNG on concrete, as published by R C Reid and Wang (1978). The verification of the conduction model with $t^{-0.5}$ is shown in Figure 34.

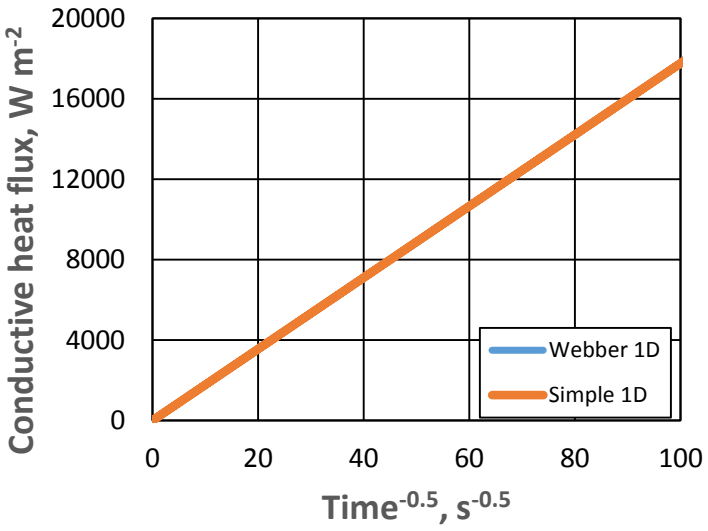

Figure 34: Verification of the Simple 1D conduction model

5.3.2 Verification of non-vaporizing pool spreading model

The non-vaporizing pool spreading model (Model 1) was verified for the trends at early and late stage of pool spreading, for both, instantaneous and continuous releases, which gives four different cases to verify.

An instantaneous spill is modeled by assuming that a body of volume V_0 is released immediately to the ground. When the initial radius is set to 0, the model faces matrix singularity issues. The initial pool radius for an instantaneous spill is thus a non-zero value which satisfies the initial volume. This model assumes a value of 3/2 for height to radius ratio of a cylindrical tank.

The following trends are expected for non-vaporizing instantaneous spill of a fixed volume. The model should initially start with $r \sim t^2$ (Figure 35) when resistance is negligible and continue to spread indefinitely with an asymptote of the form $r \sim t^{1/7}$ (Figure 36), when the gravity balances the resistance (Webber and Brighton, 1987). These trends have been explained in detail by Webber and Brighton (1987).

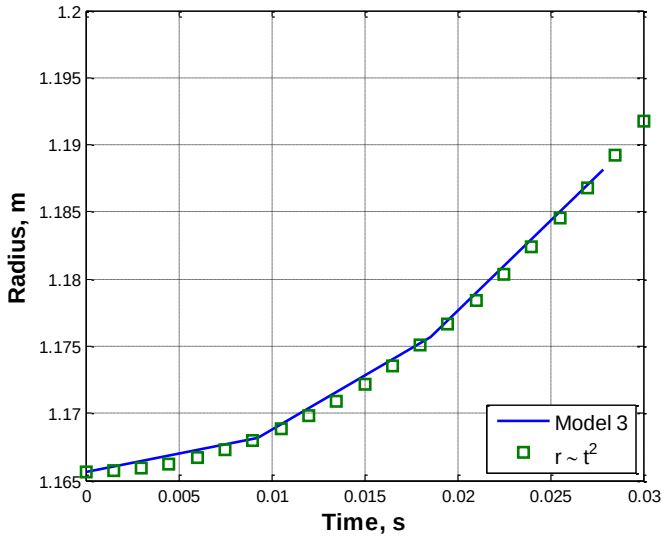

Figure 35: Similarity to $r \sim t^2$ behaviour for a non-vaporizing instantaneous release

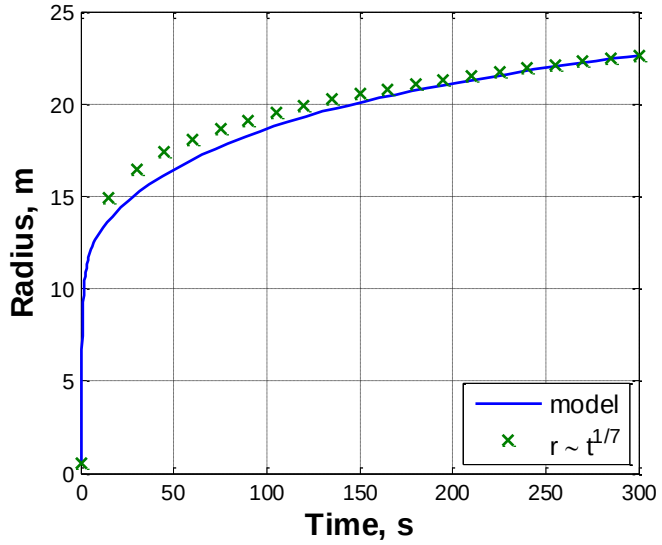

Figure 36: Similarity to $r \sim t^{1/7}$ behaviour for a non-vaporizing and instantaneous release

Similarly, the following trends are given by the model for continuous non-vaporizing spills. At early periods, the inviscid regime is implied by the $r \sim t^{3/4}$ regime (Figure 37) when the viscosity is insignificant and only inertia plays a role in resisting the flow. This relationship was derived from the Navier-Stokes equation for an inviscid, dense, axisymmetric, incompressible fluid and the continuity equation (Britter, 1979). For continuous spills, no justified trends has been found at the later stages of the spill.

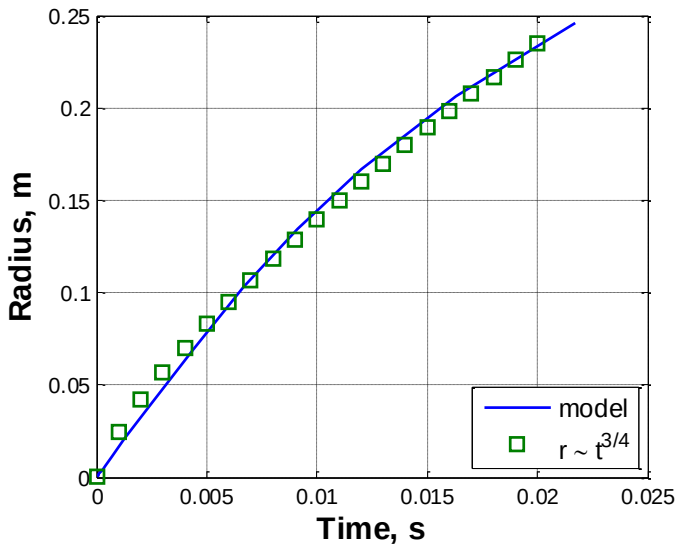

Figure 37: Similarity to $r \sim t^{3/4}$ behaviour for a non-vaporizing and continuous release

5.3.3 Validation of the vaporization model

In this work, the conductive heat flux equation obtained from GASP, the "Webber 1D" equation, has been solved numerically, while the "simple 1D" model was solved analytically. The model was described in detail in Section 5.1. Validation of the algorithm is done by comparing solution of this model to existing cryogenic vaporization data: liquid nitrogen in Section 5.3.3.1 and LNG in Section 5.3.4.

5.3.3.1 Validation with liquid nitrogen spill on smooth concrete (Sadia *et al.*, 2015)

The "Webber 1D" and "simple 1D" models have been validated with lab-scale LN_2 spills on smooth concrete. A total of 1000 g of LN_2 was spilled instantaneously into a slab of smooth concrete with dimensions 0.3 × 0.3 × 0.05 m by Sadia *et al.* (2015). Conduction from the walls have been deducted through the measurement of heat flux sensors. The boil-off rate was calculated by recording the change in mass.

Table 21: Input data for lab-scale experiment by Sadia et al.

Input data from Sadia et al.	
Liquid	Nitrogen
Initial volume, m^3	0.00124
Spill type	Instantaneous
Thermal conductivity, W m^{-1} K^{-1}	1.1
Thermal diffusivity, m^2 s^{-1}	5.96×10^{-7}
Density of liquid, kg m^{-3}	808
Initial ground temperature, ^oC	23
Additional assumptions	
Initial h/r ratio (shape of cylindrical tank)	1.5
Ground	Smooth concrete
Maximum radius (bund), m	0.15

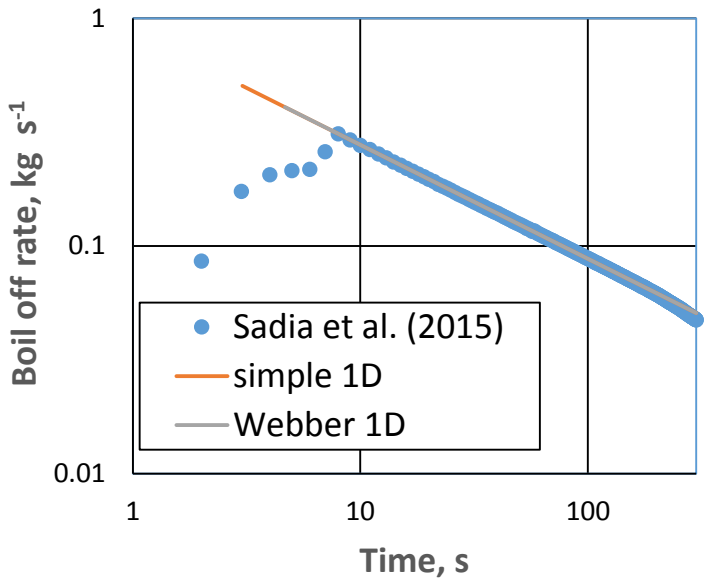

Figure 38: Models prediction of the boil-off rate of LN_2 (Sadia et al., 2015)

Both conduction models agrees with the experimental boil off rate most of the pool life and highly over predict the boil-off rate at times less than 1 second, as shown Figure 38.

5.3.4 Validation with liquefied natural gas spill on concrete

The boil-off rates of LNG from lightweight and dry standard concrete of various moisture contents have been provided in a paper by Lang *et al.* (1980). Contrastingly, water moisture is not taken into account within both models. The 1D conduction model does not take into account the moisture content of the concrete and thus assume the concrete is dry. The input data are summarized in Table 22. The boil-off rate predictions of the 1D conduction model (black line in Figure 39) agree with the result obtained by Lang *et al.* (1980) for dry standard concrete (black points), although it slightly under estimated their result. The result may not be completely accurate as the thermal properties of the concrete was assumed to be the same Moorhouse and Carpenter (1986)'s pool spreading

experiment (a validation exercise done in Section 5.3.6.1). The concrete properties were not explicitly defined for this experiment and may differ.

Table 22: Input data for LNG vaporization on concrete from Lang et al. (1980)

Input data from Lang et al. (1980)	
Liquid	Methane
Initial volume, m^3	3.36
Spill type	Instantaneous
Density of liquid, kg m^{-3}	460
Initial ground temperature, ^oC	20
Additional assumptions	
Initial h/r ratio (shape of cylindrical tank)	3/2
Ground	Smooth concrete
Thermal conductivity, W m^{-1} K^{-1}	1.7
Thermal diffusivity, m^2 s^{-1}	5×10^{-7}

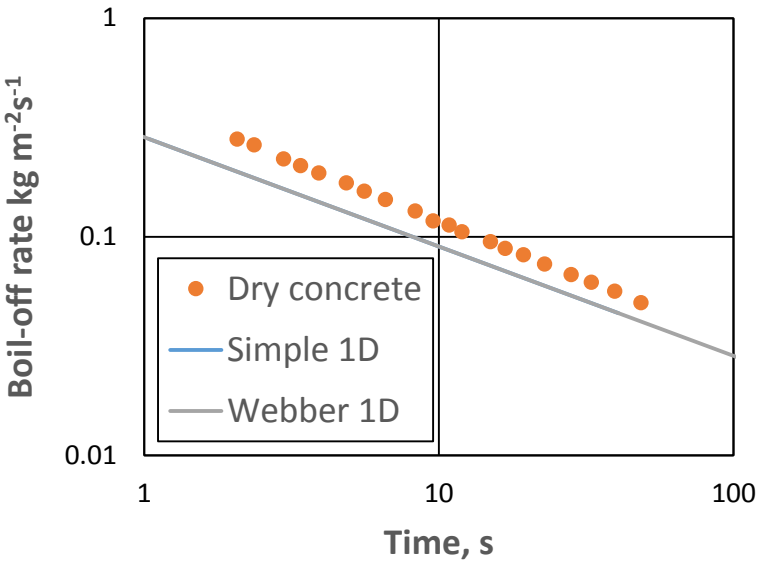

Figure 39: Simple 1D and Webber1D against LN_2 boiling on concrete(Lang *et al.*, 1980)

5.3.5 Validation of non-vaporizing pool spreading model

The pool spreading model was validated exclusively against experimental data by Belore *et al.* (1986). In this set of data, water was spilled continuously at the center of a plywood surface of 3 × 3 m^2. The spill rate was managed by adjusting the nozzle size. In this test, the spill rate was maintained at 1.19 kg s^{-1}. The pool radius was measured by the arrival timing of the pool front at flow depth markers located at known distances. The test have been repeated to verify its reproducibility. The thermal conductivity and diffusivity of plywood were assumed and based from Incropera and DeWitt (1996) at 300 K. The summary of the simulation input data is shown in Table 23.

Table 23: Simulation input data for Belore and McBean (1980)

Input data from Belore and McBean (1980)	
Liquid	Water
Spill rate, kg s^{-1}	1.19
Spill duration, s	60
Spill type	Continuous
Density of liquid, kg m^{-3}	1000
Initial ground temperature, ^{o}C	21.85
Ground	Plywood
Additional assumptions	
Initial h/r ratio (shape of cylindrical tank)	3/2
Thermal conductivity*, W m^{-1} K^{-1}	0.087
Thermal diffusivity*, m^2 s^{-1}	1.563×10^{-7}
***: Taken from Incropera and DeWitt (1996)**	

From Figure 40 it can be observed that the model curve lies in the middle of the experimental data.

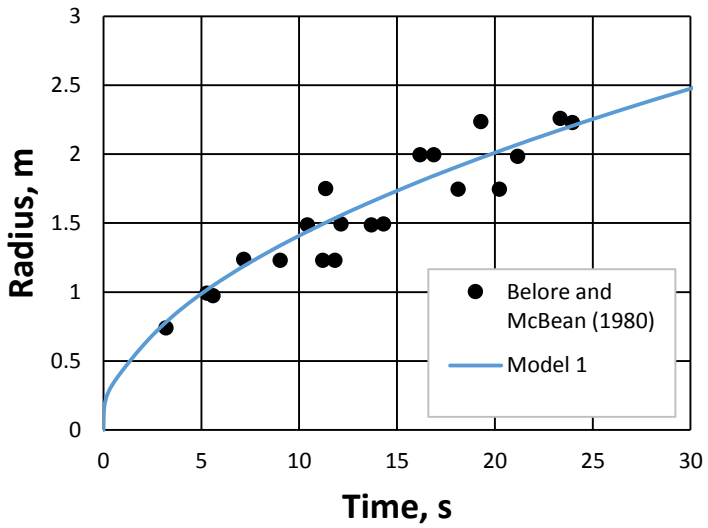

Figure 40: Comparison of Model 1 simulation with spreading of water on plywood

5.3.6 Validation of pool spreading model for vaporizing pool

In the last stage, vaporizing pool spreading spills were simulated. In each analysis the pool spreading model was coupled with either the "simple 1D conduction" (Model 2) or "Webber conduction" for 1D heat conduction (Model 3).

5.3.6.1 Moorhouse and Carpenter (1986)

The input data of Moorhouse and Carpenter (1986) is displayed in Table 24. LNG was spilled at a rate of 17 tonnes min^{-1} into the apex of a 45° sector. Model 2 was inputted into two modeling programs, Matlab and Polymath, to verify the equations were properly implemented and the solution was independent of the solver and solving method.

Table 24: Input data to the calculation for continuous release of LNG

***Input data from* Moorhouse and Carpenter (1986)**	
Liquid	Methane
Discharge rate, $m^3 s^{-1}$	0.0112
Spill time, s	300
Density of liquid, $kg m^{-3}$	460
Initial ground temperature, ^oC	20
Additional assumptions	
Initial h/r ratio (shape of cylindrical tank)	1.5
Ground	Smooth concrete
Thermal conductivity, $W m^{-1} K^{-1}$	1.7
Thermal diffusivity, $m^2 s^{-1}$	5×10^{-7}

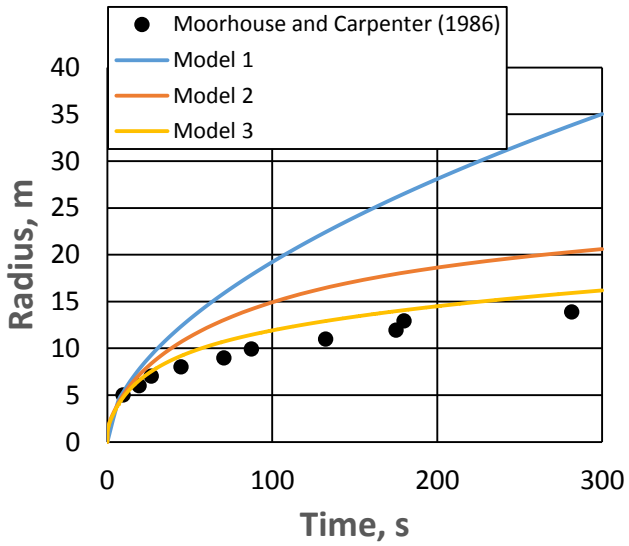

Figure 41: Validation with Moorhouse and Carpenter (Model 1 to 3)

Pool radius calculations from Models 1 to 3 were compared against the experimental data, as shown in Figure 41. Model 1 over predicts the radius by a large margin as much of the

pool has vaporized as the pool grows, reducing the pool radius. Model 2 (blue line) does take into account vaporization and provides a much closer prediction to the data as it assumes ideal one-dimensional conduction from the ground. On the other hand, it consistently exhibits overestimation of pool radius throughout the pool life. Model 3 (orange line), which takes into account the different exposure time at the outer rings as the pool spreads, indicates much better agreement with the experimental data although the overestimation is still present. The solution generated by Polymath was also found to be reproducible with one from Matlab (the yellow line overlaps with the blue line), indicating that the algorithm used was inputted correctly.

5.3.6.2 Nguyen et al. (2015)

Nguyen *et al.* (2015) investigated cryogenic pool spreading by spilling LN_2 through a funnel on a concrete plate. The plate is of radius 0.8 m and thickness 0.025 m. The container of the plate rested on a balance with a resolution of 0.1 g. A total of six trials were conducted. Nozzles of dimensions of 6 mm, 8 mm, and 10 mm were used to adjust the maximum spill rates between 3.4×10^{-2} kg s^{-1}, 5.6×10^{-2} kg s^{-1} and 9.0×10^{-2} kg s^{-1} respectively. A total of 7.5 L of LN_2 was spilled in each trial. As discussed in Section 2.2.6, the method used to maintain the spill flowrate was questionable, as there was no mention of keeping the liquid head constant.

Table 25: Input data of simulation to Nguyen et al.. (2015) data

Input data	Case 1 and 2	Case 3 and 4	Case 5 and 6
Spill rate, kg s^{-1}	3.4×10^{-2}	5.6×10^{-2}	9.0×10^{-2}
Duration, s	120	80	60
Liquid	Nitrogen	Nitrogen	Nitrogen
Additional assumptions			
Thermal conductivity*, W m^{-1} K^{-1}	1.7	1.7	1.7 W
Thermal diffusivity*, m^2 s^{-1}	5×10^{-7}	5×10^{-7}	5×10^{-7}

* : data not given by Nguyen *et al.*. (2016) and taken from Moorhouse and Carpenter (1986)

Table 25 displays the input data for the simulations done in Figure 42 to Figure 44. As thermal conductivity and diffusivity was not specified in the paper, their values have been assumed to be the same as Moorhouse and Carpenter (1986)'s data.

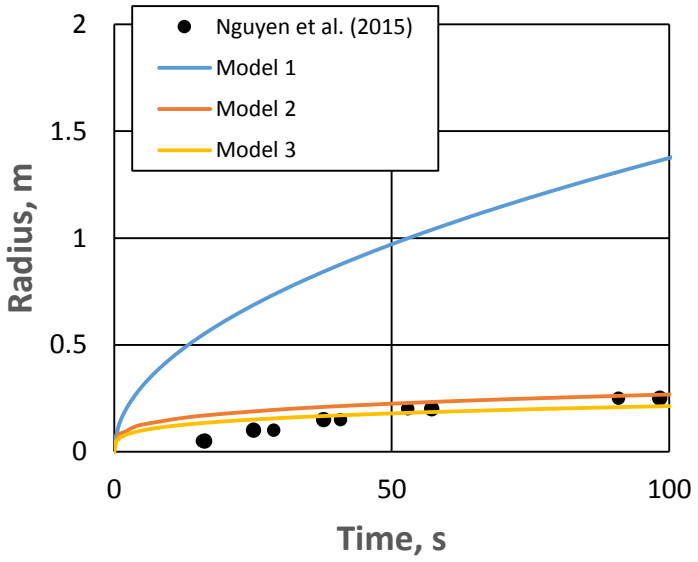

Figure 42: Validation of Model 1, 2, and 3 against pool spreading data (Case 1 and 2)

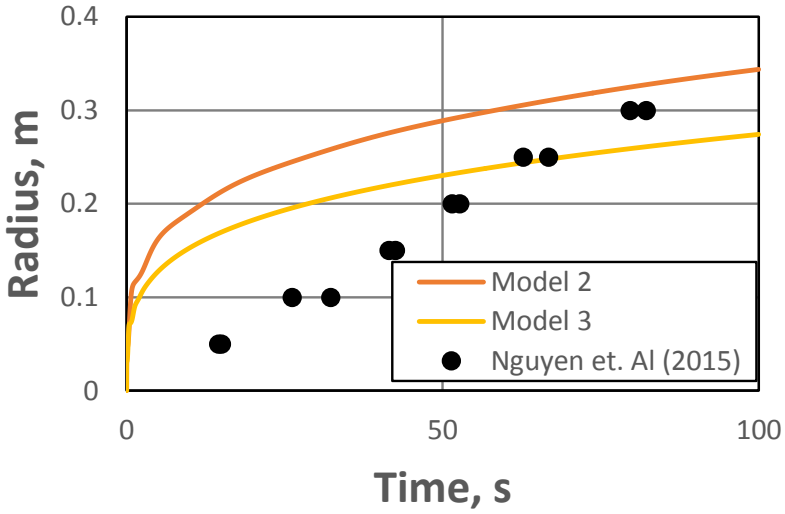

Figure 43: Validation of Model 2 and 3 against pool spreading data (Case 3 and 4)

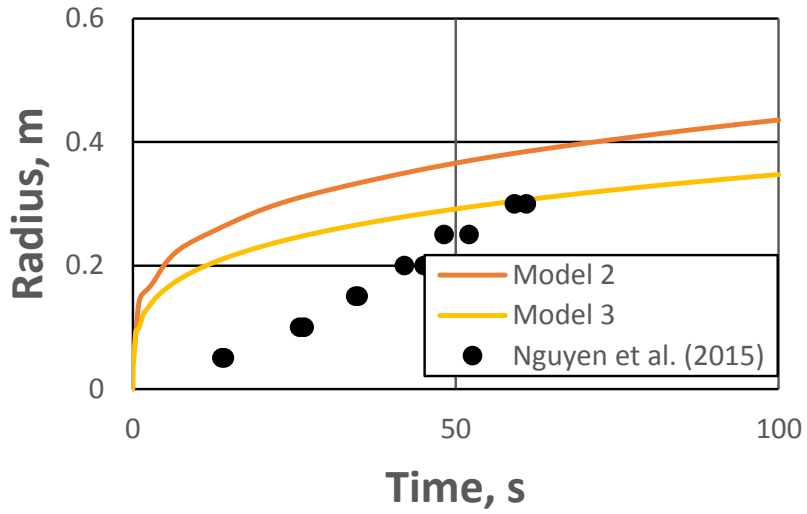

Figure 44: Validation of Model 2 and 3 against pool spreading data (Case 5 and 6)

Similar to the observations of the previous simulation, Model 3 gives a smaller pool radius prediction than Model 2 and Model 1. The difference between the Model 2 and Model 3 is less apparent in this simulation, possibly because the scale of the experiment was smaller. This validation activity indicates that the model predictions are within the range of the real data even if we lack the thermal properties to exactly simulate the scenarios. The model initially calculates high pool radius growth and then gradually decreases to converge to the experimental radius. As the scale of the spill is also much smaller than that of Moorhouse and Carpenter (1986), there are no data points after 100 s when the pool growth should by then slow down.

5.3.7 Summary of verification and validation activities

The replicated vaporizing pool spreading model has been validated using five sets of experimental data. It was found that the model predictions were comparable to experimental data, although overestimation of the pool radius was observed during the vaporizing pool spills.

6 EXPERIMENTAL RESULTS

The measurements to the pool temperature and temperature at different nodes and depths through the concrete were measured. There results gave insight to the validity of some assumptions incorporated by existing source term models.

6.1 Challenges faced prior to experiment

There were several challenges faced when setting up the experimental facility at RLESC. Most of these challenges were associated to troubleshooting the data acquisition (DAQ) system until it was ready for use.

6.1.1 Commissioning of data acquisition panel

The DAQ consisted of approximately 600 sensor connections. In the summer of 2016, it was found that many of the sensor connections would give faulty readings and exhibit the wrong computational settings (i.e. from N-thermocouple to K-thermocouple settings).

The troubleshooting phase of the DAQ panel used up at least a year of the project life. This phase includes the following tasks:

1. Testing the connection of each sensor
2. Ensuring that all physical components of the DAQ are present
3. Checking the readings of each permanent sensor
4. Modifying any wrong configuration of sensor connections

To check the usability of the DAQ, each connection at the DAQ was tested manually using a multi meter and a calibrator. For example, we would simulate mA signals ranging from

4 to 20 mA to connections with 4-20 mA signals. From here, it would be known which connections were working and which were not.

In the fall semester of 2016, it was found that the cold junction compensation components were missing in all thermocouple modules. This resulted to faulty readings at every thermocouple connections. The ferrules which were installed on these sensors also had to be replaced as they were not of the correct material. Other issues were not due to physical fault of the connections but mostly owed to configuration errors. RS Logix 5000 was the software used to reconfigure the sensor connections as needed.

6.1.2 Physical protection of data acquisition from dust and rain

After the second trial of the experiment, it was realized that many of the sensors embedded under the concrete did not change in value. A week after the experiment it was found that the power source for many of the sensor modules stopped working before the experiment started, causing the loss of data of many sensors. It was speculated that dust built up within the power source triggered the shutdown. Communication between RLESC and TAMUQ about the issue was started and resulted to better protection and maintenance program for the DAQ panel at TP-5.

6.1.3 Setup of software

The data logging software suitable for the DAQ system required a server system running a software called FactoryTalk Historian SE. This in turn requires switching the operating system of our computer to Windows Server 2012 R2 and creating a system architecture. As the graduate students working with TP-5 were unfamiliar with working with the software, we received the assistance of an engineer from Rockwell Automation (the vendor) to set up for the basic network.

6.2 Transition from boiling to evaporation regime

There is a need to ensure whether cryogenic spills ever go into evaporative cooling after a release on the ground, as most models assume that the pool boils until it completely vaporizes.

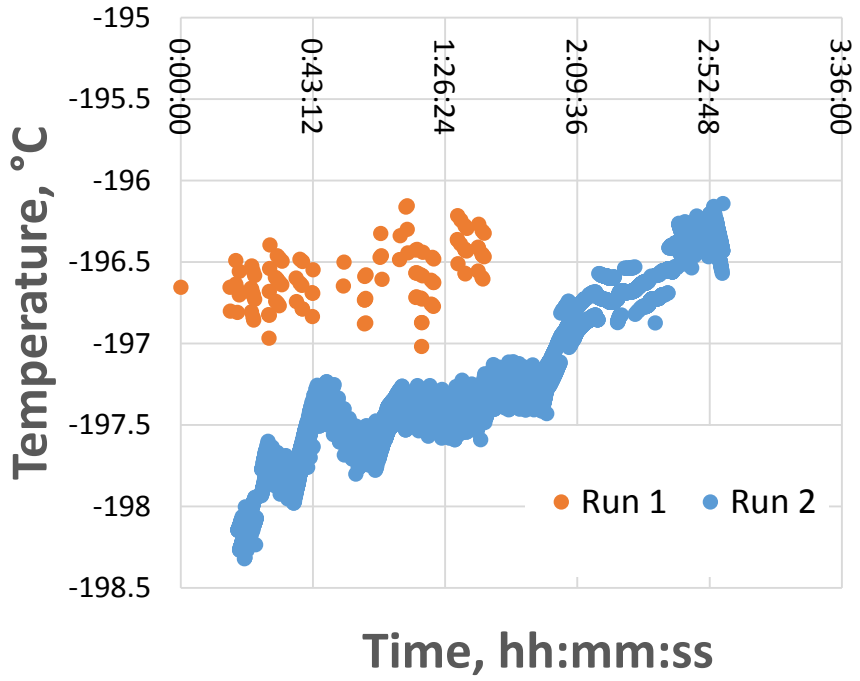

Figure 45: Evidence of boiling during the experiment

Two successful runs were performed on separate days. The first trial occurred while the wind speed averaged at 3.7 m s^{-1} ± 1.2 m s^{-1}. The second trial was run when wind speed was at 2 m s^{-1} ± 1 m s^{-1}. Temperatures measured close to the center of the pool were plotted with time to indicate the pool temperature throughout the experiment. Other than the momentary periods of vaporization due to the closing of the valve, liquid nitrogen was

consistently at its boiling point, as shown in Figure 45. No evaporative cooling was observed during the experiment. This result indicates reproducibility of the lab-scale results by Sadia *et al.*. (2015).

6.3 Temperature inside the concrete

The heat flux rate under the concrete varies according to position and time. To understand the progression of heat at different areas under the concrete, the locations of sensors under the pit base and walls have been divided into nodes shown in Figure 46. Each node is named according to its position. In total, there are 18 nodes within the concrete base, with 9 in each level.

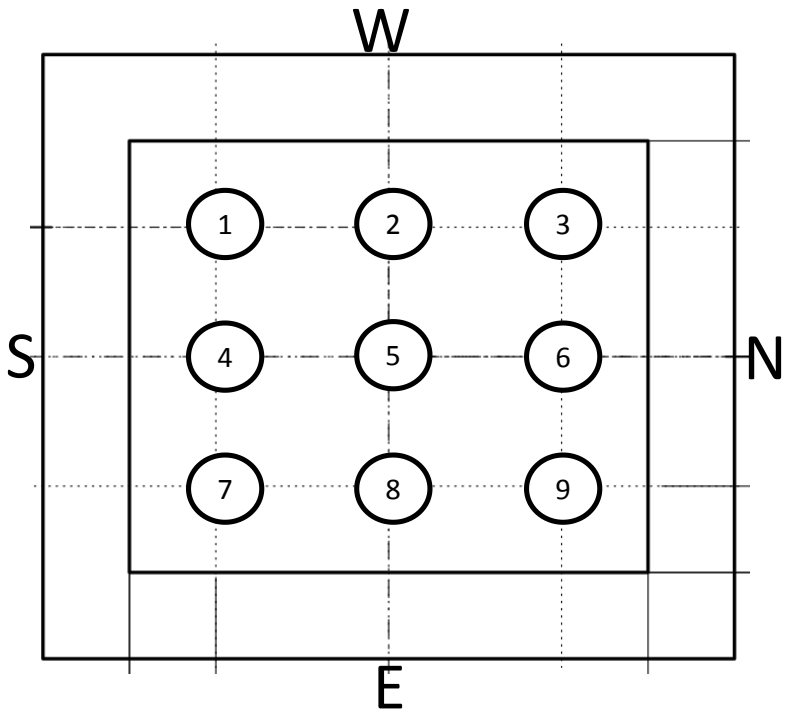

Figure 46: Grid number allocation on pit base

In trial 1 of the experiment, liquid nitrogen did not seem to have reached Nodes 9 and 3 because of the low discharge rate from the hose (Figure 47). It also seemed to travel to and fro at Nodes 2 and 6, which results to the temperature fluctuation. These data were not used in our analysis. Contrastingly, the pool did reach Nodes 1, 5, and 7.

Temperature change at the center of the base (Node 5) 0.05 m below the concrete was detected 266 s after the spill, as seen in Figure 47. It continues to drop until it reaches a minimum temperature of -156 °C In other nodes (Nodes 7, 1, 4), temperature started to change after 1000 s, after which they reach a minimum temperature of -140 to -146 °C. A 10 °C difference between the minimum temperature at Node 5 and Nodes 1 and 4 was also observed 0.15 m through the concrete (Figure 48). The temperature difference indicates the effect of the spreading pool towards the heat received by the substrate. Conduction models such as the "simple 1D" conduction model assumes uniform heat transfer towards the pool as if it was at the center of the pool, which does not account for the temperature difference. As seen in Nodes 7, 1, and 4, this is not the case throughout the pool life. Temperature difference across the nodes were not as apparent at 0.15 m depth through the concrete (Figure 48) due to the time delay, allowing heat to disperse more uniformly.

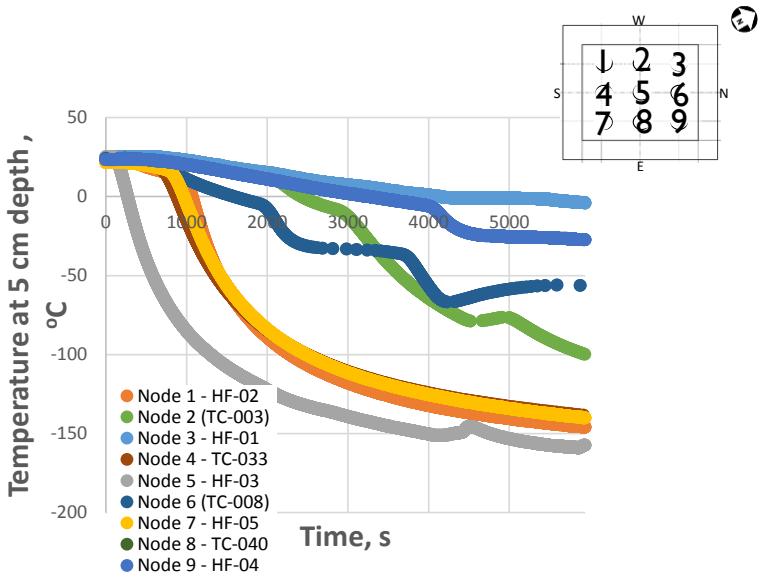

Figure 47: Temperature across the nodes at 0.05 m concrete depth (Trial 1)

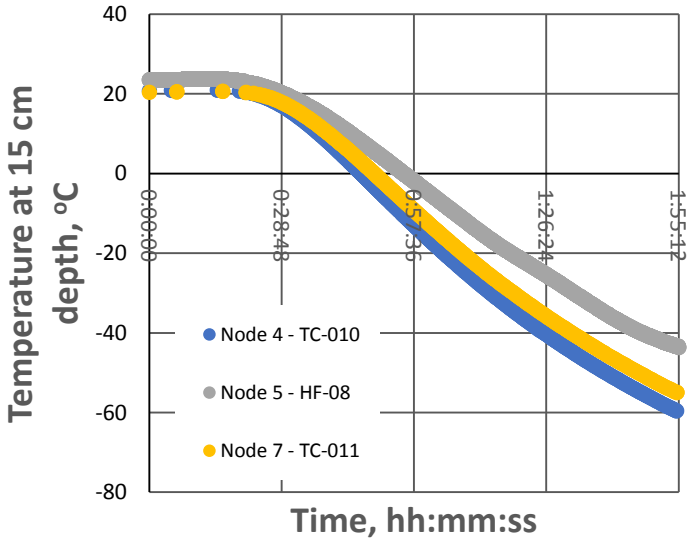

Figure 48: Temperature across the nodes at 0.15 m concrete depth (Trial 1)

7 VALIDATION OF EXISTING MODELS

In this section, the validity of the vaporizing spreading models (Model 2 and 3) are assessed with the experimental pool radius. Additionally, the adequacy of the one-dimensional conduction model for calculating conduction heat transfer to a cryogenic pool is investigated.

Data from Trial 2 was used in the pool spreading analysis as the amount of data points within Trial 1 were lacking. With a 1° slope from the deep-end to the shallow-end, there is a 6 cm height difference between the two ends of the pit, making the pool unsymmetrical. The 8 simultaneous measurements of the pool front were simplified to 4 average radii.

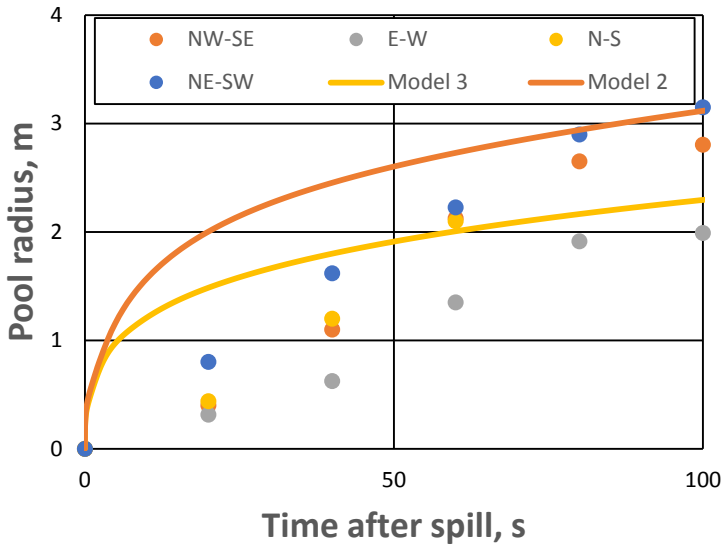

Figure 49: Radius of pool as in all 8 measured directions (Trial 2)

Compared to the experimental data, the radius predicted by Models 2 and 3 initially overshoots. While Model 2 continues to overestimate the pool size, Model 3 progresses to underestimate the pool at the last half of the spill, as seen in Figure 49. The experimental maximum pool radius varies according to the side at which side the pool is spreading because of the 1^{o} slope. Similar to the comparison done with Nguyen *et al.* (2015) data, Model 2 and 3 do not exhibit a large quantitative difference when compared to the experimental data. Model 3, however, provides a conservative prediction of the vaporization rate of cryogenic spills and an underestimation of the pool spreading rate for the last 50 s.

The assumptions of one-dimensional conduction through the concrete were tested by comparing temperature predictions at 0.05 m and 0.15 m underground with experimental data. Given the substrate thermal properties as a function of temperature, the simple 1D model was solved in two conditions; the first condition assumes thermal properties of the ground at ambient temperature, and the second assumes it at the boiling temperature of $LN_{2.}$ It was found that nearer to the surface, the model is fitted better when the substrate thermal properties are taken to be the boiling temperature of liquid nitrogen (Figure 50). Meanwhile, the experimental data at 0.15 m is closer to the model prediction when ambient substrate thermal properties were assumed (Figure 51). Thus, in order to model the temperature profile inside the concrete, the classic ideal one-dimensional conduction equation has to be corrected so that the thermal properties of the concrete is dependent on temperature (not constant).

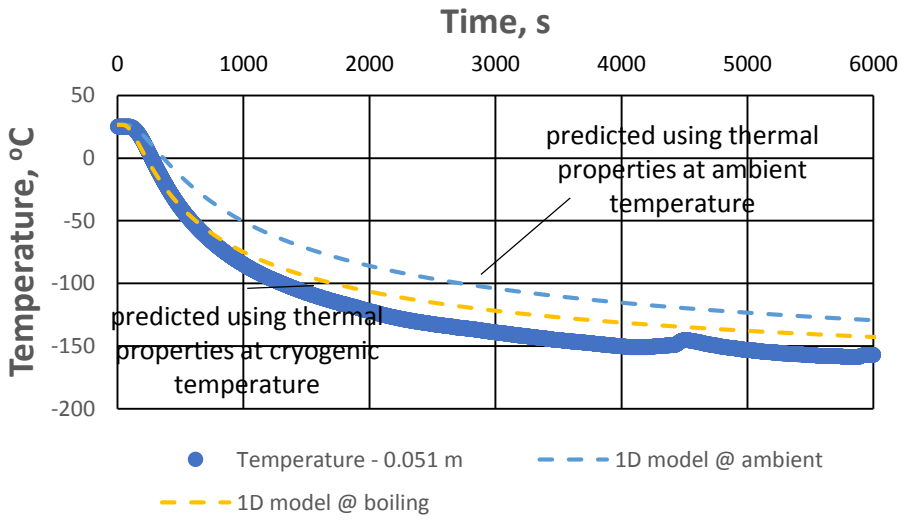

Figure 50: 1D model simulation (dotted) against temperature 5 cm through the concrete

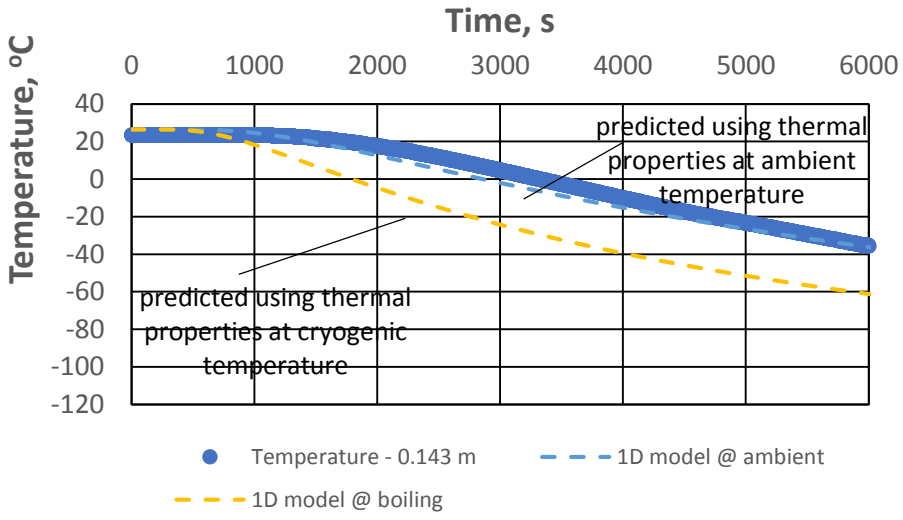

Figure 51: 1D model simulation (dotted) against temperature 15 cm through the concrete

In brief, the validation of Models 2 and 3 are tested with the experimental pool radius data, where the difference between the two models is the exclusion/inclusion of higher heat transfer at the outer rings of the pool during pool spreading. It was found that Model 2 consistently provides a more conservative (larger) pool than the experiment, while Model 3 progresses to estimate a smaller pool radius. This result made sense as the total heat transfer received by the pool was calculated higher in Model 3 than in Model 2. The fact that the pool was underestimated by Model 3 in the second half of the spill may indicate that the conduction heat transfer is being overestimated. Thus, reducing the heat transfer, possibly by taking into account resistance by bubble formation between the pool and the ground, may be a source of improvement. The applicability of Fourier's classic one-dimensional conduction equation was also tested. It was found that the model predictions were relatively close to the experimental data, as long as the thermal properties taken within the model are for temperatures close to the real-time substrate temperature.

8 PROGRESS IN LNG SPILL EXPERIMENT

As part of the work, a spill of LNG was conducted inside the TP-5 concrete pit to measure pool radius, depth, and methane gas concentration and fire radiation. The availability of LNG was uncertain until the last month before the project was due, so only preliminary analyses have been done on the recorded data. This section entails the experimental setup, preliminary results, and a list of lessons learned for future LNG experiments.

The commissioning work of the TP-5 site for LNG releases consisted of spilling LNG into the large burn-pit. Two spills of LNG have been conducted at the pit in TP-5 in two separate days. During each day, a full 38 m^3 LNG tanker was emptied into the pit through a fixed 4" pipe and black 4" hose. The vapor dispersion and fire radiation were tracked during the test through the methane gas sensors and radiometers, respectively. Temperature of the pool, level and temperature in the concrete were measured using thermocouples. Heat flux in the concrete was monitored via heat flux plates. Weather data were collected.

8.1 Sequence of events

The commissioning of LNG into the pit occurred for two days, in which LNG was ignited in the second day. A 38 m^3 tanker was top-loaded with LNG to 75% of its volume. Soon after the valve was opened, a leak was detected from a coupling between the cryogenic hose and the pipeline. After the coupling was rectified, LNG was spilled into the pit. Water curtains surrounding the pit were activated to limit the dispersion area. Figure 52 displays a vapor cloud being diluted by the water curtains. The spill lasted for approximately 1 hr 27 min before the tank was empty.

Figure 52: LNG dispersion limited by water curtains

During the second day of the test, the tanker and cryogenic hose were disconnected from the pipe and then moved to a safer location after all LNG has been delivered to the pit. Water was injected into the pit to observe rapid phase transition (RPT), however its effects were not notable. The LNG was then ignited and a large pool fire was formed. Firefighters on the site were instructed to control the flame as much as possible. Dry mix chemical extinguishers and high expansion foam were used to attempt to put the fire out. It was found that LNG could not be effectively extinguished with low quality high expansion foam and dry mix chemical extinguishers. After approximately thirty minutes into the fire, the power to the DAQ was shut off and no more data was recorded.

Figure 53: Pool fire generated at the large pit

8.2 Preliminary results

8.2.1 Day 1

Pool temperature, methane gas concentration, and temperatures through the concrete were measured during the first commissioning day. The concrete surface temperatures at various thermocouples drop to the LNG boiling point following the spill, and then steadily increases after 1 hr 27 min, which was when the spill was stopped, as shown in Figure 54. This was unlike the observations of the LN_2 spill experiments where temperature immediately fluctuates after the valve is closed, indicating vaporization. It was later found that water had filled the pit, and ice had formed between some amounts of LNG and the water. Thus, temperature measurements at the pit were not adequate as experimental data for LNG pool spreading and vaporization. As the hose was positioned to spill from the

south-east corner of the pit, the distances from the thermocouple to the spill point are also not yet calculated.

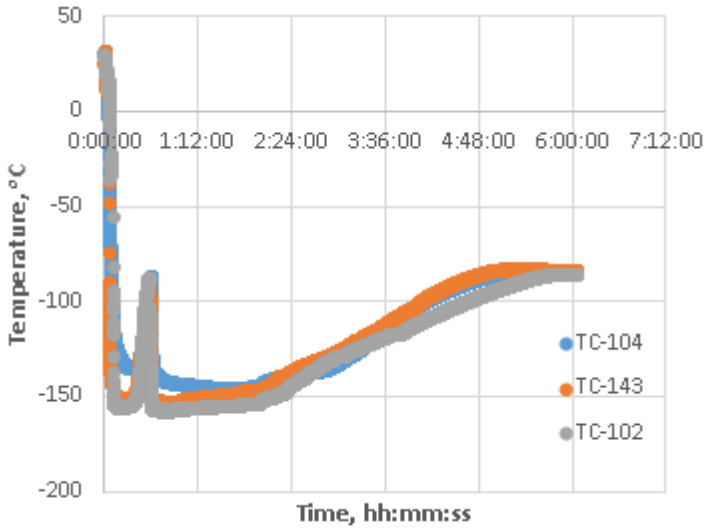

Figure 54: Temperature of the pool on the pit ground at various locations (Day 1)

Figure 55: Ice formation after Day 1 post water drainage

All methane gas sensors were located behind the water curtains. The maximum concentration momentarily detected by the nearest methane gas sensor during Day 1 was approximately 6% v/v, within the flammability limit (see Figure 56). This detection occurred before water curtains was activated. Post activation, this concentration was diluted to approximately 1-3% v/v, which is below the lower flammability limit (LFL). The concentration drop thus proves the effectiveness of the water curtains' activation.

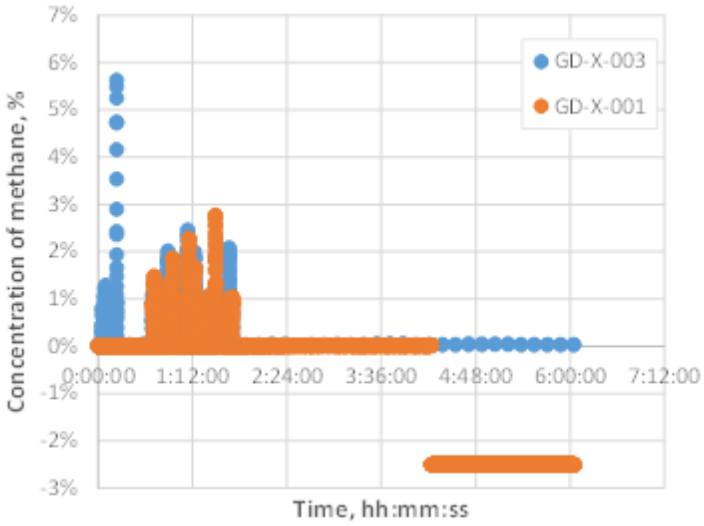

Figure 56: Concentration of methane at various locations (Day 1)

8.2.2 Day 2

Temperature of the pool between depths of 0 – 10.5 cm were measured, as shown in Figure 57, during the LNG spill on Day 2. Initially, the temperature drops to the boiling point of LNG. When ignited, the temperature immediately peaks to a temperature of approximately 1200-1300^{o}C depending on the thermocouple. The real flame temperature of the LNG may not have been detected as the data acquisition system (DAQ) only measures up to

1299°C. The pool temperature fluctuates and progressively decreases. The study of the pool fire will be in conducted as future work.

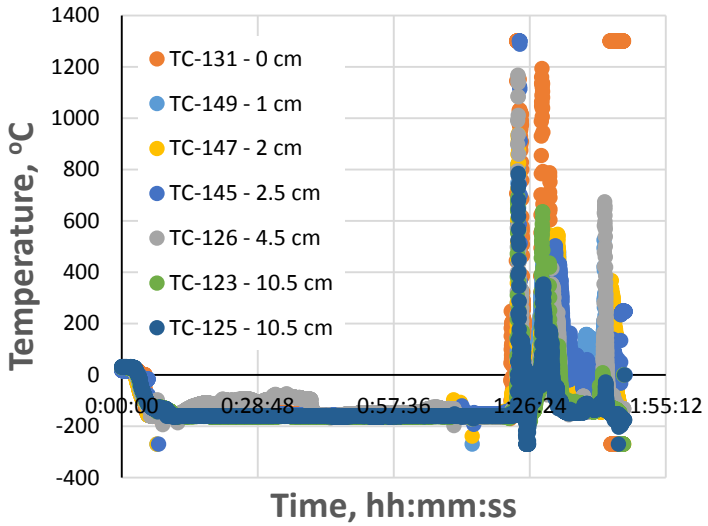

Figure 57: Pool temperature at various depths above the surface (Day 2)

Most of the methane gas sensors were removed from the site during the second day of the spill. Three methane gas sensors remained onsite at far distances from the pit. None of the sensors detected significant concentrations of methane as shown in Figure 58.

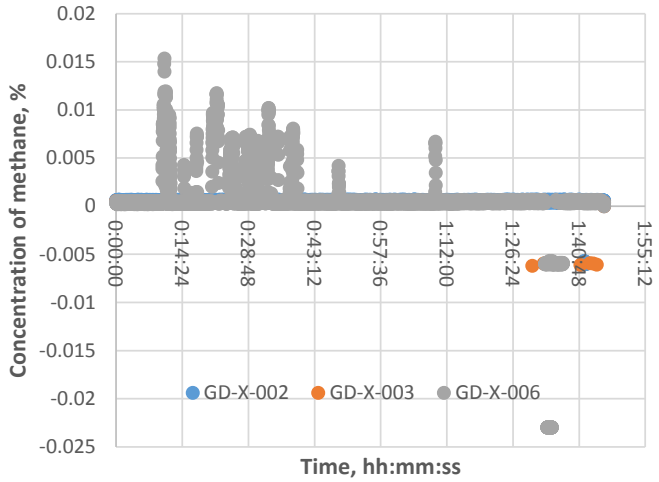

Figure 58: Concentration of methane at various locations (Day 2)

Radiation from the fire was measured by various radiometers surrounding the pit. The maximum radiation was detected at RF-12, as shown in Figure 59, which was 13 m away from the pit in the south direction. High radiation was also detected within the radius of 13 m and 22 m in various directions from the pit (RF-02, RF-07). However, other working radiometers, which are RF-01, RF-11, RF-10, RF-06, RF-05, RF-03, and RF-04, remained at low radiation (below 10 kW m^{-2}). A detailed study of the results found from the spill on Day 2 will be executed in the future. The TP-5 facility thus has shown positive potential for LNG source-term and dispersion studies.

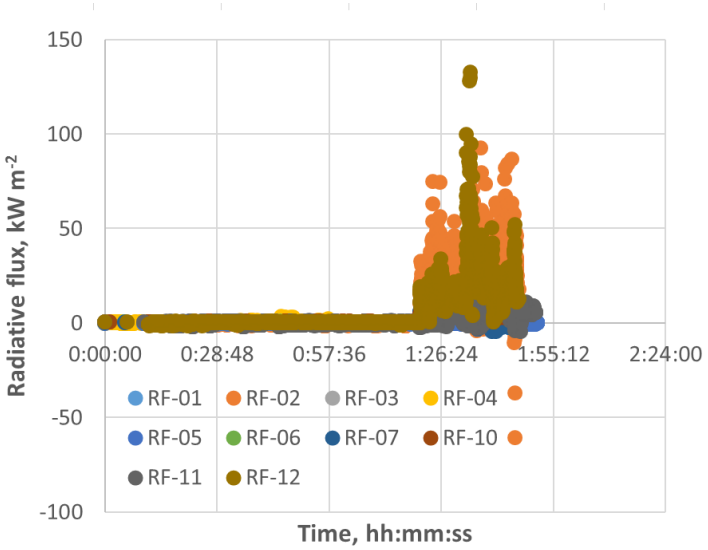

Figure 59: Radiative flux measured in various radiometers (Day 2)

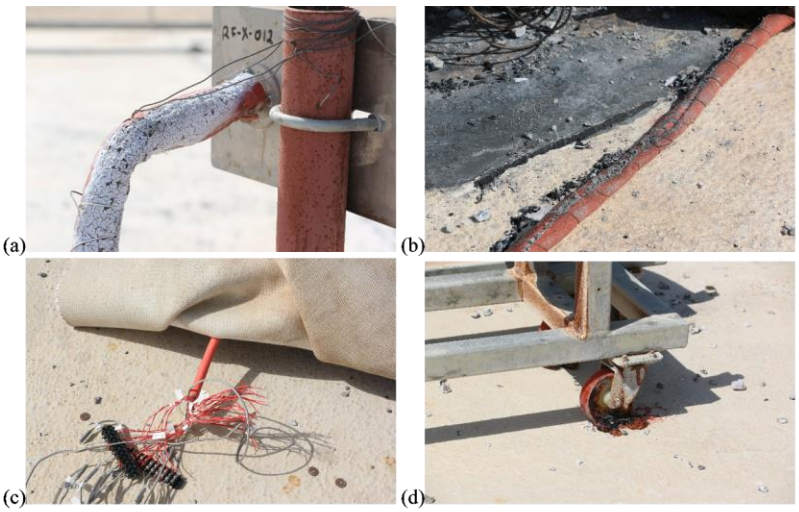

(a, b) undamaged fire sleeve
(c) undamaged cables under a fireproof sleeve
(d) damage of plastic wheels

Figure 60: After-experiment investigation evidence of insulation

8.3 Physical integrity of the facility

The integrity of all sensors stationed on-site have been assured after both days of the experiment, as all cables have been insulated using a fireproof sleeve.

(a) damage of the walls, (b) damage of the soft surface outside of the pit, (c) embedded wood in the walls, (d) limestone in the walls, (e) exposed thermocouple, (f) undamaged surface of the pit base.

Figure 61: After-experiment investigation evidence of concrete

8.4 Summary and lessons learned

Two spills of LNG have been conducted at the large burn-pit of TP-5. In the first day, only a vaporization test was carried out and the cloud was not ignited throughout the duration of the test. Water curtains surrounding the pit were activated to control the vapor dispersion. Due to the location of methane gas sensors being outside of the water curtain, the concentrations at most sensors were close to 0% v/v. One methane gas sensor (GD-X-03 in Figure 56) located in front of the water curtain, 28.86 m from the edge of the pit, gave a maximum reading of 6 % v/v for a short time prior to water curtain activation. Post water curtain activation, this maximum concentration was reduced to 2.6 % v/v. The measurement of pool radius, pool level and heat transfer in the concrete were compromised as the water entered the pit and misled the thermocouples and heat flux plates.

On the second day, LNG was spilled and then cloud was ignited. There was no monitoring of vaporization and pool spreading. For this experiment, only three methane gas sensors remained on site and the other parameters measured were the pool temperature, and temperatures and heat flux through the concrete. The methane gas sensors were relocated to much further distances from the pit and thus the concentrations at these locations were approximately zero.

After an ignition, a tall fire was observed. Fire radiation was monitored. The fire sleeve protection and water cooling system successfully maintained the integrity of the radiometers and all radiometers were undamaged during the test. The data acquisition (DAQ) system was shut-off after the first 40 minutes from the start of the fire. Measurements at the radiometers showed a maximum radiation of 100 kW m^{-2} at distance of 16.50 m from the edge of the pit (see RF-02 in Figure 57). Radiometers which were located behind the water curtains showed very low radiation during the fire thus showing a good effectiveness of the curtains to protect from radiation.

This was the first LNG spill in Qatar and much has been learned. Below is a list of the lessons learned:

1. With the current set up of the water curtains, the measurement of LNG vaporization and pool spreading are impossible due to the water interference inside the pit. Current water curtains should not be run during the exercise and should be used only in emergency. Alternatively, a second line of portable water curtains should be installed much further away from the pit for second-line defense.
2. When ice is formed under the water, it may mean that LNG is trapped underneath it. Care must be taken so not to ignite LNG.
3. To avoid ice formation with the current water curtain setup, igniting the mixture may be more recommendable after enough LNG has been released, so long as the fire generated can be controlled.
4. The fireproof sleeve used to insulate the sensor cables at the site were successful at protecting TAMUQ cables
5. The data acquisition panel and cables need to be sealed from water, dust, and heat at all times.
6. During the testing period, wind direction changed within 1-2 seconds. Equipment and firefighters onsite must be ready to be exposed to such radiation.
7. Additional actions need to be taken so to keep the integrity of the DAQ panel during a fire, as some connections became damaged after 30 minutes of the fire.

9 SUMMARY

The objective of this work is to validate existing source term models of LNG spills on concrete ground with a new set of experimental data at medium scale. Two spills of LN_2 on a 5 x 6 x 1.2 m pit were done to provide larger scale experimental data for existing cryogenic source term models. In each trial, temperature, vaporization, pool spreading rate, and heat flux to the pool and within the concrete were measured. Twenty-seven thermocouples have been aligned in 8 directions at the base of the pit to measure pool radius, and 12 thermocouples were aligned vertically to measure pool depth. Under the concrete, 100 thermocouples and 13 heat flux plates were arranged to measure heat transfer and temperature under the ground and through the walls at 5 cm and 10 cm depths. The pool front and depth were detected by the boiling temperature of LN_2 at the thermocouple. Although the spill was conducted twice, technical issues were faced during the second trial, causing the loss of some data. Some challenges were faced during the preparation for the experiment especially during the commissioning of the DAQ panel. Resolving these problems were time-consuming to the project.

Three models were generated in this work. Model 1 models a non-vaporizing spreading pool with continuity and momentum equations obtained from Gas Accumulation and Spreading Pools (GASP). Model 2 is a combination of Model 1 with the classic Fourier's one-dimensional conduction solution assuming perfect thermal contact and ambient ground temperature outside of the pool. The heat flux through the ground is solved at the center of the pool and is assumed uniform throughout. Model 3 is similar to Model 2, except that it was optimized to take into account larger temperature difference at the outer rings of the pool at each time step, resulting to a higher total heat transfer rate.

The algorithm of the model was verified using experimental data from Moorhouse and Carpenter (1986), Sadia *et al.*. (2015), and Nguyen *et al.*. (2015) and mathematical trends described by Webber (Webber, 1991;Webber and Brighton, 1987). Lastly, a validation study was done for the models which have been created.

As a result, the pool temperature and temperature of the concrete at 0.05 m and 0.15 m depth below the surface were used to justify the assumptions incorporated inside the model. The model was also directly validated with the experimental pool radius and temperature 0.05 m and 0.15 m through the concrete at the center of the pool.

The key findings of this study were the following points:

- No transition from boiling to evaporation within the pool was observed during the experiment. This was also observed in the smaller-scale LN_2 spill experiments by Sadia *et al.*. (2015). Such conclusion validates the assumption that LNG is boiling throughout its life until it has completely vaporized.
- At the base, temperature at the center of the pool decreased faster than other nodes, implying the effect of spreading upon heat transfer.
- The pool radius estimated by Model 2 and 3 was found to be relatively close with the experimental data, where Model 3 was at a better agreement. Despite of this, the predicted pool spreading rate of Model 3 starts off higher than the experimental data, but then progresses to spread at a slower rate, reflecting that heat transfer may have been overestimated by the model.
- Fourier's classic one-dimensional conduction equation solution was able to predict the concrete temperature underground, with a slight overestimation, if the thermal properties of the substrate is temperature dependent.

At the end of this thesis, LNG was made available. The same experiment was executed with LNG, with the addition of methane gas sensors and radiometers positioned around the pit. With the activation of water curtains surrounding the pit, water interfered with the measurement of the pool radius and vaporization. They also obscured some measurements of the methane gas sensors and radiometers behind the water curtains. Consequently, fire radiation and methane gas concentration at relatively close distances were recorded but measurements of the pool radius and vaporization are not yet obtained. To be able to

measure pool radius and vaporization of LNG from a concrete pit, activated water curtains should be located far enough to avoid the entrance of water inside the pit. Methane gas sensors and radiometers should also be located in front of the water curtains for more accurate measurements. Besides the water curtain, there are also additional measures to secure on-site equipment. Firstly, fireproof sleeves were found to be effective for the protection of exposed cables. Secondly, ice residue of the water inside the pit should also be taken care of cautiously as LNG could be trapped under the ice. Breaking the ice before all LNG have escaped risk an ignition.

There is much room for improvement within the current experimental setup in order to produce more reliable data. The first is to install additional thermocouples into the thermocouple frame in order to increase the amount of data points of the pool radius. The second is to be able to extract vaporization from the pool level. During the experiment, it was found that the thermocouples at the level meter detected vaporization at relatively close times, which implied instantaneous vaporization which was impossible. The cause for this reading was not concluded yet. A higher discharge rate to fill up the pit to higher levels and larger vertical distances of level meter thermocouples from each other, are recommended to reduce the noise generated by vapor formation.

During the experiment, it was observed that the inflow rate to the pit was not constant throughout the experiment. It is suspected that radiative and convective heat received by the hose vaporizes the cryogenic liquid before reaching the pit. The flowrate may fluctuate less when the cryogenic hose is insulated. It is also recommended to reproduce the experiment inside a larger pit, preferably one that is not sloped, so to achieve the development of a larger axisymmetric pool.

The implemented source term model based on GASP was found to have overestimated radius during the first half of the spill. Either the pool spreading model, the vaporization model or a combination of both could have contributed to the discrepancy. With the

validation of the pool spreading model with a water spill on plywood (Section 5.3.5), it is hypothesized that the LN_2 vaporized much more quickly during the first half of the spill than what was simulated. More study of vaporization model is recommended to understand why this overestimation was observed.

As future work, it would be interesting to measure the effect of convective and radiative heat transfer on the pool spreading and vaporization rates at large scale. This can be achieved by removing the wind fences surrounding the pit and to repeat the experiment during various weather conditions. It is also recommended to regenerate the experimental data with different release scenarios, by changing flowrates or spill type.

Lastly, preparations for LNG spill experiments should be developed further. To make the measurement of pool spreading and vaporization feasible, the framework inside the pit has to be replaced by a fireproof frame and water curtains must be positioned further away from the pit.

REFERENCES

Belore, R. C., McBean, E. A. (1986). *Modelling the spreading infiltration and evaporation of chemical spills on grass and impermeable surfaces*. Environment Canada, Ottawa.

Brighton, P. W. M. (1985*). Evaporation from a plane liquid surface into a turbulent boundary layer*. J. Fluid Mech. 159, 323–345. doi:10.1017/S0022112085003238

Briscoe, F., Shaw, P. (1980). *Spread and evaporation of liquid*. Prog. Energy Combust. Sci. 6, 127–140.

Britter, R. (1979). *The spread of a negatively buoyant plume in a calm environment*. Atmos. Environ. 13, 1241–1247.

Burgess, D. S., Zabetakis, M. G. (1962). *Fire and explosion hazards associated with liquefied natural gas, US Bureau of Mines Report of Investigations No. 6099*.

Drake, E. M., Reid, R. C. (1975). *How LNG boils on soils*. Hydrocarb. Process 54.

Incropera, F., DeWitt, D. (1996). *Fundamentals of heat and mass transfer*, 4th ed. Wiley, New York.

International Gas Union. (2017). *2017 World LNG Report.*

ioMosaic Corporation, Whitepaper. (2007). *Modeling LNG Pool Spreading and Vaporization*.

Kawamura, P., Mackay, D. (1987). *The evaporation of volatile liquids*. J. Hazard. Mater. 15, 343–364.

Lang, R. Z. J., Moorhouse, J., Paul, G. J. (1980). *Waterproof insulation materials*, in: Insititution of Chemical Engineers Seventh Symposium on Process Hazards.

Linden, P. F., Rottman, J. W., Daish, N. C., Dalziel, S. B. (1998). *LSMS : a model for the spreading and vaporization of spills of cryogenic and volatile liquids,* in: International Gas Technology Conference. San Diego.

Luketa-Hanlin, A. (2006). *A review of large-scale LNG spills: Experiments and modeling*.

J. Hazard. Mater. 132, 119–140. doi:10.1016/j.jhazmat.2005.10.008

Moorhouse, J., Carpenter, R. J. (1986). *Factors affecting vapour evolution rates from liquefied gas spills.* North West. Branch Pap. Inst. Chem. Eng. 1, 4.1–4.18.

Nguyen, D., Kim, M., Choi, B., Kim, T. (2015). *Experimental study of the evaporation of spreading liquid nitrogen, in: The 2015 World Congress on "Advances in Aeronautics, Nano, Bio, Robotics, and Energy (ANBRE15)*". Incheon, pp. 68–73. doi:10.1016/j.jlp.2015.11.018

Oke, A.O., Witlox, H. (2006). *PVAP Theory Document*.

Olewski, T., Véchot, L., Mannan, M.S. (2013a*). Study of the Vaporization Rate of Liquid Nitrogen by Small- and Medium-Scale Experiments*. Chem. Eng. Trans., 14th International Symposium on Loss Prevention and Safety Promotion in the Process Industries 31, 133–138.

Olewski, T., Véchot, L., Mannan, M.S. (2013b). *Source term modeling for LNG spills on land*, in: Qatar Process Safety Symposium 2013: Investing in Process Safety for a Sustainable Future. p. oral presentation.

Opschoor, G. (1979). *Methods for the calculation of the physical effects of the escape of dangerous material (liquids and gases) Part II*, in: TNO Yellow Book. Directorate-General of Labour, Ministry of Social Affairs, Netherlands, Voorburg, pp. 3–61.

Prince, A. J. (1985). *Experimental data on spill on land and water*, in: Details and Results of Spill Experiments of Cryogenic Liquids Onto Land and Water. United Kingdom atomic energy authority safety and reliability directorate (SRD R),100.

Quraishy, S., Sadia, A., Olewski, T., Véchot, L. (2015). *Modelling of Transition and Nucleate Boiling of Liquid Nitrogen Spill on Concrete*, in: Hazards 25.

Reid, R. C., Wang, R. (1978). *The boiling rates of LNG on typical dike floor materials*. Cryogenics (Guildf). 18, 401–404.

Reid, R. C., Wang, R. (1978). *The boiling rates of LNG on typical dike floor materials*. Cryogenics (Guildf). 18, 401–404. doi:http://dx.doi.org/10.1016/0011-

2275(78)90033-4

Sadia, A., Olewski, T., Vechot, N.L. (2015). *Cryogenic liquid spill experiments – at Lab Scale and Medium Scale*. Doha.

Thyer, A. M. (2003). *A review of data on spreading and vaporisation of cryogenic liquid spills*. J. Hazard. Mater. 99, 31–40. doi:10.1016/S0304-3894(02)00355-2

Webber, D. M. (2012). *On models of spreading pools*. J. Loss Prev. Process Ind. 25, 923–926. doi:10.1016/j.jlp.2012.05.003

Webber, D. M. (1991). *Source terms*. J. Loss Prev. Process Ind. 4, 5–15. doi:10.1016/0950-4230(91)80002-C

Webber, D. M. (1987). *Heat conduction under a spreading pool* (No. SRD-R-421; GB_ 1988:59593), HSE Reports. British Library Document Supply Centre, Warrington.

Webber, D. M., Brighton, P. W. M. (1987). *An integral model for spreading, vaporising pools* (No. SRD-R-390; GB_1987:55260), HSE Reports. UKAEA Safety and Reliability Directorate, Warrington.

Webber, D. M., Gant, S. E., Ivings, M. J., Jagger, S. F. (2010). *LNG source term models for hazard analysis: A review of the state-of-the-art and an approach to model assessment* (No. RR789), HSE Report RR789. Buxton.

Webber, D. M., Witlox, H. W. M. (2005). PVAP - Verification.

Witlox, H. W. M., OKE, A. (2008). *Verification and Validation of Consequence Models for Accidental Releases of Hazardous Chemicals to the Atmosphere*, in: Hazards XX - Process Safety and Environmental Proctection, Harnessing Knowledge - Challenging Complacency. IChemE, Manchester, pp. 1–12.

Woodward, J. L. (1990). *An integrated model for discharge rate, pool spread, and dispersion from punctured process vessels*. J. Loss Prev. Process Ind. 3, 33–37. doi:10.1016/0950-4230(90)85020-A

Woodward, J. L., Pitblado, R. M. (2010). *LNG Risk Based Safety: Modeling and Consequence Analysis, LNG Risk Based Safety: Modeling and Consequence*

Analysis. AIChE, John Wiley & Sons, Inc., NJ, USA; doi:10.1002/9780470590232

APPENDIX A

SUBSTRATE CHARACTERISTIC

The LNG research facility located at LNG training prop-5 (TP-5) of Ras Laffan Emergency and Safety College (RLESC) was constructed of industrial grade concrete designed to stand an extremely low (cryogenic) as well as extremely high (fire) temperatures. It is critical that the properties of this concrete are well known to ensure a good quality experimental data that can be used for model validation. These properties include physical properties, density and surface roughness as well as thermal properties, thermal conductivity, thermal diffusivity and heat capacity. It is to be noted that last three parameters are dependent and it is sufficient if two out of three are measured to be determined, and in this work these were: thermal conductivity and heat capacity.

Several concrete samples were taken during the construction of the research facility: six concrete samples (roughly each of 0.3 × 0.3 × 0.05 m size) prepared for the measurements of surface roughness and density and one big block of concrete (roughly 0.5 × 0.5 × 0.5 m) to prepare several samples for heat capacity.

A.1 Concrete density and composition

The average density of the concrete was estimated via measurement of the volume and weight of six concrete samples. All three dimensions of each sample were measured with an accuracy of 1 mm and their volume was estimated. The weight of each was measured with an accuracy of 1 g.

The average density of the concrete was calculated at 2323 kg m^{-3} with a standard deviation of 70 kg m^{-3} (Sadia *et al.*., 2015).

Table 26. Density measurements of concrete samples

Sample	Width, mm	Length, mm	Thickness, mm	Volume, m^3	Weight, kg	Density, kg/m^3
TP 5-1	300	300	44	0.0040	9.247	2335.1
TP 5-2	300	300	42	0.0038	8.929	2362.2
TP 5-3	299	300	43	0.0039	9.2465	2397.3
TP 5-4	298	300	43	0.0038	9.1061	2368.8
TP 5-5	300	300	46	0.0041	9.319	2251.0
TP 5-6	300	300	47	0.0042	9.396	2221.3

The mix details of the concrete was also obtained from RLESC and is shown in Table 27.

Table 27: Composition of concrete

Composition	Part
Aggregate (10 and 20 mm recrystallized limestone)	3
Washed Sand	2
Dry Portland Cement	1

A.2 Concrete surface roughness

The surface roughness was measured using surftest SJ 201P/M manufactured by Mitutoyo. The standard specified in the equipment was JIS B0601-2001, ISO with a sampling length of 8 mm. The equipment was set on "primary profile measurement" mode to obtain the real profile of the surface in terms of average roughness (Ra_{avg}), median roughness (Ra_{med}), and standard deviation of it (σ_{Ra}) for a sample length of 8 mm for each measurement. A total of 60 measurements were taken at 10 random locations (three

measurements for each location) for the surface of two random samples. The average roughness for two slabs and average rougness for all measurements are shown in Table 28 (Sadia *et al*., 2015).

Table 28: Surface roughness measurement for TP-5 concrete

Sample	Ra_{avg} μm	Ra_{med} μm	σ_{Ra} μm
TP 5-5	15.4	15.7	5.0
TP 5-6	18.6	16.0	8.8
Average for both samples	17.0	16.0	7.3

A.3 Concrete thermal properties

The thermal properties of the concrete were experimentally determined at NETZSCH Instruments Testing Laboratory, Burlington, MA, for a temperature range from -161 to 50°C. Standard procedures (ASTM C 177-10), steady-state heat flux measurements and thermal transmission properties by means of guarded hot plate apparatus, utilizing a Holometrix Model were followed to measure the thermal conductivity. Two concrete slabs of the same composition, and dimensions 305 mm by 305 mm square with a thickness of 43 mm, were polished and prepared at our laboratory, and then sent to NETZSCH for analysis of the thermal conductivity (Figure 62). The reported results have the uncertainty of lower than 7%. It is observed that concrete thermal conductivity increases almost linearly with temperature through the range, and the increase rate is higher between -161 to -66°C and lower from -41 to 50°C. A disturbance from the trend has been observed at temperature of 66°C, which created a decreasing trend between temperatures of -66 and -41°C, where the rate of change of thermal conductivity with mean temperature is negative.

Four additional small concrete samples were taken and prepared from the big concrete block that was made during the construction of the LNG research facility out of the same concrete. The mass of the samples were 12.61 mg, 10.02 mg, 10.02 mg, and 10.54 mg, respectively. All samples were tested using a Differential Scanning Calorimeter (DSC) to determine the specific heat capacity (*Cp*) as the function of the temperature within the range of -160 to 50°C. Test temperature program was isothermal at -185°C for 6 minutes, then heating was set from -185 to 60°C with 20 K min-1 ramp. The purge gas was helium with flow rate 40 mL min^{-1} and the sensor DSC type was E. Samples were tested utilizing crimped crucible aluminum cells. The result of this analysis is shown in Figure 63. The observed specific heat increases linearly with the increase of temperature, with an observed standard deviation varying from 2.4 to 1.5% at low temperatures, up to 3% at the temperature of 50°C. The specific heat of the concrete was about 2-2.5 times lower at cryogenic temperature than at 50°C.

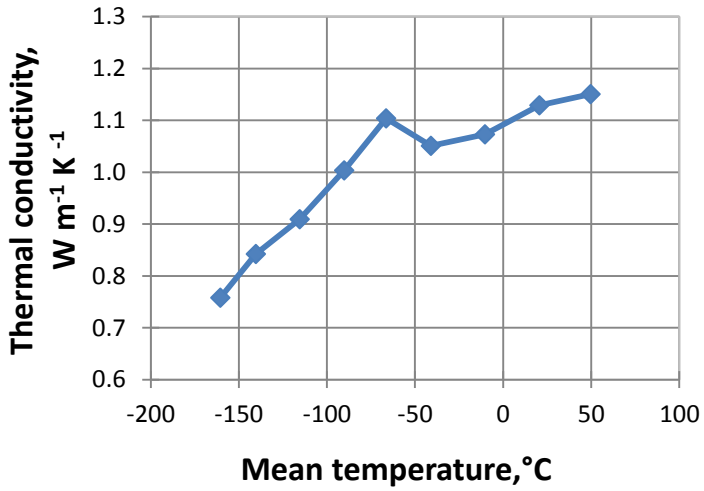

Figure 62: Thermal conductivity of the concrete samples as a function of temperature

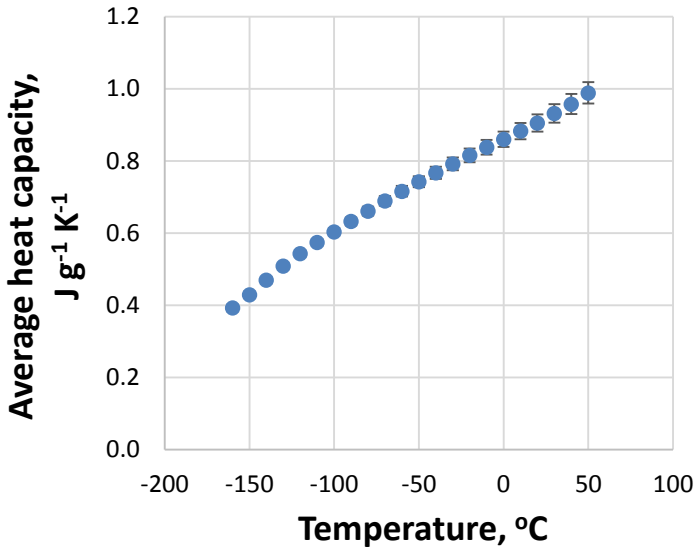

Figure 63: Heat capacity of the concrete samples as a function of temperature